

ALAAEDDIN LOULOU

# **Low-Complexity Multicarrier Waveform Processing Schemes for Future Wireless Communications**



ALAAEDDIN LOULOU

Low-Complexity Multicarrier  
Waveform Processing  
Schemes for Future Wireless  
Communications

ACADEMIC DISSERTATION

To be presented, with the permission of  
the Faculty of Information Technology and Communication Sciences  
of Tampere University,  
for public discussion in the auditorium TB109  
of Tietotalo, Korkeakoulunkatu 1, Tampere,  
on 22 November 2019, at 12 o'clock.

# ACADEMIC DISSERTATION

Tampere University, Faculty of Information Technology and Communication  
Sciences  
Finland

<i>Responsible supervisor and Custos</i>	Professor Markku Renfors Tampere University Finland	
<i>Supervisor</i>	Doctor Juha Yli-Kaakinen Tampere University Finland	
<i>Pre-examiners</i>	Associate Professor Gilberto Berardinelli Aalborg University Denmark	Doctor Jean-Baptiste Doré CEA Leti France
<i>Opponent</i>	Håkan Johansson, Professor Linköping University Sweden	

The originality of this thesis has been checked using the Turnitin OriginalityCheck service.

Copyright ©2019 author

ISBN 978-952-03-1348-7 (print)  
ISBN 978-952-03-1349-4 (pdf)  
ISSN 2489-9860 (print)  
ISSN 2490-0028 (pdf)  
<http://urn.fi/URN:ISBN:978-952-03-1349-4>

PunaMusta Oy – Yliopistopaino  
Tampere 2019

# Abstract

Wireless communication systems deliver enormous variety of services and applications. Nowadays, wireless communications play a key-role in many fields, such as industry, social life, education, and home automation. The growing demand for wireless services and applications has motivated the development of the next generation cellular radio access technology called fifth-generation new radio (5G-NR). The future networks are required to magnify the delivered user data rates to gigabits per second, reduce the communication latency below 1 ms, and enable communications for massive number of simple devices. Those main features of the future networks come with new demands for the wireless communication systems, such as enhancing the efficiency of the radio spectrum use at below 6 GHz frequency bands, while supporting various services with quite different requirements for the waveform related key parameters. The current wireless systems lack the capabilities to handle those requirements. For example, the long-term evolution (LTE) employs the cyclic-prefix orthogonal frequency-division multiplexing (CP-OFDM) waveform, which has critical drawbacks in the 5G-NR context. The basic drawback of CP-OFDM waveform is the lack of spectral localization. Therefore, spectrally enhanced variants of CP-OFDM or other multicarrier waveforms with well localized spectrum should be considered.

This thesis investigates spectrally enhanced CP-OFDM (E-OFDM) schemes to suppress the out-of-band (OOB) emissions, which are normally produced by CP-OFDM. Commonly, the weighted overlap-and-add (WOLA) scheme applies smooth time-domain window on the CP-OFDM waveform, providing spectrally enhanced subcarriers and reducing the OOB emissions with very low additional computational complexity. Nevertheless, the suppression performance of WOLA-OFDM is not sufficient near the active subband. Another technique is based on filtering the CP-OFDM waveform, which is referred to as F-OFDM. F-OFDM is able to provide well-localized spectrum, however, with significant increase in the computational complexity in the basic scheme with time-domain filters. Also filter-bank multicarrier (FBMC) waveforms are included in this study. FBMC has been widely studied as a potential post-OFDM scheme with nearly ideal subcarrier spectrum localization. However, this scheme has quite high computational complexity while being limited to uniformly distributed subbands. Anyway, filter-bank based waveform processing is one of the main topics of this work. Instead of traditional polyphase network (PPN) based uniform filter banks, the focus is on fast-convolution filter banks (FC-FBs), which utilize fast Fourier transform (FFT) domain processing to realize effectively filter-banks with high flexibility in terms of subcarrier bandwidths

and center frequencies. FC-FBs are applied for both FBMC and F-OFDM waveform generation and processing with greatly increased flexibility and significantly reduced computational complexity.

This study proposes novel structures for FC-FB processing based on decomposition of the FC-FB structure consisting of forward and inverse discrete Fourier transforms (DFT and IDFT). The decomposition of multirate FC provides means of reducing the computational complexity in some important specific scenarios. A generic FC decomposition model is proposed and analyzed. This scheme is mathematically equivalent to the corresponding direct FC implementation, with exactly the same performance. The benefits of the optimized decomposition structure appear mainly in communication scenarios with relatively narrow active transmission band, resulting in significantly reduced computational complexity compared to the direct FC structure.

The narrowband scenarios find their places in the recent 3GPP specification of cellular low-power wide-area (LPWA) access technology called narrowband internet-of-things (NB-IoT). NB-IoT aims at introducing the IoT to LTE and GSM frequency bands in coexistence with those technologies. NB-IoT uses CP-OFDM based waveforms with parameters compatible with the LTE. However, additional means are needed also for NB-IoT transmitters to improve the spectrum localization. For NB-IoT user devices, it is important to consider ultra-low complexity solutions, and a look-up table (LUT) based approach is proposed to implement NB-IoT uplink transmitters with filtered waveforms. This approach provides completely multiplication-free digital baseband implementations and the addition rates are similar or smaller than in the basic NB-IoT waveform generation without the needed elements for spectrum enhancement. The basic idea includes storing full or partial waveforms for all possible data symbol combinations. Then the transmitted waveform is composed through summation of needed stored partial waveforms and trivial phase rotations. The LUT based scheme is developed with different variants tackling practical implementations issues of NB-IoT device transmitters, considering also the effects of nonlinear power amplifier. Moreover, a completely multiplication and addition-free LUT variant is proposed and found to be feasible for very narrowband transmission, with up to 3 subcarriers. The finite-wordlength performance of LUT variants is evaluated through simulations.



---

## Preface

This study was carried out during the years 2014-2019 at the department of Electrical Engineering at Tampere University, Finland.

First and foremost, I would like to express my sincere and deepest gratitude to Prof. Markku Renfors. His great effort, patience, vast knowledge and continuous support has been guiding this research work. Working with Prof. Renfors has developed my personality as human and engineer. I am very grateful to have such opportunity. I would like also to express my deepest gratitude to Dr Juha Yli-Kaakinen for his great help in my research work. His advices and the discussions have helped greatly in my research development.

I would like to thank Prof. Mikko Valkama for his valuable recommendations and support. I would like also to thank Dr. Toni Levanen, Dr. Frank Schaich, Dr. Thorsten Wild from Nokia Bell Labs, and Mr. Vesa Lehtinen for their contributions in this research work.

I am grateful for Dr. Jean-Baptiste Doré and Dr. Gilberto Berardinelli for their valuable effort in reviewing this thesis. I would like also to thank Prof. Håkan Johansson for accepting to be the opponent for my dissertation.

I would like to also express my appreciations for my friends in Finland that have given all the necessary encouragements to continue this work. I would like to thank Dr. Sener Dikmese, Dr. Sajjad Nouri and Dr. Paschalis Sofotasios that they have shared the times with me in the University. Without missing my dearest friend, the first fire-line, the life support and guidance, many thanks to Mirhasn Miradham, Amir Shokohi, Annette Iliste, Arman Dastpak, and Armin Iraqi. I would also to send my thanks and gratitude to friends behind the seas, especially, Rashid El-Najjar, Salah Zendah, Ahmed Hetasi. To my family, I appreciate whatever you have given unconditionally to me and nothing can repay your sacrifices. My girlfriend Ida Reini, My sister Riima, the brother Amr, Emad, Aziz, Abd, the mother Nehad, and the my father Yahia.

Tampere, October 2019

AlaaEddin Loulou





# Contents

<b>Preface</b>	<b>iii</b>
<b>Acronyms</b>	<b>vii</b>
<b>Key symbols and expressions</b>	<b>xi</b>
<b>1 Introduction</b>	<b>1</b>
1.1 Background and motivations . . . . .	1
1.2 Objectives and scope of the thesis . . . . .	3
1.3 Outline and contributions of the thesis . . . . .	4
1.4 Author's contribution to related publications . . . . .	6
<b>2 Fundamentals of CP-OFDM with Spectral Enhancement Techniques</b>	<b>7</b>
2.1 CP-OFDM implementation . . . . .	7
2.2 Spectral enhancements techniques of CP-OFDM . . . . .	9
2.3 Computational complexity analyses of CP-OFDM and enhanced-OFDM schemes	16
2.4 Chapter summary . . . . .	20
<b>3 Fundamentals of Advanced Multicarrier Schemes</b>	<b>21</b>
3.1 FBMC waveforms . . . . .	21
3.2 Resource block based F-OFDM waveforms . . . . .	31
3.3 Computational complexity analyses of multirate schemes . . . . .	37
3.4 Chapter summary . . . . .	42
<b>4 Low-Complexity Multicarrier Schemes using Decomposed FC Processing</b>	<b>43</b>
4.1 The decomposition of circular convolution . . . . .	44
4.2 The decomposition of the multirate CC . . . . .	46
4.3 Analysis of the computational complexity of the decomposed variants . . . . .	57
4.4 Chapter summary . . . . .	66
<b>5 Multiplierless Filtered-OFDM Transmitter for Narrow-Band IoT Devices</b>	<b>69</b>
5.1 NB-IoT overview . . . . .	70
5.2 Single-input sample models for uplink transmitter . . . . .	71

---

5.3	Look-up table based implementations . . . . .	74
5.4	LUT wordlength requirements . . . . .	79
5.5	Computational complexity analyses of LUT variants . . . . .	84
5.6	Chapter summary . . . . .	87
<b>6</b>	<b>Conclusion</b>	<b>89</b>
<b>A</b>	<b>The Implementation of the Complex Multiplication and Complex Addition</b>	<b>93</b>
A.1	The multiplication of two complex numbers . . . . .	93
A.2	Complex multiplication of complex sequence by set of twiddle factor . . . . .	93
A.3	Odd-DFT implementations . . . . .	94
A.4	DFT pruning with single input/output . . . . .	95
	<b>Bibliography</b>	<b>97</b>



---

# Acronyms

<b>3GPP</b>	3rd Generation Partnership Project
<b>5G</b>	fifth generation
<b>5G-NR</b>	fifth generation new radio
<b>AFB</b>	analysis filter bank
<b>BER</b>	bit error rate
<b>BLER</b>	block error rate
<b>BPSK</b>	binary phase-shift keying
<b>CC</b>	circular convolution
<b>CP</b>	cyclic prefix
<b>CFO</b>	carrier frequency offset
<b>D-FC</b>	decomposed multirate FC
<b>D-FC-F-OFDM</b>	decomposed FC-F-OFDM
<b>D-FC-FB</b>	decomposed FC-FB
<b>DFT</b>	discrete Fourier transform
<b>DFT-s-OFDM</b>	DFT-spread-OFDM
<b>E-LUT</b>	extrapolated CP based LUT
<b>E-LUT-F</b>	F-SC-FDMA based E-LUT
<b>E-LUT-W</b>	WOLA-SC-FDMA based E-LUT
<b>E-OFDM</b>	enhanced OFDM
<b>EVM</b>	error vector magnitude

<b>F-OFDM</b>	filtered OFDM
<b>F-SC-FDMA</b>	time-domain filtering based SC-FDMA
<b>FB</b>	filter bank
<b>FBMC</b>	filter-bank multicarrier
<b>FC</b>	fast-convolution
<b>FC-F-OFDM</b>	FC-based F-OFDM
<b>FC-FB</b>	fast-convolution filter bank
<b>FDD</b>	frequency-division duplexing
<b>FFT</b>	fast Fourier transform
<b>FMT</b>	filtered multitone
<b>FS</b>	frequency spreading
<b>FS-FBMC</b>	frequency spreading FBMC
<b>G-LUT</b>	input-sample grouping based LUT
<b>G-LUT-F</b>	F-OFDM-SC-FDMA based G-LUT
<b>G-LUT-W</b>	WOLA-SC-FDMA based G-LUT
<b>GSM</b>	global system for mobile communications
<b>ICI</b>	inter-carrier interference
<b>IDFT</b>	inverse discrete Fourier transform
<b>IFFT</b>	inverse fast Fourier transform
<b>IoT</b>	internet-of-things
<b>ISI</b>	inter-symbol interference
<b>LTE</b>	long-term evolution
<b>LUT</b>	look-up table
<b>LUT-W</b>	WOLA-SC-FDMA based LUT
<b>LUT-F</b>	F-SC-FDMA based LUT
<b>MIMO</b>	multiple-input multiple-output
<b>mMTC</b>	massive machine-type communications
<b>MPR</b>	maximum power reduction
<b>NB</b>	narrow-band
<b>NB-FC</b>	narrowband D-FC

---

<b>NB-FC-F-OFDM</b>	narrowband D-FC-F-OFDM
<b>NB-FC-FB</b>	narrowband D-FC-FB
<b>NB-IoT</b>	narrow-band IoT
<b>O-LUT</b>	overlap storing based LUT
<b>O-LUT-F</b>	F-SC-FDMA based O-LUT
<b>O-LUT-W</b>	WOLA-SC-FDMA based O-LUT
<b>OFDM</b>	orthogonal frequency-division multiplexing
<b>OFDMA</b>	orthogonal frequency-division multiple access
<b>OLA</b>	overlap-and-add
<b>OLS</b>	overlap-and-save
<b>OOB</b>	out-of-band
<b>OQAM</b>	offset quadrature amplitude modulation
<b>PA</b>	power amplifier
<b>PAM</b>	pulse amplitude modulation
<b>PAPR</b>	peak-to-average power ratio
<b>PPN</b>	polyphase network
<b>PRB</b>	physical resource block
<b>PSD</b>	power spectral density
<b>QAM</b>	quadrature amplitude modulation
<b>QPSK</b>	quadrature phase-shift keying
<b>RB</b>	resource block
<b>RB-F-OFDM</b>	resource block filtered OFDM
<b>RC</b>	raised cosine
<b>RMS</b>	root mean squared
<b>RRC</b>	root raised cosine
<b>SC-FDMA</b>	single-carrier frequency-division multiple access
<b>SCS</b>	subcarrier spacing
<b>SFB</b>	synthesis filter bank
<b>SNR</b>	signal-to-noise ratio
<b>TDL</b>	tapped delay line

<b>UD-FC</b>	uniformly distributed D-FC
<b>UD-FC-F-OFDM</b>	uniformly distributed D-FC-F-OFDM
<b>UD-FC-FB</b>	uniformly distributed D-FC-FB
<b>UE</b>	user equipment
<b>UF-OFDM</b>	universal filtered OFDM
<b>UFMC</b>	universal filtered multicarrier
<b>WOLA</b>	weighted overlap-add
<b>WOLA-SC-FDMA</b>	WOLA based SC-FDMA
<b>ZP</b>	zero prefix

# Key symbols and expressions

$W_N = \exp[-2\pi j / N]$	Twiddle factor.
$N_{\text{CP}}$	The CP length.
$N_{\text{s}}$	The length of CP-OFDM symbol.
$N_{\text{EX}}$	The length of the cyclic extension.
$N_{\text{WOLA}}$	The length of the WOLA-OFDM symbol.
$N_{\text{h}}$	The filter length.
$\mu$	Multiplication rate.
$\alpha$	Addition rate.
$\kappa$	Subband index.
$R$	Interpolation factor.
$\langle a \rangle_N$	Modulo $N$ operation.
$\lambda$	Overlapping factor.
$D$	Decomposition factor.
$\lfloor a \rfloor$	The greatest integer less than or equal to $a$ .
$\lceil a \rceil$	The least integer greater than or equal to $a$ .
$\mathbf{I}_a$	$a \times a$ identity matrix.
$\mathbf{0}_{a \times b}$	$a \times b$ zero matrix.
$(c^{\circ \mathbf{A}})_{p,q} = c^{(\mathbf{A})_{p,q}}$	Element-wise matrix power of $\mathbf{A}$ .





---

# Introduction

## 1.1 Background and motivations

The foreseen wireless fifth generation new radio (5G-NR) is expected to deliver a vast variety of services and application to individuals, industries, and the society. The anticipated services are a big leap over the current technology of long-term evolution (LTE) towards an integrated multi-service network serving all areas of life in an economic and sustainable way. The features of 5G-NR include ultra-reliable and low-latency communications (URLLC) for critical and time-sensitive applications. Moreover, 5G-NR promises gigabits/s connections feeding the data-rate hungry applications with collectively enormous amount of data [SMS<sup>+</sup>17, EPGA16, DPS18]. With media-centered applications and devices, the bandwidth demand will dramatically increase. The use of frequency bands above 6 GHz could provide the spectrum for the bandwidth-hungry services. In high frequency ranges, high path-loss and short non-line-of-sight coverage is expected. Therefore, the use of massive multiple-input multiple-output (MIMO), beamforming, and small cell coverage is suggested in above 6 GHz frequency bands [RS<sup>+</sup>13, RS<sup>+</sup>14, HBL<sup>+</sup>14]. Those techniques could be also used for spectrum below 6 GHz to improve the channel capacity and communication availability. However, more effective use of the spectrum below 6 GHz is required for wide-area coverage. The commonly used waveform for current wireless communication systems, namely cyclic prefix (CP)-orthogonal frequency-division multiplexing (OFDM), does not provide proper spectrum localization, limiting dynamic and flexible use of the radio spectrum for different services in an efficient manner. Besides, the 5G-NR systems will allow various sensors, devices, and machines to interact by exchanging data through the wireless communication system. This kind of service is called massive machine-type communications (mMTC) and it is related to the general concept of internet-of-things (IoT). Such communication is usually in the form of sporadically sent small packets with very low average data rate per device. These services require cheap devices with battery life of 10 years or more.

The demanded features for 5G-NR challenges the current technology, LTE, and more specifically the use of plain CP-OFDM waveform. The obstacles for using CP-OFDM in 5G-NR have been addressed widely in the literature [LLJ<sup>+</sup>15, LSH<sup>+</sup>17, WAT16, GBB<sup>+</sup>17]. Basically, the CP-OFDM waveform produces high out-of-band (OOB) emission around the active subbands, and the flexible dynamic use of the spectrum is limited due to the spectral leakage. Therefore, LTE specifications assign relatively wide guard bands around the active part of the carrier. More-

over, the synchronization in time-domain becomes critical, requiring tight synchronization between base-station and user equipment (UE). The required synchronization process would introduce high overhead in sporadic low-rate traffic, like mMTC, and the mobile network might be congested by the signaling traffic. Due to these problems, it has been widely suggested to replace the CP-OFDM by a waveform with significantly better spectrum localization.

Therefore, enhancing the spectrum of CP-OFDM based waveforms is crucial in this context. It is supported by the 5G-NR development by the 3rd Generation Partnership Project (3GPP), which is based on CP-OFDM. The weighted overlap-add (WOLA)-OFDM scheme is based on applying time-domain window on the CP-OFDM waveform. This replaces the sharp transition between CP-OFDM symbols by smooth transitions, which helps to control the spectrum of the generated signal. This is an old idea from [GA96] and renewed in [R1-16a] as candidate waveform for 5G-NR. This scheme provides significant reduction in OOB emissions with low additional computational complexity. Nevertheless, this enhancement of the CP-OFDM is not very effective in frequencies close to the active subbands, and relatively wide guardbands are still needed. Another enhancement technique is to filter the CP-OFDM waveform. This filtered OFDM (F-OFDM) scheme suppresses the OOB emissions, but it introduces inter-symbol interference (ISI) and inter-carrier interference (ICI) because filtering harms the orthogonality of subcarriers [Fau00]. In basic F-OFDM, each subband is filtered separately using multirate digital filters, which significantly increases the computational complexity compared the basic CP-OFDM. Different variants of resource block filtered OFDM (RB-F-OFDM) have been proposed in the literature, such as universal filtered multicarrier (UFMC) [VWS<sup>+</sup>13]. UFMC is based on RB based filtering of zero-padded OFDM with filter tail shorter than the padding length. Either way, the complexity increment compared to CP-OFDM is still significant.

Basically, the filter-bank multicarrier (FBMC) waveform is subcarrier-wise filtering solution that uses very sharp filters to suppress the OOB emissions. Using well-localized subcarriers, FBMC can provide nearly-perfect OOB emissions. The FBMC scheme is traditionally implemented with relatively low complexity by using a polyphase network (PPN) together with discrete Fourier transform (DFT) or inverse discrete Fourier transform (IDFT) processing [BDH03, BDH99, CC97, VL01, SSL02]. Nevertheless, the computational complexity of FBMC is relatively high compared to CP-OFDM. Moreover, offset quadrature amplitude modulation (OQAM) is required for subcarriers to reach orthogonality, which leads to low commonality with CP-OFDM and various complications in certain waveform processing functions, like channel estimation and certain multi-antenna/MIMO schemes.

Recently fast-convolution filter banks (FC-FBs) have been proposed for waveform processing instead of the traditional polyphase filter-banks [UT10, TUIT09, RYH14]. FC-FB introduces more flexibility in controlling the subband center frequencies and bandwidths. Additionally, FC-FB simplifies the equalization process [RY14a, RY14b, ZWG15]. Furthermore, FC-FB adds extra level of flexibility such that FC-FB scheme can process simultaneously different waveforms, such as FBMC/OQAM, filtered multitone (FMT), and single carrier waveforms [YR13, SAYR15, YR15a, YR14a]. Furthermore, these added benefits become available with reduced computational complexity compared to the conventional filter-banks. Moreover, fast-convolution (FC) based implementation has been extended to implement F-OFDM as proposed in [RYL<sup>+</sup>15, RYLV16, YLRV17, YLV<sup>+</sup>17]. This new scheme has been denoted as FC-based F-OFDM (FC-F-OFDM). Again, FC-F-OFDM provides also more flexible implementation with reduced computational complexity compared to separate subband filtering or polyphase filter bank based F-OFDM schemes [LBY14, MZSR17, SW14].

Considering the 5G-NR challenges and requirements, effective and flexible schemes for enhancing the spectral characteristics of CP-OFDM is an essential topic to study. One important

motivation for this is to be able to relax the synchronization and power control requirements in uplink mMTC operation, as discussed above. Even more importantly, 5G-NR applies flexible parametrization for different groups of subcarriers (i.e., subbands or bandwidth parts in 3GPP terminology), in order to support the requirements of different services. The subcarrier spacings are integer multiples of the 15 kHz subcarrier spacing of LTE, and the useful symbol durations are inversely proportional to the subcarrier spacing. This so-called mixed numerology scheme degrades the orthogonality of subcarriers, introducing interference leakage between adjacent subbands. This inter-numerology interference (INI) is critical both in downlink and uplink transmission. Spectrum enhancement reduces the interference, making it possible to reduce the guardbands between subbands, which enhances the exploitation of the spectral resources. The F-OFDM schemes provide well-localized subbands, and FC-FB based filtering is a particularly appealing solution, offering new level of flexibility in allocating dynamically the spectrum for subbands with different service-dependent numerologies. Even though these schemes deliver reduced complexity compare to time-domain filtering or filter bank schemes, it is worth considering possible further reductions in the computational workload. This is especially the case when considering simple devices for services like mMTC.

3GPP has developed the narrow-band IoT (NB-IoT) as a cellular low-power wide-area (LPWA) IoT technology, intended to be applied in the LTE and global system for mobile communications (GSM) frequency bands [RMZ<sup>+</sup>16, WLA<sup>+</sup>17, XYW<sup>+</sup>18, MLT<sup>+</sup>18]. NB-IoT is also a strong candidate for the mMTC technology in the 5G context. NB-IoT uses CP-OFDM based waveforms with LTE-compatible numerology and no more than 12 subcarriers. Spectrum enhancement is also needed to satisfy NB-IoT specifications. NB-IoT is intended to be used in simple ultra-low complexity devices, which motivates the study of reduced complexity F-OFDM for narrowband allocations.

## 1.2 Objectives and scope of the thesis

The main objective of this thesis is to analyze and develop further communication waveforms with good spectrum localization for application in 5G-NR and beyond 5G wireless communication systems. Excellent spectral containment is critical for asynchronous transmission in heterogeneous communications reducing interference and increasing spectral efficiency. The spectrally well-localized waveforms come with excessive computational complexity requiring at least two times higher complexity than the corresponding CP-OFDM implementations. In case of narrowband allocations, which are relevant for simple low-cost devices, the difference is found to be much bigger. Hence, the main emphasis is on reducing the computational complexity without compromising the system performance. Particular focus is on narrowband allocations, which are typically encountered in simple devices with moderate data rate and long battery life demands. Reduced computational complexity is particularly important in such applications, since low complexity helps to reduce the cost and power consumption. Considering the developing 3GPP specifications for 5G-NR, the primary waveform of interest is CP-OFDM with filtering for spectrum enhancement. However, FBMC is also included in the study as an interesting choice for beyond-OFDM systems, also outside the cellular mobile network evolution, where the required waveform characteristics might be quite different. Two fundamentally different approaches for reducing the computational complexity are investigated:

- FC processing structure in narrowband allocations and other specific scenarios.

- A look-up table (LUT) based implementations of ultra-low complexity transmitters for NB-IoT devices and other OFDM-based applications with very low number of subcarriers.

The computational complexities of the developed solutions will be compared against baseline schemes and existing enhanced variants, especially with the direct FC implementations developed in the Wireless Communications research group at Tampere University. The metrics for computational complexity include multiplication and addition rates per transmitted/processed symbol and memory requirements. The proposed novel algorithms are tested through computer simulations in order to verify correct functionality and check that the performance is not compromised.

The research question can be formulated as follows: Can we achieve sufficient reduction in computational complexity through the two investigated approaches to make them interesting for practical devices? The quantitative target is to reach the complexity of plain CP-OFDM for filtered OFDM in general narrowband scenarios, and to reach significantly lower complexity in the specific case study on NB-IoT.

### 1.3 Outline and contributions of the thesis

Provided the objectives of the study, analytical signal/system models are developed for the studied waveforms and signal processing functions. Analytical expressions are derived also for computational complexity of the algorithms, mostly in terms of multiplication and addition rates per processed symbol. Figure 1.1 shows a simplified diagram of the thesis structure containing the studied schemes and their connection with different multicarrier waveform classes. Additionally, it summarizes the chapters contents that are detailed as follows.

Chapter 2 briefly describes the CP-OFDM scheme and discusses two main spectral enhancements techniques. First WOLA-OFDM is introduced and analyzed in this context, discussing the benefits and limitations of this scheme. Then conventional F-OFDM is also analyzed and discussed. Finally, the computational complexities of those schemes are analyzed and compared in LTE-like scenarios.

Chapter 3 gives an overview of different multirate filtering based waveforms. First subcarrier filtering based FBMC schemes are introduced, considering both time-domain and frequency-domain realizations of the filter banks. Focusing on frequency-domain filtering, special attention is given to FC processing as it is the core of the frequency-domain filtering. Moreover, resource block (RB) and subband based filtering is also discussed in this chapter showing the possible implementation options in time- and frequency-domains. The computational complexities of the considered schemes are analyzed and compared.

Chapter 4 continues the investigation of the multirate FC based schemes. The circular convolution (CC) decomposition is used for the implementation of the multirate FC based schemes, and novel implementations for FC-FB and FC-F-OFDM using the decomposition are proposed. The decomposed multirate FC (D-FC) scheme does not compromise the system performance in any way since its input-output behavior is equivalent to the direct FC scheme. Furthermore, D-FC based schemes are exploited in narrowband scenarios when the active bandwidth is relatively small compared to total bandwidth. In such cases, the computational complexity of the FC based implementation can be significantly reduced. Using this approach, CP-OFDM with dynamic pruned transforms is also proposed. Furthermore, the decomposition idea is analyzed also in the uniformly distributed non-overlapping subband scenario. This scenario

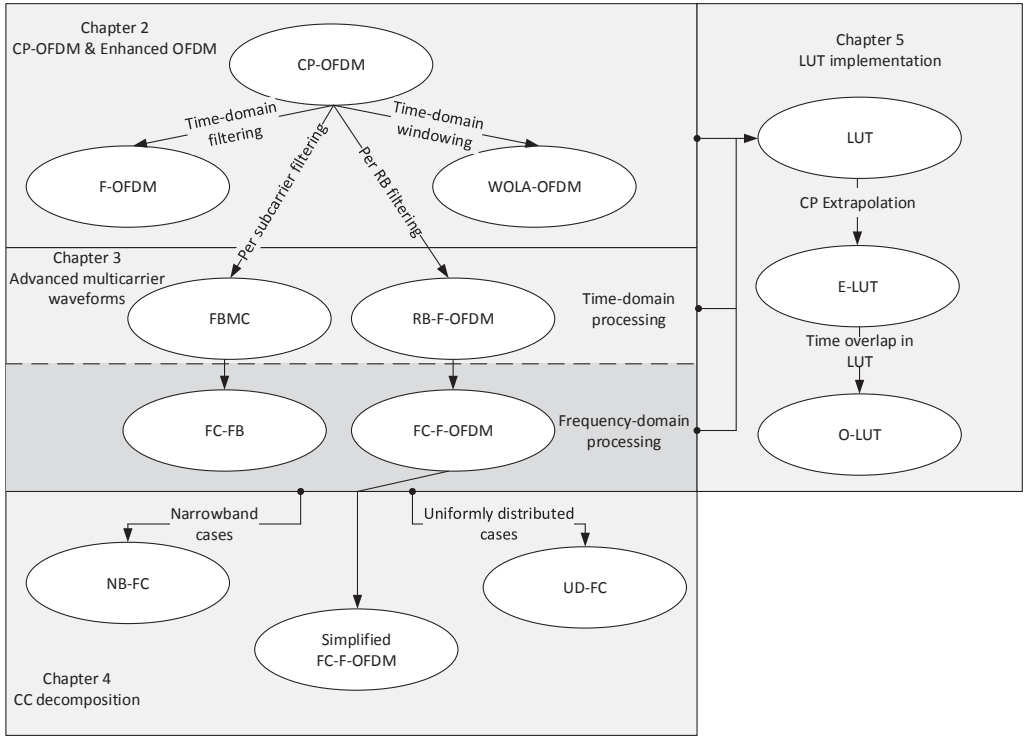


**Figure 1.1:** Thesis structure showing the studied waveforms, their classifications and their connections with the proposed schemes.

fits well with the FMT waveform, and the decomposition achieves a significant reduction in the computational complexity especially in oversampled cases. Besides, a special simplification for the discontinuous FC-F-OFDM receiver is also proposed. The simplification is based on the circular convolution decomposition.

Additionally, the design aspects of the decomposition variants are examined while considering optimal solution for reduced computational complexity. Consequently, the D-FC variants are compared to the time-domain and direct FC filtering based schemes through numerical case studies in LTE-like scenarios. The main findings of this chapter have been published in [LYR17, LYR19]. However, the simplified symbol-synchronized scheme of Section 4.2.4 has not been published earlier.

Chapter 5 investigates spectrally enhanced CP-OFDM waveforms with very low complexity for the NB-IoT service. Alternative LUT based schemes are proposed for multiplication-free implementations of narrowband transmitters, primarily for UE devices with ultra-low complexity. This approach provides completely multiplication-free implementations and the addition rates are not essentially increased with respect to the basic NB-IoT waveform generation without the needed elements for spectrum enhancement. The main idea is to store full or partial waveforms for all possible data symbol combinations. Then the transmitted waveform is composed through addition of needed stored partial waveforms along with trivial phase rotations. The proposed LUT approach is mainly considered for F-OFDM as the spectrum enhancement scheme. Also the WOLA model is considered for the stored waveform generation, but the F-OFDM is found to offer more attractive performance-complexity trade-off,

especially when the OOB emission requirements are relatively tight. The LUT based schemes can be implemented even without additions by storing all possible overlap sections between consecutive processing blocks in the memory. This proposed scheme is feasible in very narrowband cases with single or three subcarrier allocation cases of the uplink NB-IoT. The LUT based scheme is developed with different variants tackling practical implementations issues of NB-IoT device transmitters, including also the effects of nonlinear power amplifier. The minimum LUT wordlengths required to reach the 3GPP specifications are evaluated through computer simulations. The LUT approach and the main contents of this chapter are based on [LYL<sup>+</sup>19].

Chapter 6 summarizes the findings of the thesis and presents ideas for the future work for extending the study.

## 1.4 Author's contribution to related publications

The narrowband decomposed FC approach for transmitters was first published in [LYR17], and the study of decomposed FC schemes was further extended in [LYR19] to cover both transmitter and receiver sides and include the generic and uniformly distributed schemes. The findings of Chapter 5 are published in [LYL<sup>+</sup>19, LYKL<sup>+</sup>19]. The author of the thesis is the first author and main contributor in these publications. The mathematical analyses, computer simulations, and main part of the writing were carried out by the author of this thesis. The author's supervisor Prof. Markku Renfors is a co-author in all of the publications and made invaluable efforts regarding the technical content, quality of presentation, and writing. The author's instructor Dr. Juha Yli-Kaakinen is a co-author in all of the publications and carried out significant efforts to improve the publications' presentation quality and he provides technical assistance in FC and time-domain based FBMC implementations and relevant filter designs. [LYL<sup>+</sup>19] is based on the original idea of Dr. Frank Schaich and Dr. Thorsten Wild from Nokia Bell Labs. Dr. Toni Levanen, Mr. Vesa Lehtinen, and Prof. Mikko Valkama contributed greatly to elaborating the LUT-scheme to satisfy the NB-IoT specifications of 3GPP.

---

## Fundamentals of CP-OFDM with Spectral Enhancement Techniques

The advent of OFDM in wireless systems has transformed the telecommunication in such way that OFDM scheme is in the core part of most of the today wireless technologies. OFDM divides the spectrum into overlapping and orthogonal small bands that are called subcarriers. If the subcarrier spacing is small with respect to coherence bandwidth of the channel, the channel characteristics could be approximated as constant on each subcarrier simplifying the equalization process. Additionally, OFDM transmits the data with circular extension in the form of cyclic prefix (CP), and this allows to model the effect of frequency-selective multipath channel as circular convolution. This simplifies the channel equalization process even further. Moreover, OFDM is efficiently implemented using fast Fourier transform (FFT) resulting into very simple multi-access scheme in terms of computational complexity. Therefore, OFDM based on FFT delivers a simplified way of manipulating different users' bandwidths and center frequencies. Furthermore, OFDM allows straightforward implementation of the MIMO deployments.

However, OFDM has its own limitations that challenge its use in 5G-NR systems. Generally, the OFDM leaks high-powered sidelobes around the active bands. In other words, high-powered OOB leakage forces to maintain guard-bands around active bands of each OFDM channel. Besides, OFDM should maintain synchronicity in time- and frequency- domains to avoid ISI and ICI. Additionally, OFDM output has a considerably high peak-to-average power ratio (PAPR) that introduces spectral regrowth due to non-linearity of the power amplifier (PA).

This chapter represents the fundamentals of the CP-OFDM including implementation aspects as well as the benefits and limitations of the scheme. The spectral enhancements techniques for CP-OFDM scheme are also represented focusing on recently promoted techniques.

### 2.1 CP-OFDM implementation

In general, CP-OFDM transmitter modulates the incoming low-rate complex-valued samples to orthogonal overlapping subbands that are commonly called as subcarriers. The CP-OFDM transmitter is simply implemented by using IDFT that modulates the incoming low-rate samples to orthogonal frequencies. IDFT block can be implemented effectively using inverse fast Fourier transform (IFFT) algorithms such as radix-2 or split-radix. The use of IFFT block necessitates the segmentation of the stream of samples into the blocks of size  $N$ , which is the size of IFFT processing block. Following the IFFT, a copy of the samples at the end of



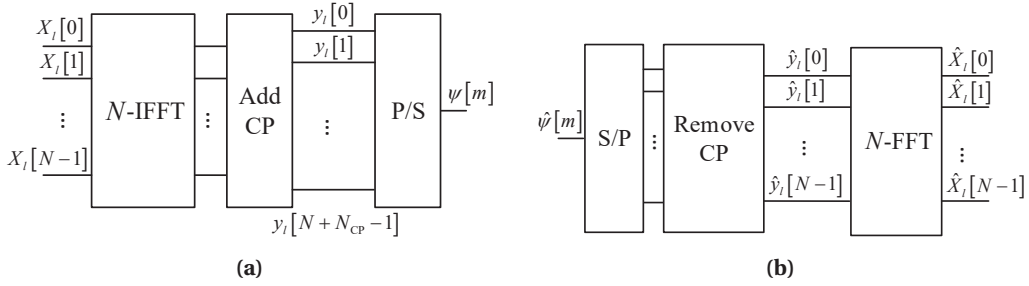


**Figure 2.1:** Basic implementation of the CP-OFDM (a) transmitter and (b) receiver. The P/S and S/P blocks refer to parallel-to-serial and serial-to-parallel operations, respectively.

the  $N$ -sample block is appended to the beginning of the  $N$ -sample block to create CP-OFDM symbol. Figure 2.1(a) shows the implementation of CP-OFDM transmitter that is represented mathematically as

$$y_l[n] = \frac{1}{N} \sum_{k=0}^{N-1} X_l[k] W_N^{-k(n-N_{CP})}, \quad (2.1)$$

where  $l$  is the index of the CP-OFDM symbol,  $n = 0, 1, \dots, N + N_{CP} - 1$  is the time index,  $k$  is the frequency index or subcarrier index,  $W_N = \exp[-2\pi j/N]$  is a twiddle factor or the  $N$ th root of unity,  $N_{CP}$  is the length of the CP,  $X_l[k]$  is the low-rate input at the  $k$ th subcarrier and  $l$ th CP-OFDM symbol, and  $y_l[n]$  is the CP-OFDM output at the  $n$ th time index and  $l$ th CP-OFDM symbol. The processed CP-OFDM symbols are finally concatenated in serial form as

$$\psi[m] = \sum_l w_T[m - lN_s] y_l[m - lN_s], \quad (2.2)$$

where  $N_s$  is the OFDM symbol length and  $w_T[m]$  is the transmitter time-domain window used to represent mathematically the block-wise processing due to IDFT. This time-domain window is a rectangular function with value of one when  $0 \leq m \leq N_s - 1$  and zero otherwise.

The receiver side is a dual of the transmitter as illustrated in Figure 2.1(b). The CP-OFDM receiver removes the CP and divides the received signal  $\hat{\psi}[m]$  to OFDM symbols of size  $N$  samples in the following way:

$$\hat{y}_l[n] = w_R[n] \hat{\psi}[n + N_{CP} + lN_s]. \quad (2.3)$$

Here,  $n = 0, 1, \dots, N - 1$ , and  $w_R[n]$  is the receiver time-domain window. The receiver window is a rectangular function that equals 1 for  $0 \leq n \leq N - 1$  and zero otherwise removing the CP. Then, the sequence is demodulated using DFT as follows:

$$\hat{X}_l[k] = \sum_{n=0}^{N-1} \hat{y}_l[n] W_N^{nk}. \quad (2.4)$$

Here  $\hat{X}^{(l)}[k]$  equals the transmitted low-rate inputs  $X^{(l)}[k]$  in the absence of channel distortions and noise, i.e.,  $\hat{y}[m] = y[m]$ . This equality is possible thanks to the orthogonality of DFT bases vectors preventing overlapping subcarriers to interfere.

Figure 2.2(a) shows the spectrum of the IDFT output of CP-OFDM transmitter for each subcarrier and sum of subcarriers. Notably, each subcarrier has a sinc-type response that results from the time-domain window  $w_T[m]$ . The overlapping subcarriers have nulls at frequency



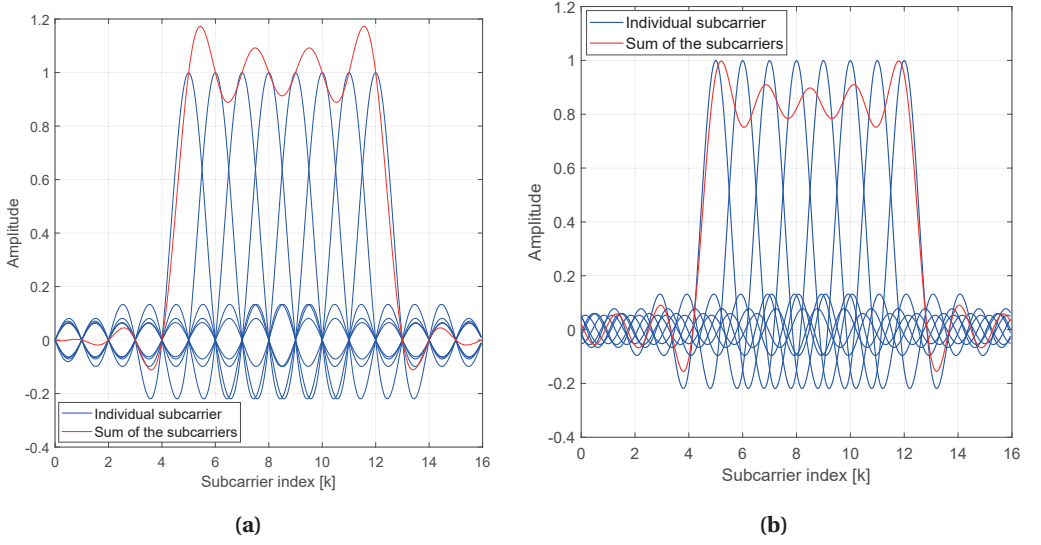


**Figure 2.2:** The spectrum of the DFT output showing the behavior of each subcarrier separately. The DFT size is 16 with 8 active subcarriers for (a)  $N_{CP} = 0$  and (b)  $N_{CP} = 3$ .

points corresponding to center frequencies of other subcarriers. Therefore, ICI is also null due to the orthogonality. However, this case is only true when  $N_{CP} = 0$ , otherwise, the CP-OFDM waveform loses the orthogonality as depicted in Figure 2.2(b). This is not crucial because the orthogonality is retained by removing the CP at the receiver side. The transmitter time-domain window,  $w_T[m]$ , in (2.2) is needed to provide the segmentation between the CP-OFDM symbols. In other words, the windowing operation is not practically applied on the CP-OFDM transmitter output, but it appears naturally due to the block-wise processing IDFTs. The DFT of (2.2) appears as sum of frequency-shifted Dirichlet function, i.e.,  $\sin(N_s \pi k/N) / \sin(\pi k/N)$ . The Dirichlet function has high power sidelobes, e.g., the maximum power level of the first side-lobe is only around  $-13$  dB lower than the main-lobe power. The summation of the frequency-shifted Dirichlet functions results in high power sidelobes around the active band in the CP-OFDM scheme. Therefore, it is suggested to use guard-bands around active bands of CP-OFDM to avoid the interference. This decrease in spectral efficiency could be seen as direct reduction in the throughput of the CP-OFDM system. For example, 5 MHz LTE system reserves 0.5 MHz of the spectrum as guard-band, e.g., 10% of the allocated bandwidth is reserved as guard-band. The unused spectrum in form of guard-band is very valuable considering the scarcity of the available spectrum below 6 GHz. Moreover, the high sidelobes introduce serious issues for OFDM scheme in opportunistic spectral use scenarios. The leaked power complicates the exploitation of the spectrum around the active bands, especially, in the gaps between the active subcarriers. These issues in the CP-OFDM affect the development towards the 5G-NR, considering asynchronous communication and the opportunistic spectral use as essential aspects of 5G-NR. Therefore, CP-OFDM scheme requires the spectral improvements to deliver well localized subbands with asynchronous transmission.

## 2.2 Spectral enhancements techniques of CP-OFDM

The spectral issue of the CP-OFDM has been addressed in the early literature discussing CP-OFDM. A considerable number of spectral enhancement techniques have been proposed

in the literature. According to [YFL14], those techniques could be classified based on the processing location in the CP-OFDM scheme and they are denoted as frequency-domain, symbol mapping, and time-domain approaches.

Frequency-domain based approaches process the inputs of the CP-OFDM transmitter to improve the spectral enhancement. Very basic enhancement technique is the deactivation of the subcarriers around the edge of the active subband [WHKJ04]. Definitely, deactivating some subcarriers around the active band reduces the OOB emissions. As consequence, this technique reduces the spectral efficiency of the CP-OFDM scheme and it does not essentially solve the problem of OOB leakage. Subcarrier weighting technique [CBS06] minimizes the sidelobes at specific frequency range by finding the optimal weights for the subcarriers through optimization. The optimization problem is defined by two parameters, the number of weighted subcarriers and the frequency range to be minimized. Then, the optimization problem is solved to obtain the subcarrier weights. Nevertheless, subcarrier weighting degrades the in-band error vector magnitude (EVM) [LR15]. In [BCS05b], so-called cancellation carriers are inserted around the active subband. Those subcarriers are optimized to suppress the power of the sidelobes at specific range. The cancellation carrier technique has seen several variations. In [PWR08], the cancellation carriers are optimized sequentially in such a way that the edge-most subcarrier is optimized for the edge-most frequency range and the second cancellation carrier is optimized for the second frequency range and so on. This reduces the computational complexity of the cancellation carrier scheme with some degradation in the sidelobe suppression performance. The effect of CP and time-domain window on cancellation carriers technique in unused spectrum between the subcarriers scenario has been discussed in [MA08b]. Moreover, [YPW08] suggests the use of genetic algorithm for optimizing the weights of the cancellation carriers. The cancellation carriers could be distributed over the spectral gaps orthogonal [Yam04] or non-orthogonal [QWJ10] with respect to the active subcarriers achieving significant reduction in the OOB emissions. In other work [KB13], the location of cancellation carriers are optimized to reach higher sidelobe suppression performance. Moreover, another simplified form of cancellation carriers technique where one or two cancellation carriers are used to suppress the sidelobes is proposed in [LR13]. Furthermore, the suppression performance of the simplified cancellation carriers technique has shown close performance to the normal cancellation carriers method. Moreover, it has been combined with time-domain windowing and edge windowing techniques [LR15]. Though the cancellation carriers has gained significant attention in the literature; the cancellation carriers and subcarrier weighting techniques have considerably high computational complexity when compared with the plane CP-OFDM as well as their suppression performance is limited only to specific range of the spectrum. Additionally, adding cancellation carriers reduces the spectral efficiency of the CP-OFDM.

Symbol mapping approach is based on remapping the input symbols in such way that sidelobes are suppressed around the active band. The multiple choice sequence technique remaps the symbol constellation in optimized sequence that has reduced OOB emissions [CM06]. However, this technique requires signaling with receiver side in order to retain the original symbols. The constellation expansion technique does not require the signaling with receiver by expanding the symbol constellation and then optimizing for symbol sequence with enhanced spectral localization [PRWM08]. Major drawback in this technique is the increase in the bit error rate (BER) for given signal-to-noise ratio (SNR) as the constellation order increases.

The final class of the enhancement techniques is time-processing based techniques. Those techniques are either filtering the CP-OFDM waveform to suppress the sidelobes or changing the rectangular time-domain window  $w_T[m]$  in (2.2) to new window with improved spectral characteristics. Both techniques are quite simple and straightforward with significantly

improved spectral localization. Motivated by the 3GPP studies [R1-16a, R1-16b, R1-16c], the time-domain windowing and F-OFDM are discussed in the following subsections.

### 2.2.1 Weighted overlap-add based CP-OFDM

The idea of modifying time-window had been exploited for improving the estimation of power spectral density (PSD) by weighted overlap-and-add (OLA) that denoted as Welch method [Wel67]. The use of proper time-domain window with steep edges improves the spectral estimation by producing pulse shape with low-power sidelobes with respect to the Dirichlet function. Basically, the trade-off is between the main-lobe width and maximum level of side-lobes. The modification of the time-domain window to improve the spectral characteristics is first proposed by [Mus96]. The author proposed the use of adaptive Nyquist time-domain windowing at the receiver side with doubling the receiver transform to enhance the reception of the OFDM waveform. Authors in [GA96] have proposed modified time-domain windowing at the transmitter side to reduce the effect of the synchronization errors in time- and frequency-domain. Later, [Arm99] analyzed further the effect of time-domain windowing to ICI due to frequency offset. Different window shapes have been later proposed and studied in the context of reducing the effects of the ISI and ICI in [SL05, MW01, BT07]. To author's knowledge, the use of raised-cosine window in CP-OFDM implementation has been proposed for sidelobe suppression in [WHKJ04]. Basically, the OFDM symbol is circularly extended from both ends of the symbol. Then the extended symbol is weighted by time-window and overlapped with adjacent symbols in guard-period. This extra time period prevents ISI at the cost of the time overhead. At that paper, time-domain windowing is proposed as a solution for spectrum pooling concept that allows the temporary users to exploit deactivated unused licensed spectrum [WJ04]. Moreover, time-domain windowing has been suggested to enhance the CP-OFDM waveform in the 3GPP document [3GP04]. Later, the time-domain windowing technique using raised cosine window is either compared [MA08b, WHKJ04] or combined [BCS05a] with other techniques. In [ESSA09], Hanning window is suggested instead of the raised cosine window. Edge windowing technique is proposed in [SA11a, SA11b, LGR13, cGD17], which divides the active subcarriers into two or more independently processed groups with different time-domain windows. Adaptive symbol transition technique, which is similar to time-domain windowing, adds optimized extension to the OFDM symbol reducing the OOB radiation [MA08a]. This technique improves the sidelobe suppression with respect to the time-domain windowing technique with increase in the computational complexity. In [R1-16a], the time-domain windowing technique was proposed to be used in the transmitter and the receiver as one of the 5G-NR waveforms candidates which is called as CP-OFDM with WOLA. Later, it was denoted as WOLA-OFDM. The proposed WOLA-OFDM is similar to the traditional time-domain windowing proposed in [WJ04] with slight difference. WOLA-OFDM symbol overlaps with adjacent symbols without including extra guard-period reducing the time overhead. Figure 2.3 explains the WOLA process at the transmitter and the receiver sides. Generally, WOLA-OFDM has been introduced to 5G-NR in [ZMSR16, GMD<sup>+</sup>17, MZSR17, TMS<sup>+</sup>18] due to its implementation simplicity and sidelobe suppression performance.

The implementation of the WOLA-OFDM transmitter is shown in Figure 2.4(a). In the transmitter, the IFFT output is circularly extended at the beginning of OFDM symbol by  $N_{CP} + N_{EX}$  and at the end by  $N_{EX}$  as

$$y_l[n] = \frac{1}{N} \sum_{k=0}^{N-1} X_l[k] W_N^{-k(n-N_{CP}-N_{EX})}, \quad (2.5)$$

where  $n = 0, 1, \dots, N_{WOLA} - 1$  and  $N_{EX}$  is the length of the cyclic extension added to each OFDM

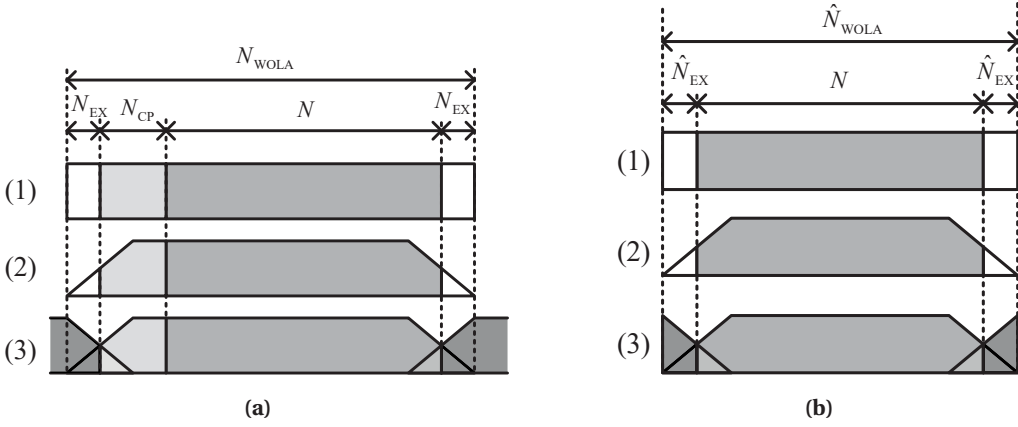


**Figure 2.3:** (a) The implementation of WOLA-OFDM processing on the transmitter side: (1) adding the CP and the circular extensions, (2) applying time-domain window  $w_T[n]$  and (3) overlap-and-add with the adjacent symbols. (b) The implementation of WOLA-OFDM processing on the receiver side: (1) cp removal leaving the extensions, (2) applying the time-domain window  $w_R[n]$  and (3) overlap-and-add of the beginning of the windowed symbol with the end.

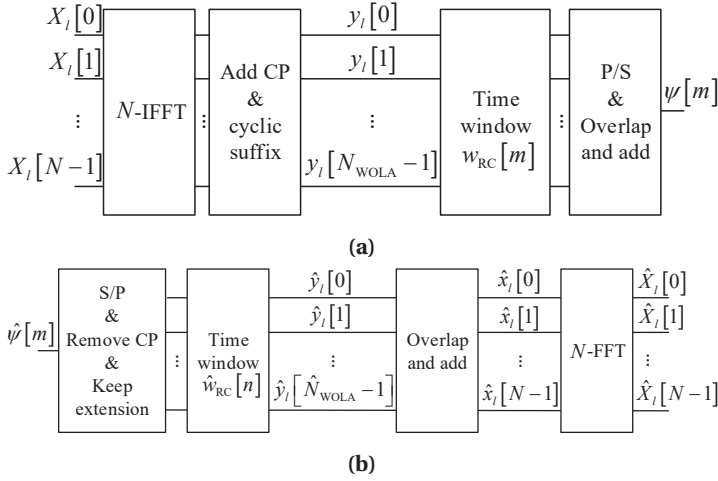


**Figure 2.4:** The implementation of the WOLA-OFDM (a) transmitter, and (b) receiver.

symbols defining the overlapping with the adjacent symbols. Now,  $N_{\text{WOLA}} = N_s + 2N_{\text{EX}}$  is the length of the WOLA-OFDM symbol after adding the CP and cyclic extensions. Consequently, WOLA process is defined simply by (2.2), where the time-domain window  $w_T[m]$  is defined as raised-cosine window,  $w_{\text{RC}}$ , providing faster decaying sidelobes than the rectangular window. The raised-cosine window is defined as

$$w_{\text{RC}}[m] = \begin{cases} 0.5 + 0.5 \cos\left(\pi + \pi \frac{m}{N_w}\right), & \text{for } 0 \leq m \leq N_w - 1 \\ 1, & \text{for } N_w \leq m \leq N_s + 2N_{\text{EX}} - N_w - 1 \\ 0.5 + 0.5 \cos\left(\pi + \pi \frac{m - (N_{\text{WOLA}} - 2N_w - 1)}{N_w}\right), & \text{for } N_{\text{WOLA}} - N_w \leq m \leq N_{\text{WOLA}} - 1 \\ 0, & \text{otherwise,} \end{cases} \quad (2.6)$$

where  $N_w$  is the number of the non-trivial values of  $w_{\text{RC}}[m]$ , i.e.,  $w_{\text{RC}}[m] \neq 0$  and  $w_{\text{RC}}[m] \neq 1$ .

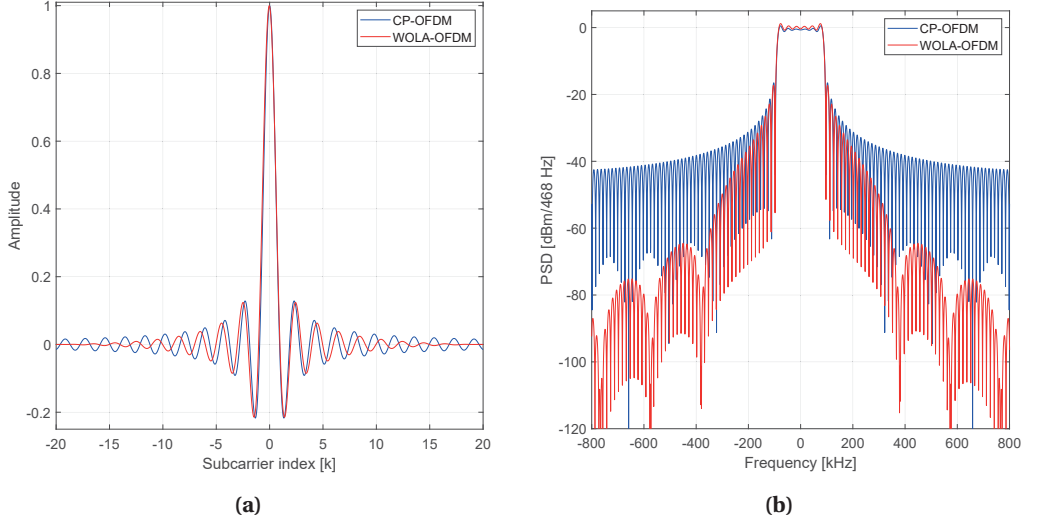


**Figure 2.5:** The CP-OFDM and WOLA-OFDM with  $N = 128$ ,  $N_{CP} = 9$ ,  $N_{EX} = 5$ , and  $N_w = 10$  (a) spectrum for single subcarrier and (b) PSD for 12 subcarriers.

Generally, the increase in  $N_w$  provides improved frequency localization for the WOLA-OFDM scheme.

In similar way, WOLA-OFDM receiver, that is shown in Figure 2.4(b), could be used to reduce the effects of the interference and distortion caused by asynchronous users. Similar to (2.3), the receiver removes the CP while keeping two extensions at the beginning and at the end of symbol as follows:

$$\hat{y}_l[n] = w_R[n] \hat{\psi} \left[ \langle n + N_{CP} - \hat{N}_{EX} \rangle_{N_s} + l N_s \right]. \quad (2.7)$$

Here  $\langle \cdot \rangle_{N_s}$  is modulo  $N_s$  operation,  $n = 0, 1, \dots, \hat{N}_{WOLA} - 1$  is time index within symbol,  $\hat{N}_{WOLA} = N + 2\hat{N}_{EX}$ , and  $\hat{N}_{EX}$  is the time extension that is used in the WOLA process on the receiver side. Then overlap and add is performed between the windowed part at the beginning and the end of the symbol as follows:

$$\hat{x}_l[r] = \hat{y}_l[r + \hat{N}_{EX}] + \hat{y}_l[r + N + \hat{N}_{EX}] + \hat{y}_l[r - N + \hat{N}_{EX}]. \quad (2.8)$$

Then the output of the WOLA process is fed to FFT as follows:

$$\hat{X}_l[k] = \sum_{r=0}^{N-1} \hat{x}_l[r] W_N^{rk}. \quad (2.9)$$

WOLA-OFDM scheme achieves a significant reduction in the OOB emissions of CP-OFDM spectrum. Modifying the window shape to be raised cosine (RC) reduces significantly the sidelobes power when compared to Dirichlet function. Figure 2.5(a) shows the subcarrier PSD of the CP-OFDM and WOLA-OFDM waveforms. The frequency-response of the WOLA-OFDM subcarriers decays faster than CP-OFDM subcarrier. This reduces the OOB emissions of WOLA-OFDM waveform as shown in Figure 2.5(b).

## 2.2.2 Filtering based CP-OFDM

Filtered OFDM waveform processing could be the straightforward solution to the problem of high OOB leakage of plain CP-OFDM waveform. This has been addressed in [GL95] where

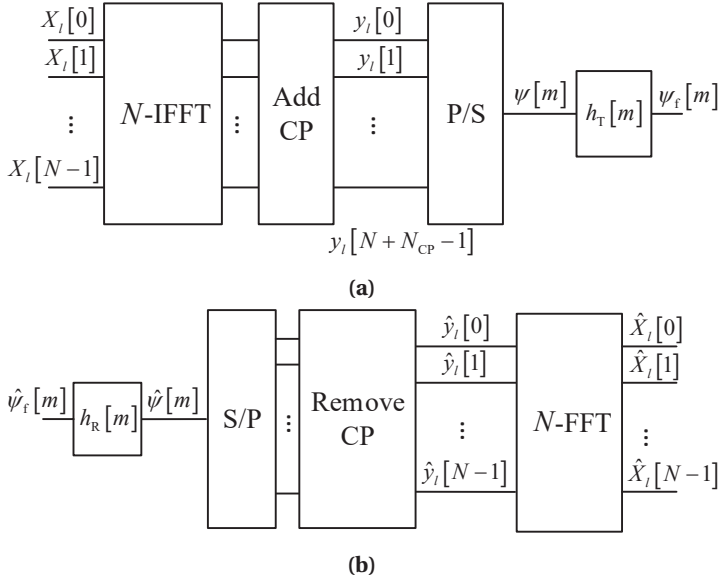


**Figure 2.6:** The implementation of the F-OFDM (a) transmitter, and (b) receiver.

filtering is applied partially on the edge subcarriers considering the orthogonality of the used filters in the optimization. The effects of time-domain filtering on the CP-OFDM scheme is discussed in [Fau00]. The authors consider the filtering for interpolation/decimation and reconstruction/anti-aliasing purposes. Generally, filtering the CP-OFDM symbol results in smearing the CP-OFDM symbol in similar way as in WOLA-OFDM system causing ISI in adjacent CP-OFDM symbols. In [MAK13], the effect of the filtering on the receiver side is examined in generic way. In [NGB11], it is suggested to filter the output of the CP-OFDM system for OOB leakage suppression. Then, an essential improvement to F-OFDM is proposed in [LKBY13]. This improvement is based on processing each set of continuous subcarriers or RBs independently introducing modular implementation to F-OFDM. The proposed scheme, which is called RB-F-OFDM, passes each subband to decimated CP-OFDM transmitter and the output is interpolated using time-domain low-pass filter. This multirate operation has been realized using PPN for uniformly distributed subbands in [LBY14]. Filter design for F-OFDM and RB-F-OFDM schemes has been discussed in [KLS14, CHGH16, YX17]. Many other multirate filtering based on OFDM schemes such as UPMC [VWS<sup>+</sup>13] has been proposed in the literature. Nevertheless, this chapter discusses only the basic implementation of the F-OFDM. Other forms of multirate based F-OFDM will be discussed in Chapter 3.

The implementation of F-OFDM transmitter and receiver are shown in Figure 2.6. The incoming low-rate signal  $X_l[k]$  is processed using CP-OFDM modulator as in (2.1) and (2.2). This is followed by filtering the output of OFDM to suppress the OOB emission as

$$\psi_f[m] = \sum_{\eta=0}^{N_h-1} h_T[\eta] \psi[\eta - m], \quad (2.10)$$

where  $N_h$  is the length of the transmitter filter  $h_T[m]$ . On the receiver side, the incoming high rate signal is filtered by the receiver filter  $h_R[m]$ . This is followed by typical CP-OFDM receiver in similar way in (2.3) and (2.4). Figure 2.8(b) compares the PSD of F-OFDM with CP-OFDM. In this example, CP-OFDM is filtered using linear-phase low-pass filter with pass-band edge at

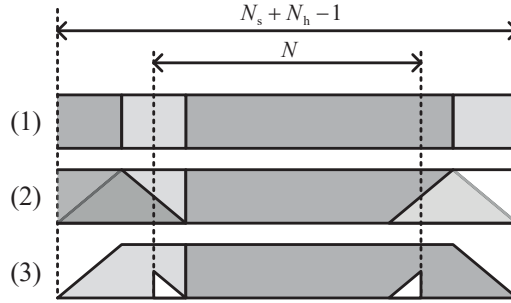


**Figure 2.7:** Time-domain representation of the filtering effects on symbol in time-domain. (1) The CP-OFDM symbol without filtering. (2) F-OFDM with ISI. (3) The circular distortion due to receiver window.

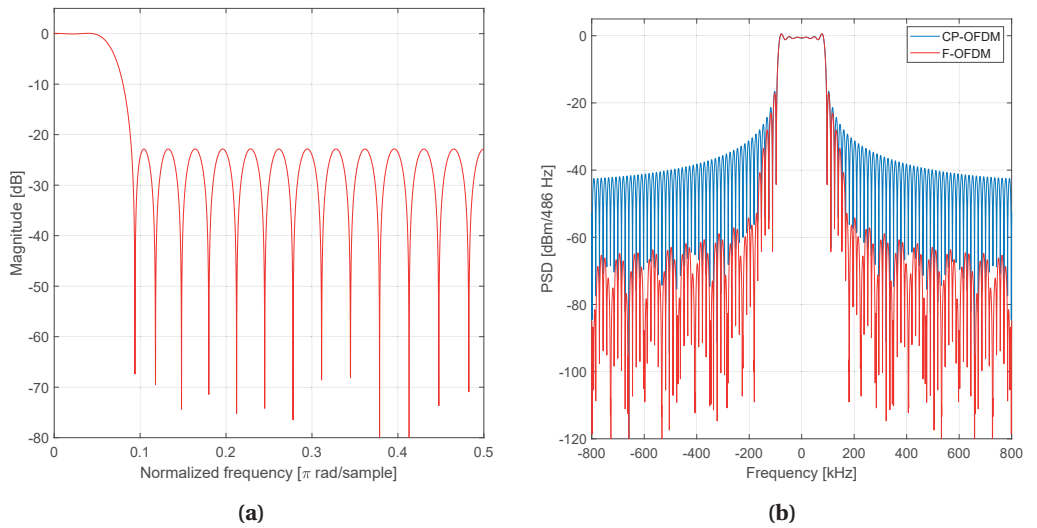


**Figure 2.8:** (a) The magnitude response of linear-phase low-pass filter with 90 kHz pass-band edge, 172.5 kHz stop-band edge, and  $N_h = 33$ . (b) The PSD for 12 subcarriers of CP-OFDM, and F-OFDM with  $N = 128$  and  $N_{CP} = 9$ .

90 kHz, stop-band edge at 172.5 kHz, and magnitude response shown in Figure 2.8(a). Filtering achieves significant reduction in the OOB emissions of CP-OFDM by just using direct filtering by low-order time-domain filter.

The transmitter and the receiver filters provide the spectral shaping at the transmitter side and enhance the detection at receiver side. However, the filtering process smears the symbol extending it from  $N_s$  to  $N_s + N_h - 1$  such that the extension is divided symmetrically on both sides of the symbol [BT07]. Figure 2.7 shows that part of the energy of the filtered symbol in time-domain leaks on the top of the adjacent symbol blocks causing ISI and circular distortion due to lack of circular symmetry [MAK13]. Nevertheless, ISI and the distortion are absorbed by the CP if the filter length is smaller than half of  $N_{CP}$ . This comes at the cost that F-OFDM system is less immune to multipath effects with respect to CP-OFDM [AJM15, CHGH16]. Beside the time-domain effects, the use of the filtering affects the orthogonality of the filtered CP-OFDM, if it is not considered in the filter design. Moreover, the F-OFDM has some limitations in



the cases of the opportunistic use of the spectrum [NGB11]. The spontaneous change in the subband bandwidths and center frequency requires new filter design for each spectral use case. Therefore, modular implementation of the filtering as in RB-F-OFDM is optimal solution for such scenarios.

### 2.3 Computational complexity analyses of CP-OFDM and enhanced-OFDM schemes

The computational complexity is calculated in terms of real multiplication and real addition rates for CP-OFDM, WOLA-OFDM, and F-OFDM schemes. The real multiplication rate and the real addition rate give the number of real multiplications and additions needed per complex input sample, respectively. This metric is a fair measure of the required computational complexity for a specific waveform independent from the number of samples processes per symbol. Moreover, it eases the comparison with other schemes that have different multiplexing patterns in time-domain with respect to frequency domain. As illustrated, the DFT and IDFT are essential ingredient for the OFDM based implementations. Therefore, all of those transforms are assumed to be implemented using split-radix FFT and IFFT algorithm. The split-radix algorithm has been commonly known as non-recursive power-of-two FFT implementations requiring minimum number of multiplications for a given transform length [DH84, SHB86, DH85]. The computational complexity of the FFT or IFFT blocks in terms of number of real multiplications and real additions are evaluated as

$$\mu[N] = N \log_2 N - 3N + 4 \quad (2.11a)$$

$$\alpha[N] = 3N \log_2 N - 3N + 4, \quad (2.11b)$$

respectively. In this document, single complex multiplication is implemented using 3 real multiplication and 3 real additions. This is possible due to the fact that the trigonometric constant (twiddle) factors are already known and saved in the memory of the system. In other alternative realizations, the complex multiplication requires 4 real multiplication and 2 real additions or 3 real multiplication and 5 real addition. Moreover, the multiplications by 0,  $\pm 1$  and  $\pm j$  are trivial multiplications that can be realized without any general multiplications or additions. Besides, the multiplications by  $W_8^{\pm 1}$  and  $W_8^{\pm 3}$  require only 2 real multiplications and 2 real additions. More discussion about the complex multiplications is presented in Appendix A.1.

The implementation of the CP-OFDM transmitter consists mainly of IDFT and CP inclusion. The latter does not require computations leaving the IDFT as the dominant factor of the computational complexity. On the receiver side, the computational complexity is also concentrated in the DFT implementation. The computational complexity ratio for the CP-OFDM scheme is expressed as

$$\mu_{\text{OFDM}}[N, N_a, A_R] = \frac{\mu[N]}{N_a} + 4A_R \quad (2.12a)$$

$$\alpha_{\text{OFDM}}[N, N_a, A_R] = \frac{\alpha[N]}{N_a} + 2A_R, \quad (2.12b)$$

for real multiplication and real addition rates, respectively. Here,  $N_a$  represents the number of processed complex samples per CP-OFDM symbol which is equivalent to the number of active subcarriers. Further,  $A_R$  is receiver modifier that is defined as follow:

$$A_R = \begin{cases} 0, & \text{for transmitter} \\ 1, & \text{for receiver.} \end{cases} \quad (2.13)$$



Here, the receiver modifier is included to generalize the complexity formulas encompassing both transmitters and receivers. In this document, receivers with single-tap equalizer is assumed.

Therefore, the increase in computational complexity rate due to equalization is expected to be marginal compared to the transform complexity.

WOLA-OFDM scheme has similar implementation to CP-OFDM. The number of extra multiplication due to time-windowing is specified by  $N_w$  as seen in (2.6). Besides, the overlap-and-add between consecutive sequences increases slightly the additional rate. However, this increase is insignificant compared to plain CP-OFDM complexity. The computational complexity of the WOLA-OFDM can be expressed as

$$\mu_{\text{WOLA}}[N, N_a, A_R] = \mu_{\text{OFDM}}[N, N_a, A_R] + \frac{4N_w}{N_a} \quad (2.14a)$$

$$\alpha_{\text{WOLA}}[N, N_a, A_R] = \alpha_{\text{OFDM}}[N, N_a, A_R] + \langle A_R + 1 \rangle_2 \frac{4(n_a - 1)N_{\text{EX}}}{n_a N_a} + A_R \frac{4N_{\text{EX}}}{N_a}, \quad (2.14b)$$

for real multiplication and real addition rates, respectively. Here, the second term of the real addition rate represents the computational complexity of the overlapping process between the consecutive WOLA-OFDM symbols in the transmitter. Therefore,  $n_a$  is defined as the number of consecutive transmitted WOLA-OFDM symbols. It is noted here, that the number of overlaps depends on the number of adjacent symbols. Therefore, the overlap is not needed when only one symbol is transmitted, whereas 9 overlaps are needed when 10 symbols are transmitted. The third term of the real addition rate represents also the computational complexity of the overlap process in the receiver. The number of overlaps does not depend on the number of the consecutive symbols considering that the overlap-and-add process at the receiver does not involve adjacent symbols (cf. (2.8)).

The F-OFDM scheme is expected to require significant increase in the computational complexity. This is due to the weighted summation in the filtering process that involves  $N_h$  multiplications (either complex or real) for each processed samples. The increase in the computational complexity is obvious from the computational complexity formula that is expressed as

$$\mu_F[N, N_a, A_R] = \mu_{\text{OFDM}}[N, N_a, A_R] + \frac{2N_h N_s}{N_a} \quad (2.15a)$$

$$\alpha_F[N, N_a, A_R] = \alpha_{\text{OFDM}}[N, N_a, A_R] + \frac{2(N_h - 1)N_s}{N_a}, \quad (2.15b)$$

for real multiplication and real addition rates, respectively. Here, it is assumed that the filter impulse response values (or filter coefficients) are real. Therefore, two real multiplications are needed for the multiplication of real filter coefficient value by complex input sample. In case of complex filter coefficients,  $3N_h(N + N_{\text{CP}})$  real multiplications are required instead of  $2N_h(N + N_{\text{CP}})$ . Furthermore,  $3N_h(N + N_{\text{CP}})$  real additions is added to (2.15b). It should be noted that the CP length is assumed to be fixed in contrast to varying CP length defined in LTE CP-OFDM standard in order to simplify the formulas. Moreover, the effect of varying CP length on the computational complexity is negligible.

### 2.3.1 Numerical results

The computational complexity of the CP-OFDM is illustrated in LTE scenario in Figure 2.9. The transform sizes of 128, 256, 512, 1024, and 2048 are used with 1.4 MHz, 3 MHz, 5 MHz, 10 MHz, and 20 MHz LTE scenarios with subcarrier spacing of 15 kHz and slot duration of

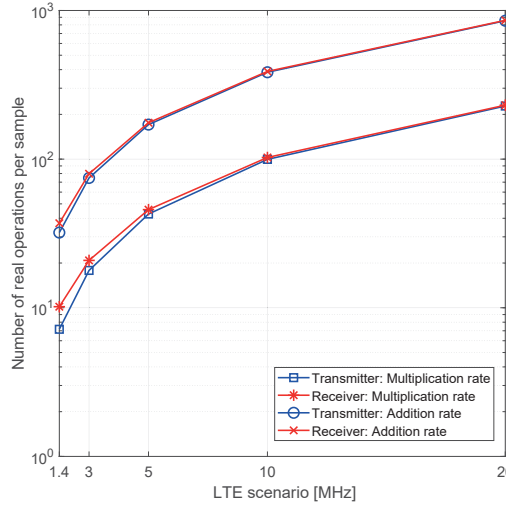


**Figure 2.9:** Real multiplication and real addition rates per transmitted or received sample for CP-OFDM in the transmitter and the receiver with 72 active subcarriers.

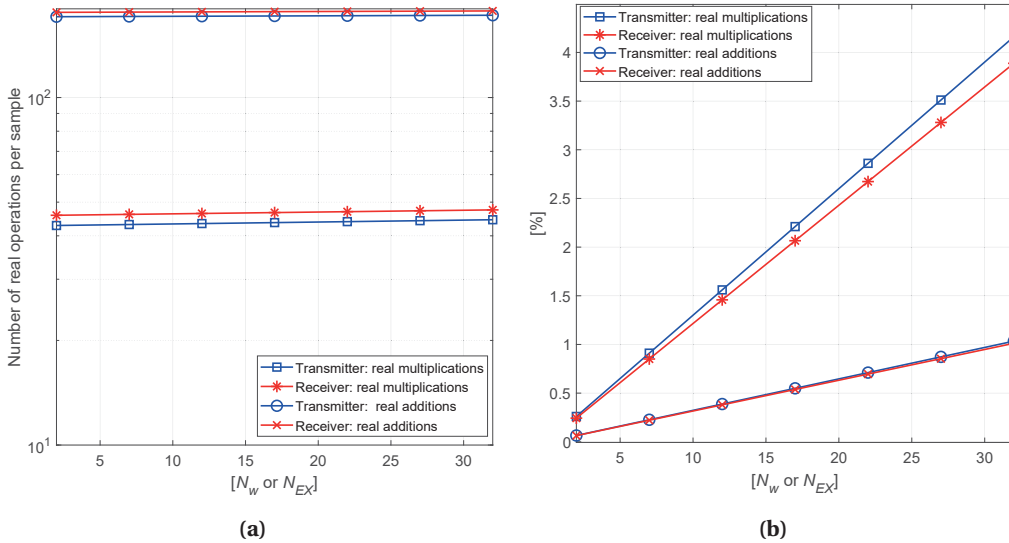


**Figure 2.10:** (a) Real multiplications and real addition per sample for WOLA-OFDM and (b) the ratio of WOLA-OFDM additional complexity to CP-OFDM in percents in the transmitter and the receiver with 72 active subcarriers and 5 MHz LTE scenario.

0.5 ms [3GP18a]. Fixed number of active subcarriers is assumed corresponding to 6 physical resource blocks (PRBs) or  $N_a = 72$  active subcarriers at the transmitter and receiver sides with different LTE scenarios. The results show that the real additions rate is three times the real multiplication rate. This increase is relevant to the FFT complexity (2.11) which shows similar rate increase of real addition with respect to the real multiplications. The difference between the transmitter and the receiver complexities is quite insignificant indicating the dominance of the FFT computational complexity compared to the equalization complexity in the receiver side.

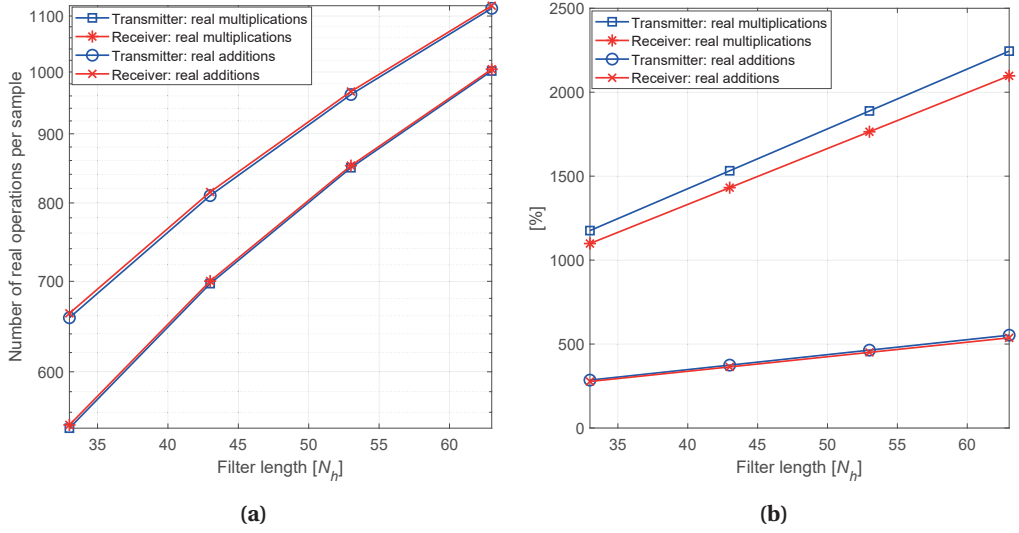


**Figure 2.11:** (a) Real multiplications and real additions per sample for F-OFDM and (b) the ratio of F-OFDM additional complexity to CP-OFDM scheme for CP-OFDM in percents in the transmitter and the receiver with 72 active subcarriers and 5 MHz LTE scenario.

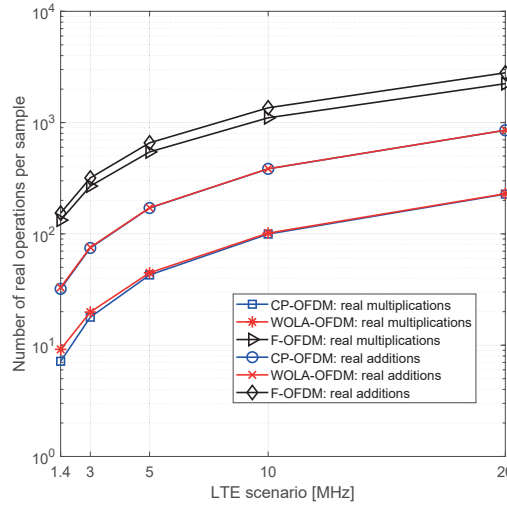


**Figure 2.12:** Real multiplications and real additions per transmitted sample for CP-OFDM, WOLA-OFDM with  $N_w = 36$  and  $N_{EX} = 18$ , and F-OFDM with  $N_h = 33$ . All compared schemes are transmitter cases with 72 active subcarrier.

The second test is related to WOLA-OFDM in 5 MHz case with  $N_a = 72$  active subcarriers. Figure 2.10 shows the effect of the  $N_w$  and  $N_{EX}$  on the computational complexity of the WOLA-OFDM. Both factors contribute to the computational complexity of the transmitter and the receiver side as shown in (2.14). Therefore, real multiplication rates and real addition rates are function of  $N_w$  and  $N_{EX}$ , respectively. Therefore, those factors share  $x$ -axis. In Figure 2.10(a), the computational complexity of WOLA-OFDM is nearly constant regardless of  $N_w$  and  $N_{EX}$ . Figure 2.10(b) shows the increase in the real multiplications and real additions in percentage

with corresponding CP-OFDM configuration. The results show around 4 % increase in the number of real multiplications at  $N_w = 32$ . Therefore, computational complexity is dominated by the transform complexity in WOLA-OFDM implementations.

The same scenario of 5 MHz and 72 active subcarriers is used for evaluating F-OFDM computational complexity. The varying factor in this case is the filter length  $N_h$ . Figure 2.11(a) shows the real multiplication and real addition rates of F-OFDM in the transmitter and the receiver. The results show significant increase in the computational complexity. Figure 2.11(b) shows significant increase in the require real multiplication of F-OFDM by 1000 % to 2000 % with respect to CP-OFDM.

The computational complexity of CP-OFDM, WOLA-OFDM, and F-OFDM are compared in different LTE scenarios in Figure 2.12. The comparison is performed at the transmitter side. Because the difference in the computational complexity between the receiver and the transmitter is marginal. The WOLA-OFDM parameters are chosen to be  $N_w = 36$  and  $N_{EX} = 18$ . The filter length is chosen to be 33 for F-OFDM which gives the lowest complexity in Figure 2.11. The result shows significant increase in the computational complexity of F-OFDM with respect to CP-OFDM and WOLA-OFDM. The increase of the computational complexity occurs though the filter length is chosen to be short. On the other hand, WOLA-OFDM has very close computational complexity to the CP-OFDM and it is expected to have similar complexity even if the window parameters are increased.

## 2.4 Chapter summary

The high OOB emissions of CP-OFDM are due to the block-wise processing that translates to rectangular window in time domain and Dirichlet function in frequency domain. By using WOLA technique, the edges of the rectangular window are relaxed resulting in reduced OOB emissions with up to 4 % additional real multiplications. However, WOLA-OFDM still has quite high OOB emissions in frequencies near the active subcarriers. In this regards, WOLA-OFDM is not sufficient for the 99 % spectrum utilization target in 5G-NR. F-OFDM can achieve significant reduction in the OOB emissions. However, this scheme comes with extreme increase in the computational complexity. Besides, F-OFDM lacks the flexibility to filter the unwanted sidelobes in dynamic spectrum allocations with variable bandwidth. Hence, computationally efficient and flexible schemes with effective OOB reduction are required.

## Fundamentals of Advanced Multicarrier Schemes

The advanced multicarrier schemes based on multirate filtering have been widely considered as key enabler for the 5G-NR wireless systems [LLJ<sup>+</sup>15, ZCQA16, ZMMF17, WJK<sup>+</sup>14, SSE<sup>+</sup>16, ZLG<sup>+</sup>16]. As described earlier, the CP-OFDM scheme is challenged by the new requirements of 5G-NR such as higher spectral utilization and loose synchronicity. Therefore multirate filtering based schemes have been always a strong candidate to replace the CP-OFDM waveform due to their high spectral localization. Generally, multirate filter processing is based on altering the sampling rate using interpolation and decimation. The filtering is needed to remove the spectral images or to prevent the aliasing [Vai93, Rab96]. In this document, the multirate filtering based waveforms are classified to two distinct categories. The first category is based on filtering each subcarrier with sharp filter which reduces significantly the OOB leakage. This category includes the filter bank (FB) based waveforms. The second category is based on multirate filtering each OFDM subband independently. As mentioned earlier in Chapter 2, this category of waveforms is referred as resource block filtered OFDM (RB-F-OFDM).

### 3.1 FBMC waveforms

The basic CP-OFDM scheme produces well time localized waveform with poor localization in frequency domain causing high OOB leakage. This issue has been addressed in Chang's work [Cha66] proposing the use of band-limited waveform. Using set of identical parallel transmission filters but with frequency shifted responses, the pulse amplitude modulation (PAM) signal can be transmitted while maintaining the time-frequency orthogonality condition. This scheme was improved by Saltzberg to transmit staggered quadrature amplitude modulation (QAM) signals using similar idea of identical parallel filters [Sal67] which denoted as staggered-modulated multitone in [FBGY10]. The work of Saltzberg [Sal67] has been improved by efficient implementation of the parallel transmission filter using the polyphase network (PPN) [BD74, BCB78]. Later, the staggering has been referred to as OQAM in [Hir80]. The FB based approaches has been intensively studied in the literature [BDH03, BDH99, CC97, VL01, SSL02] with different alternative approaches. For instance, FMT modulates QAM low-rate signal by partially overlapping filters [CEO99, VT95, Cve95].

FB-based transmitter processing combines multiple low-rate signals into a single wide-band signal using upsampling and frequency-selective filtering. The upsampling of the low-rate input samples results in spectral images that have to be removed by the interpolation filters.

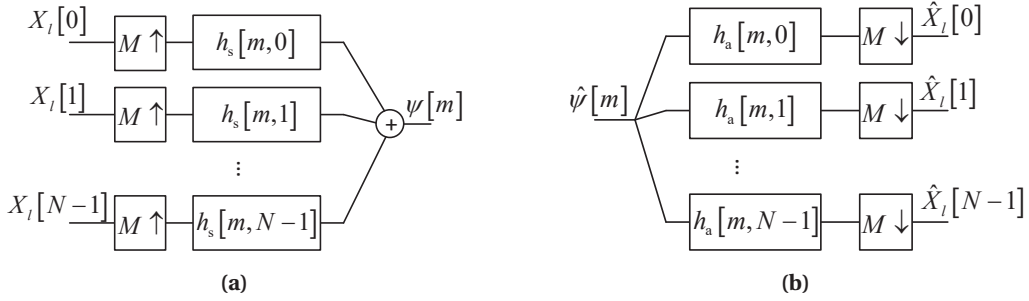


**Figure 3.1:** Implementation of the FB based (a) transmitter and (b) receiver processings with  $N$  subcarriers and interpolation/decimation factor of  $M$

Accordingly, the output of the interpolated signal with  $N$  low-rate inputs can be expressed as

$$\psi[m] = \sum_{k=0}^{N-1} \sum_l X_l[k] h_s[m - Ml, k], \quad (3.1)$$

where  $h_s[m, k]$  is the synthesis filter or the interpolation filter of the  $k$ th subband. Here, the  $k$ th low-rate input signal is upsampled by  $M$  and filtered by  $k$ th interpolation filter  $h_s[m, k]$ . Hence,  $N$  interpolation filters are needed to interpolate  $N$  low-rate signals. This form of FB based scheme is also denoted as synthesis filter bank (SFB). The implementation of the basic FB based transmitter is shown in Figure 3.1(a).

The receiver side processing (also known as analysis filter bank (AFB)) is a dual of the transmitter, as shown in Figure 3.1(b). Here, the incoming high-rate, wide-band signal is to be split into several narrowband signals with adjustable frequency responses and adjustable sampling rates. Therefore, the decimated low-rate output of the AFB could be expressed as

$$\hat{X}_l[k] = \sum_m \hat{\psi}[m] h_a[Ml - m, k], \quad (3.2)$$

where  $\hat{\psi}[m]$  is the received high-rate signal and  $h_a[m, k]$  is the analysis filter or the decimation filter of the  $k$ th subband.

Generally, FB based waveforms can be classified based on the interpolation/decimation factor  $M$  and the number of subbands  $N$ . The critically sampled FB based waveform is the case when the interpolation/decimation factor equals the number of subbands, that is,  $M = N$ . Otherwise, FB based waveform is considered oversampled when  $N > M$ . In [Bel10], it has been shown that OFDM is special case of critically-sampled FB based waveforms such that low-rate inputs are filtered by frequency shifted Dirichlet functions in frequency domain.

The interpolation filter should be sharp enough to remove the spectral images. Besides, the decimation filters should be highly frequency-selective as well to remove the unwanted subbands and to avoid aliasing in downsampling. Figure 3.2 shows the effect of the interpolation and the decimation on the spectral components of critically sampled low-rate inputs. From top to bottom, the low-rate input is upsampled by 4 resulting in 4 images in the spectrum. The filter  $h_s[m, 2]$  removes the folding copies and keeps the wanted image that is centered at  $\pi$ . This implies that the low-rate signal has been frequency shifted by  $\pi$  without modulation. Observing Figure 3.2 from bottom to top, the high-rate input that contains different active subbands is filtered removing other subbands before the downsampling. The downsampling stretches out the frequency axis of the downsampled signal. As a result, the output is the low-rate signal centered at zero frequency.

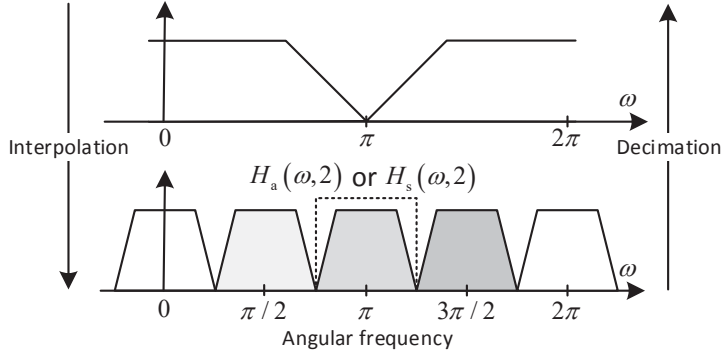


**Figure 3.2:** The spectral components of the low-rate or high-rate input at different stages of the interpolation and the decimation, respectively. Here,  $H_a(\omega, 2)$ , and  $H_s(\omega, 2)$  are amplitude responses of the decimation and the interpolation filters, respectively, for subband of index 2.

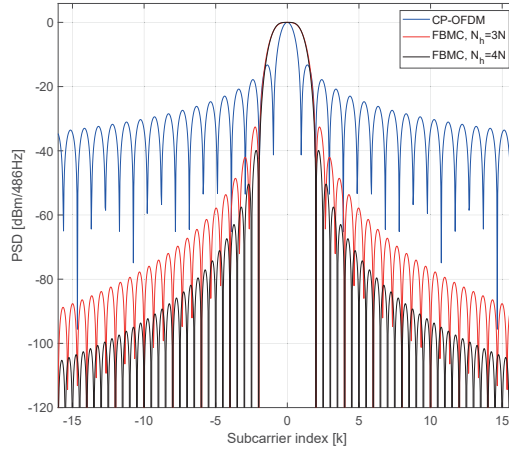


**Figure 3.3:** The PSD of the FB based subband, filter lengths of  $3N$  and  $4N$  with RRC filter of roll-off one, and CP-OFDM subcarrier as reference. The used filter is based on the prototype filter of PHYDYAS project [Bel01].

Usually, the interpolation and decimation filters follow the Nyquist pulse shaping criteria achieving zero ISI at the sample detection range. Therefore, RC filter is a natural choice for this purpose. Accordingly, RC filter can be divided into two root raised cosine (RRC) filters between SFB and AFB achieving Nyquist pulse shaping criteria and acting as matched filter to maximize the SNR at the detected samples. Besides, the filter plays key-role in guaranteeing the orthogonality in time-domain and frequency-domain [SR17]. Due to these critical roles of the synthesis and analysis filters, SFB and AFB filters are typically defined with impulse responses from 3 to 4 times longer than symbol length  $N_h = 3N$  or  $4N$ . Figure 3.3 shows the PSD of a single subband of FB based waveform using RRC with roll-off factor of one compared with PSD of the single OFDM subcarrier. Here, RRC filter is based on the prototype filter designed by PHYDYAS project [Bel01] as it provides the maximum rejection of the images. The OOB emissions of the FB based subband decay in faster rate than the CP-OFDM subcarrier. PSD of the FB waveform at zeroth subband is well below -80 dB in the middle of the  $M/2$ th subband even with  $N_h = 3N$  whereas for CP-OFDM only 30 dB attenuation is achieved.

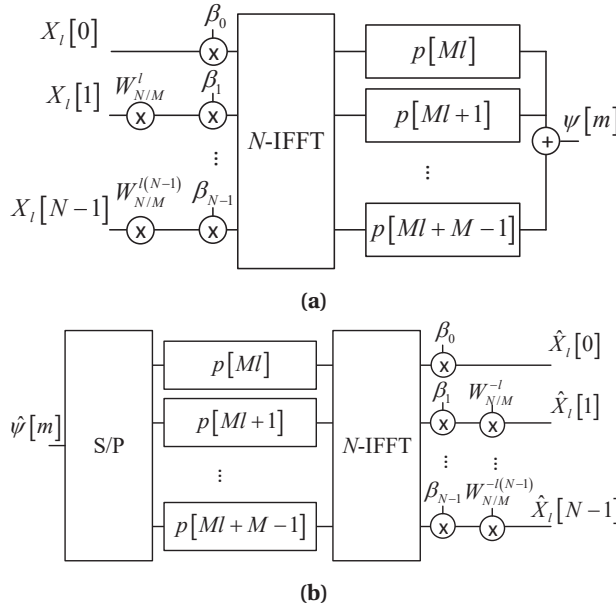


**Figure 3.4:** The implementation of the PPN-FBMC (a) transmitter and (b) receiver.

The generic FB based approach that is shown in Figure 3.1 requires intensive computations to provide sharp interpolation and decimation filters. PPN-based approaches provide computationally efficient solutions for the uniformly distributed FBs [BD74, BCB78]. In other words, interpolation and decimation filters can be expressed in terms of frequency-shifted prototype filters as

$$h_s[m, k] = h_a[m, k] = p[m] \beta_k W_N^{-km}, \quad (3.3)$$

where  $p[m]$  is the prototype low-pass filter and  $\beta_k = W_N^{k(N_h-1)/2}$  is for the delay compensation due to filter causality. The computational complexity of the PPNs can be further reduced by exploiting the FFT in the implementation. Considering (3.3), the expression in (3.1) is reformulated as

$$\psi[m] = \sum_l p[m - ML] \sum_{k=0}^{N-1} X_l[k] \beta_k W_N^{-k(m-ML)}, \quad (3.4)$$

by direct substitution with (3.3). Similarly, substituting (3.3) in (3.2) results in the following way:

$$\hat{X}_l[k] = \beta_k \sum_m \hat{\psi}[m] p[LM - m] W_N^{k(m-ML)}. \quad (3.5)$$

Here, the IDFT and DFT operations appear in (3.4) and (3.5) as sum of the complex exponentials  $W_N^{-km}$  and  $W_N^{km}$ , respectively. Hence, PPN can be implemented with the aid of the IDFT and DFT. The implementation of the transmitter and receiver using FBMC based PPN is shown in Figure 3.4. Moreover, the PPN implementation replaces the direct implementation of the interpolation and decimation filters by decimated version of those filters alongside with IDFT or DFT transforms.

In Figure 3.3, the subbands is clearly not orthogonal with adjacent subcarriers. Therefore, the well localized waveform in time- and frequency-domain lacks the orthogonality with the complex modulated samples in the case of overlapping subcarriers. Actually, the spectral efficiency of FBMC is maximal only when the orthogonality in complex domain is relaxed.



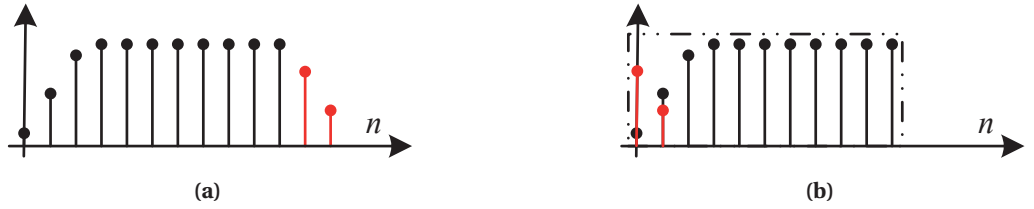


**Figure 3.5:** The spread components as a result of (a) linear convolution and (b) circular convolution, highlighted by red. Moreover, the dash-dotted rectangle represents the CC period.

Actually, according to Balian-Low theorem, the system cannot be well localized in time- and frequency-domains, achieve orthogonality in complex domain, and achieve the maximum spectral efficiency according to Balian-Low theorem [Bal81, low85]. OFDM reaches the spectral efficiency and uses QAM symbol at the cost of poor frequency localization. Therefore, good localization in time- and frequency-domains requires the scarification of the strict complex orthogonality, or the maximum spectral efficiency.

In this context, OQAM based FBMC (FBMC/OQAM) scheme relaxes the complex orthogonality by transmitting the real and imaginary parts of the complex symbols staggered by half symbol period. This decomposition is referred as  $\mathbb{C}2\mathbb{R}$  transformation [SIVR10]. This is followed by the phase rotation of by  $\exp[j\pi/2(l+k)]$ . This phase rotation multiplies by  $\pm j$  on every other subcarrier and symbol. This permits the overlapping between adjacent subcarriers and symbols without interference. In other words, the orthogonality is maintained and maximum spectral efficiency could be reached. On the receiver side, the low-rate output is obtained by taking real components followed by phase rotation, that is  $\exp[-j\pi/2(l+k)]$ . Accordingly, each consequent two symbols can construct single complex symbol.

Another variant of the FBMC is based on using low-rate complex samples sacrificing the maximum spectral efficiency. In FMT, the spectral efficiency is reduced by increasing  $N$  with respect to  $M$ . This leads to an increase in the subcarrier spacing. Accordingly, well localized waveform can be provided with plain QAM modulation by relaxing the spectral efficiency. Generally, the FMT based FBMC provides better ICI than corresponding CP-OFDM due to the increase in the subcarrier spacing [RMKB17]. Moreover, FMT avoids the inconvenience of FBMC/OQAM in pilot based channel estimation or in the MIMO implementations.

### 3.1.1 Fast convolution based FBMC waveforms

The presented FBMC implementations are based on multirate time-domain filtering. The filtering process in time-domain is simply a linear convolution. The other way of the filter implementation is based on frequency-domain filtering. The frequency-domain filtering is implemented by multiplying the frequency components of the input signal by the frequency components of the filter. Then, the filtered signal is obtained by transforming the resulted frequency-domain multiplication to time-domain, representing CC process. The CC process is basically similar to the linear convolution in such way that it is the weighted sum of input samples. Generally the linear convolution process spreads the filtered signal in time-domain by  $N_h - 1$  samples, i.e., the filtered signal length is  $N_x + N_h - 1$ , where  $N_x$  is input signal length. On contrary, the CC spreads components to the beginning of the filtered sequence in causal systems. The number of the overlapping components depends directly on the length of CC. Figure 3.5 shows the spreaded components in time-domain as a result of linear convolution and circular convolution. The time-spread adds up to the beginning of the signal in circular

convolution rather than spreading the signal in the linear convolution.<sup>1</sup> Therefore, extending the CC period to equal the linear convolution can make the CC equivalent to the linear convolution. As a result, linear convolution could be performed in frequency-domain in such a way that it is equivalent to the time-domain filtering.

Typically, DFT and IDFT processes are used for the time-to-frequency and frequency-to-time transformation for finite discrete sequences, respectively. Consequently, the length of the DFT and IDFT should be at least  $N_x + N_h - 1$ . However, the discrete input signal is usually long sequences requiring very long transforms to perform frequency-domain filtering. Therefore, the long sequences are broken down to relatively short blocks to shorten the required transform sizes. The concatenation of the shortened blocks is performed using two techniques, namely, overlap-and-save (OLS) and OLA. OLA is based on appending  $N_h - 1$  samples to the input block of length  $N_b$ . This is followed by applying DFT of size  $N_b + N_h - 1$ . Consequently, the output of the DFT is multiplied by stored DFT components of the filter. Then, IDFT is applied on resulted multiplication. The output of the IDFT is overlapped and added with  $N_h - 1$  samples of the following block. For OLS technique, input block is overlapped with  $N_h - 1$  samples of the following block. Then, DFT of size  $N_b + N_h - 1$  is applied on the overlapped blocks. The output of the DFT is multiplied by the DFT components of the filter that is followed by IDFT of size  $N_b + N_h - 1$ . Then,  $N_h - 1$  samples of the output block are removed. Figures 3.6(a) and 3.6(b) show the OLA and OLS processings before and after the DFT and IDFT. These processes of performing linear convolution in frequency-domain are commonly denoted as FC. One important aspect of the FC processing that it still involves the CC equivalent as depicted in Figure 3.6(c).

The involvement of the FC processing in the multirate filtering has shown significant reduction in the terms of computational complexity as proposed in [MK97]. The FC processing has been used for the implementation of AFBs in [BMF99, ZW00]. The FC processing has been exploited in [Tom05] for frequency-domain decision feedback equalization considering single carrier transmission. The implementation of multirate filtering using OLS-FC has been also discussed in [Bor06] providing the recommendations for proper parameterization of the FC transforms. The involvement of the FC in FB based multicarrier scheme has been later proposed in [UT10, TUIT09]. The implementation of the FC as non-uniform filter-bank and the filter design has been proposed in [RH11]. In [Bel10, Bel12b], frequency spreading concept has been proposed which could be considered as special case of the filter-bank based on FC processing. The proposed scheme, which is named frequency spreading (FS)-FBMC, emulates the exact FBMC waveform using OLA at the transmitter and OLS at the receiver. This scheme provides simple frequency shifting, simplified equalization, and straight-forward time-offset compensation [Bel12a]. Moreover, it has been suggested to be used in the opportunistic spectral use [BDN14a, BDN14b]. However, such scheme requires higher computational complexity than PPN-FFT realization. Therefore, a reduced computational complexity version of FS-FBMC has been proposed in [MTB12] with the trade-off in the spectral localization. The generalized form of the FC based FBMC has been proposed in [RYH14] which has been denoted as FC-FB. Generally, FC-FB scheme shows reduced computational complexity with respect to PPN-FBMC by shortening the CC period including circular components. This results in controllable amount of circular interference. Besides, the scheme has proven its reliability in terms of channel equalization [RY14a, RY14b, ZWG15], in heterogeneous scenarios [YR13, SAYR15, YR15a, YR14a], and time offset compensation [RY13]. In [SPYR17, SYLR18], FMT based FC with overlapped subbands has been studied showing significant increase in the

<sup>1</sup>It is also possible to rearrange the circular convolution process in such way that the spread overlap is at the beginning and the end of the symbol as in the low-pass non-causal filtering case.

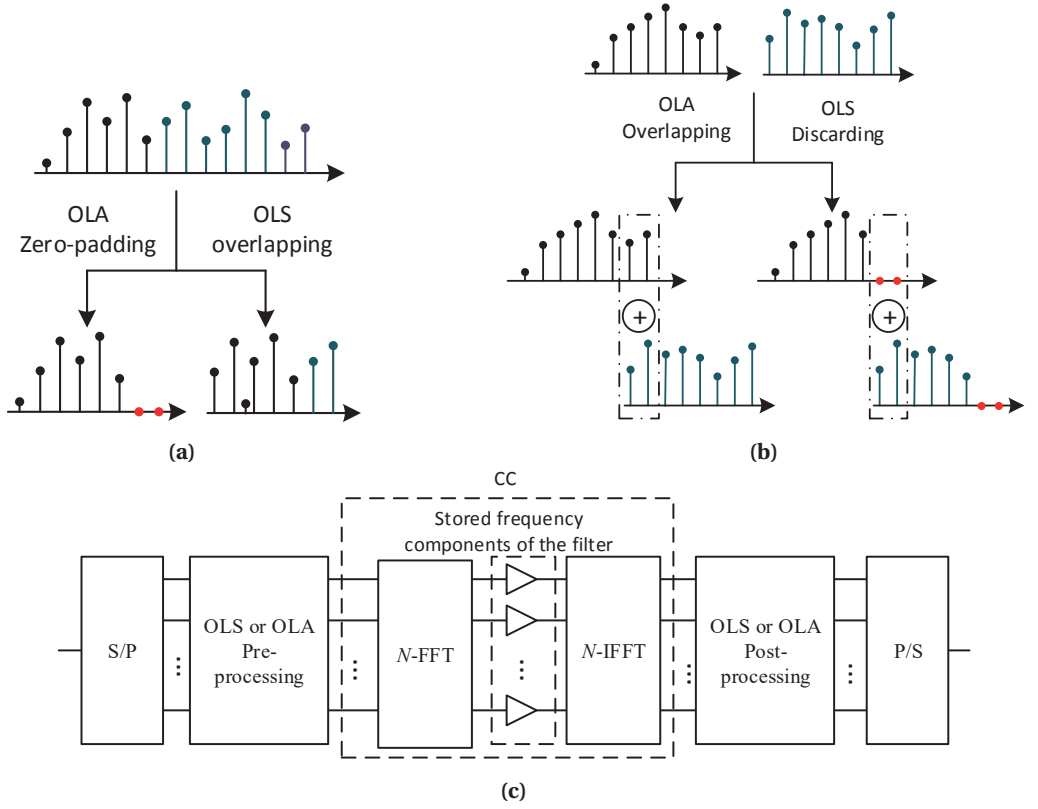


**Figure 3.6:** The generic implementation of the FC filtering showing (a) the pre-processing for OLS and OLA, (b) the post-processing for OLS and OLA, and (c) the full FC processing.

spectral efficiency. The subband representation and the filter optimization of FC-FB have been discussed further in [YR14b, YR15b, YKR16, YR18].

Here, the FC model in [RYH14] is discussed and analyzed due its generality and flexibility in describing a wide range of FBMC based FC variations. Firstly, the low-pass model of the FC is used.<sup>2</sup> Therefore, the discarding, zero-padding and overlapping process are performed at the beginning and the end of the FC block. The low-rate input symbol is firstly divided to blocks considering OLA and OLS as

$$c_l[s, \kappa] = x \left[ s + lL_b^{(\kappa)} - \left\lfloor \frac{L_o^{(\kappa)}}{2} \right\rfloor, \kappa \right] w_{FC} [s, L^{(\kappa)}, A_{OV1}], \quad (3.6)$$

where  $x[r, \kappa]$  is the low-rate serial sequence of the  $\kappa$ th subband with the time index of the serial sequence  $r$  and defined as  $x[r, \kappa] = 0$  for  $r < 0$ ,  $s = 0, 1, \dots, L^{(\kappa)} - 1$  is the time index of the  $\kappa$ th subband and  $l$ th FC block for the parallel sequence  $c_l[s, \kappa]$ ,  $L_o^{(\kappa)}$  is the low-rate overlapping period or the time extension of the multirate FC process considering that  $L^{(\kappa)} = L_b^{(\kappa)} + L_o^{(\kappa)}$ ,  $L$  is the low-rate length of the CC or the short transform size, and  $L_b^{(\kappa)}$  is the non-overlapping part of the low-rate FC block. Here,  $w_{FC} [s, L^{(\kappa)}, A_{OV1}]$  is a rectangular time-domain window that is defined according to  $A_{OV1}$  such that  $A_{OV1} = 0$  for OLS and  $A_{OV1} = L_o^{(\kappa)} / 2$  for OLA. Therefore,

<sup>2</sup>Causal FC implementation is also possible with FC-FB.

the FC window is defined as follows:

$$w_{\text{FC}}[s, L^{(\kappa)}, A_{\text{OV1}}] = \begin{cases} 1, & \text{for } \lfloor A_{\text{OV1}} \rfloor \leq s \leq L^{(\kappa)} - \lfloor A_{\text{OV1}} \rfloor - 1 \\ 0, & \text{otherwise.} \end{cases} \quad (3.7)$$

Here, overlapping FC blocks are generated using (3.6) which suits only OLS processing. Therefore, FC window (3.7) is needed to remove the overlapping parts and represent the zero-padding for OLA processing.

The low-rate parallel samples  $c_l[s, \kappa]$  are considered as the input of the multirate CC process. Then, DFT of size  $L^{(\kappa)}$  is applied as

$$C_l[k', \kappa] = \sum_{s=0}^{L^{(\kappa)}-1} c_l[s, \kappa] W_{L^{(\kappa)}}^{-jL_b^{(\kappa)} k'_0} W_{L^{(\kappa)}}^{s k'}, \quad (3.8)$$

where  $k' = 0, 1, \dots, L^{(\kappa)} - 1$  is the DFT index for the low-rate CC input. Here,  $W_{L^{(\kappa)}}^{-jL_b^{(\kappa)} k'_0}$  is phase rotation that is need for the phase continuity between FC blocks due to partly overlapping processing. Then, the low-rate is upsampled in the DFT-domain by directly copying the data in such a way that number of copies equals the required interpolation ratio. Considering the upsampling from  $L^{(\kappa)}$  samples to  $N$  samples per FC block, the interpolation factor is defined as follows:

$$R^{(\kappa)} = \frac{N}{L^{(\kappa)}}. \quad (3.9)$$

Moreover, frequency shift can be applied simply by circularly shifting the high-rate DFT response of the signal. Consequently, filtering can be applied using the multiplication on the frequency domain by the DFT components of the filter (frequency-domain mask). Hence, filtering removes the unwanted images at the wanted center frequency. Generally, the frequency-domain mask provides another mean of controlling the upsampling rate by the modification of the number of zero components in the mask. In practical implementations, the outputs of the short transforms are multiplied directly by the corresponding non-zero DFT components of the frequency-domain mask of length  $L_H$ . The result of the multiplication by the frequency-domain mask are found as

$$Y_l[k, \kappa] = H_s[k, \kappa] C_l[\langle k - k'_0 \rangle_N, \kappa], \quad (3.10)$$

where  $k'_0$  is the center frequency and  $H_s[k, \kappa]$  is the frequency-domain mask of the low-pass filter both for the  $\kappa$ th subband. The above processes are performed  $K$  times for each subband where  $K$  is the number of subbands. Each subband could have different short transform sizes, filter masks and interpolation/decimation factors.

The final step in the FC process includes the combination of the different filtered subbands and obtaining the output of the multirate CC using IDFT as follows:

$$y_l[n] = \sum_{k=0}^{N-1} \sum_{\kappa=0}^{K-1} Y[k, \kappa] W_N^{-kn}. \quad (3.11)$$

Consequently, the post FC operation is applied as

$$\psi[m] = \sum_l y_l[m - N_b l] w_{\text{FC}}[m - N_b l, N, A_{\text{OV2}}], \quad (3.12)$$

where  $N_b$  is the non-overlapping length at the high-rate output such that  $N = N_b + N_o$ ,  $N_o$  is the overlapping length at the high-rate output and  $w_{\text{FC}}[m - N_b l, N, A_{\text{OV2}}]$  is defined using (3.7) with  $A_{\text{OV2}} = 0$  for OLA and  $A_{\text{OV2}} = N_o/2$  for OLS.

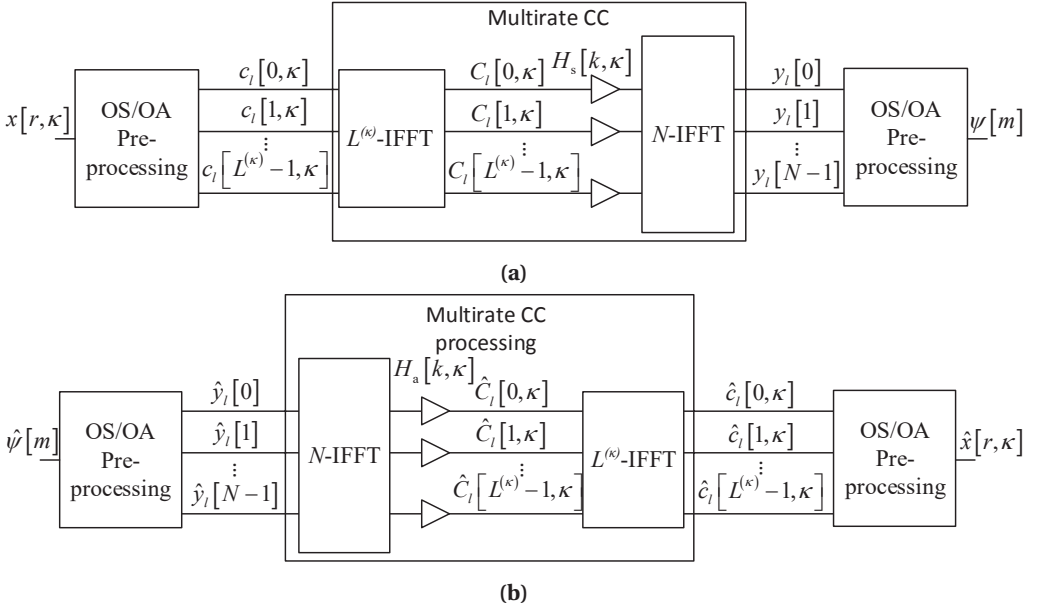


**Figure 3.7:** The generic implementation of the FC-FB showing (a) the transmitter, and (b) the receiver. The processing of single subband is shown for simplicity. More subbands could be processed in similar way as illustrated.

Regarding FC-FB at the receiver, the received signal is overlapped or zero-padded as follows:

$$\hat{y}_l[n] = \hat{\psi} \left[ n + lN_b - \left\lfloor \frac{N_0}{2} \right\rfloor \right] w_{\text{FC}}[n, N, A_{\text{OV1}}]. \quad (3.13)$$

Consequently, DFT of size  $N$  is applied for each FC block in the following way:

$$\hat{Y}_l[k] = \sum_{n=0}^{N-1} \hat{y}_l[n] W_N^{kn}. \quad (3.14)$$

The input of the DFT is the input of the CC processing on the receiver side. Then, the DFT response of the input signal is masked by the DFT components of the filter in the following way:

$$\hat{C}_l[k, \kappa] = H_a[k, \kappa] \hat{Y}_l[\langle k + k_o^{(\kappa)} \rangle_N]. \quad (3.15)$$

The frequency-mask removes the unnecessary components outside the  $\kappa$ th subband. The filtered high-rate samples are returned to the time-domain and decimated using short DFT of size  $L$  as follows:

$$\hat{c}_l[s, \kappa] = W_{L^{(\kappa)}}^{L_b^{(\kappa)} k_o^{(\kappa)}} \sum_{k=0}^{L^{(\kappa)}-1} \hat{C}_l[k, \kappa] W_{L^{(\kappa)}}^{-sk}. \quad (3.16)$$

Finally, the low-rate CC output is processed as follows:

$$\hat{x}[r, \kappa] = \sum_l \hat{c}_l \left[ r - L_b^{(\kappa)} l \right] w_{\text{FC}}[r - L_b^{(\kappa)} l, L^{(\kappa)}, A_{\text{OV2}}]. \quad (3.17)$$

The implementation of the FC-FB transmitter and receiver is shown in Figure 3.7. The illustrated figure shows the processing of single subband. More bands could be processed

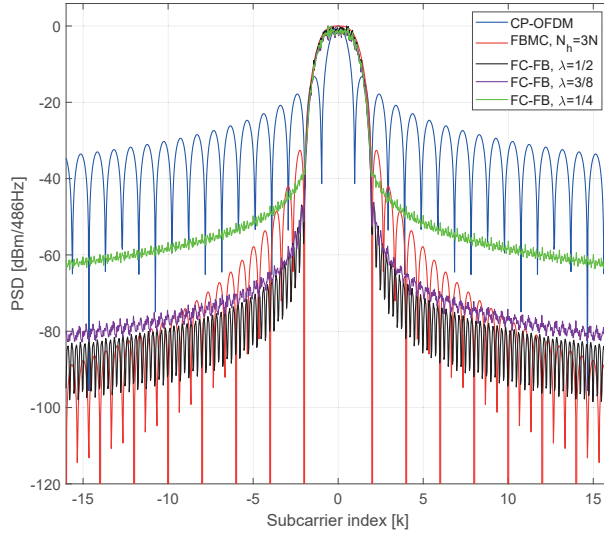


**Figure 3.8:** PSD of FC-FB subband with different values of overlapping factor  $\lambda$ . The PSDs of single subcarrier for CP-OFDM and FBMC are shown for reference.

considering (3.11) and (3.15). In the case of overlapping subbands, the subbands are simply added using (3.11). However, only filtering is used to separate the different subbands from each other on the receiver side as in (3.14).

FC-FB scheme accepts some amount of circular interference by not satisfying the linear convolution condition. Because following the linear convolution condition leads to unrealistic sizes of long transform, increasing intensively the computational complexity of the scheme. The frequency spreading FBMC (FS-FBMC) scheme is an example of such case, knowing that linearity condition is satisfied with significant increase in the computational complexity. Therefore, FC-FB waveform allows the control of the circular interference, considering the overlapping factor  $\lambda$  as follows:

$$\lambda = \frac{L_o^{(\kappa)}}{L^{(\kappa)}} = \frac{N_o}{N}. \quad (3.18)$$

Here, it is indicated that  $\lambda$  must be constant in low-rate and high-rate sides. The effect of the circular interference appears as slight increase in the OOB emissions of the subbands. Figure 3.8 shows PSD of a single subband of FC-FB with different values of  $\lambda$ . Moreover, FBMC and CP-OFDM subcarriers are represented as reference. It is assumed also a two times oversampling case for both FBMC and FC-FB schemes. It is shown that the OOB emissions of the FC-FB increases with the increase of  $\lambda$ . However, this increase is tolerable considering that the OOB is around  $-55$  dB for highest value of  $\lambda$ . Generally,  $\lambda$  controls the number of processed samples per FC block. As a result, small value of  $\lambda$  leads to increase in the computational complexity rate. Therefore, the overlapping factor  $\lambda$  determines the trade-off between OOB emission and computational complexity rate. Finally, the short transform size  $L^{(\kappa)}$  should be in multiple integer of  $N/\gcd(N, N_b)$ . This condition is needed to keep the short transform size in integer number with respect to long transform alongside the condition (3.18).

### 3.2 Resource block based F-OFDM waveforms

Filtering CP-OFDM scheme as presented in Subsection 2.2.2 suppresses the OOB emissions of the CP-OFDM effectively. However, this gain comes with 100 times increase in the computational complexity compared to CP-OFDM, as depicted in Figure 2.11 (b). Additionally, F-OFDM lacks the flexibility when the active bandwidth changes. The change in the used bandwidth while transmitting or receiving requires new filter designs. Alternatively, pre-designed filter coefficients could be stored in the communication device for potential changes in the active bandwidth. These options are not feasible in practical implementations considering the added computational complexity for filter design or the massive number of possibilities for storing filter coefficients. In other words, using a single filter for CP-OFDM waveform could not secure low OOB emissions, specially, in the non-contiguous and spontaneous use of the spectrum.<sup>3</sup> In [LKBY13], a flexible time-domain filtering based scheme has been proposed for flexible OOB reduction. This idea is based on modular subband-wise filtering that exploits multirate processing to reduce the computational complexity, in UE. This idea has been discussed in many 3GPP reports [KLS14, CHGH16, YX17]. Different aspects of the RB-F-OFDM have been discussed in the literature in details [GWT<sup>+</sup>17, ZIX<sup>+</sup>18, HMK<sup>+</sup>17, YX17, BKW<sup>+</sup>17, ADB17]. In this section, the discussion is concerned more with the implementation aspects. The acronym RB-F-OFDM is chosen to differentiate this scheme from the traditional F-OFDM. The RB is chosen considering the LTE parameterization that each subband consists of 12 subcarriers (PRBs).

Basically, CP-OFDM scheme is a linear operation such that each subband or group of subbands could be processed independently. Meaning that, each group of subcarriers can be processed using independent transforms, then, they can be added at the output. Actually, the linearity of the CP-OFDM scheme has been exploited in edge-windowing technique [SA11a]. Similarly, RB-F-OFDM is based on dividing the subbands to  $K$  groups of subcarriers each containing  $L_r^{(\kappa)}$  subcarriers where  $\kappa$  is the subband index. Consequently, the transform of size  $N$  could be replaced by smaller transform of size  $L_O^{(\kappa)}$ , upsampling (decimation for receiver) by factor  $R^{(\kappa)} = N/L_O^{(\kappa)}$  and then filtering. Therefore, a single short transform with interpolator/decimator could be sufficient in UE. Usually, UEs transmission and receiving contains a single subband transmissions.

Starting with the transmission, the  $\kappa$ th subband that contains  $L_r^{(\kappa)}$  active subcarriers is modulated using low-rate CP-OFDM modulator as

$$x_l[n_O, \kappa] = \sum_{s_O = -\left\lfloor \frac{L_r^{(\kappa)}}{2} \right\rfloor}^{\left\lceil \frac{L_r^{(\kappa)}}{2} \right\rceil - 1} X_l \left[ \langle s_O \rangle_{L_O^{(\kappa)}}, \kappa \right] W_{L_O^{(\kappa)}}^{-s_O \left( n_O - L_{CP}^{(\kappa)} \right)}, \quad (3.19)$$

where  $n_O = 0, 1, \dots, L_s^{(\kappa)} - 1$  is the low-rate time index of the  $l$ th symbol and  $\kappa$ th subband,  $L_s^{(\kappa)} = L_{CP}^{(\kappa)} + L_O^{(\kappa)}$  is the length of the low-rate CP-OFDM symbol, and  $L_{CP}^{(\kappa)}$  is the length of the low-rate CP. The subcarriers are arranged around zero bin to represent a low-pass model of the signal. Therefore, significant reduction in the computational complexity can be achieved. Consequently, parallel to serial operation is applied as

$$y[s_s, \kappa] = \sum_l x_l \left[ s_s - lL_s^{(\kappa)}, \kappa \right], \quad (3.20)$$

<sup>3</sup>Transmit and receive filter is used in practical implementations of CP-OFDM for signal reconstruction and anti-aliasing purposes.



where  $s_s$  is the serial low-rate time index. Then, the low-rate CP-OFDM is interpolated using low-pass filter with  $R^{(\kappa)}$  interpolation factor. Then, this is followed by frequency shift as

$$\psi[m] = \sum_{\kappa=0}^{K-1} W_N^{-mk_o^{(\kappa)}} \sum_{s_s} y[s_s, \kappa] h_t[m - R^{(\kappa)} s_s, \kappa], \quad (3.21)$$

where  $k_o^{(\kappa)}$  is the center frequency of the  $\kappa$ th subband. Frequency shift is needed to modulate the center frequency to  $k_o^{(\kappa)}$ . Because the center frequency before the filtering (3.21) is at zeroth bin as in (3.19). However, it is also possible to use bandpass filter and avoid the frequency translation  $W_N^{-mk_o^{(\kappa)}}$ . This leads to more complex scheme and limitation in the scheme flexibility.

On the receiver side, the incoming high-rate sequence is the firstly frequency shifted, filtered and downsampled as follow:

$$\hat{y}[s_s, \kappa] = \sum_m \hat{\psi}[m] W_N^{mk_o^{(\kappa)}} h_r[s_s - mR^{(\kappa)}, \kappa]. \quad (3.22)$$

Then, the decimated sequence is fed to CP-OFDM demodulator starting with parallel-to-serial and CP removal as

$$\hat{x}_l[n_O, \kappa] = \hat{y}[n_O + L_{CP}^{(\kappa)} + lL_s^{(\kappa)}], \quad (3.23)$$

where  $n_O = 0, 1, \dots, L_O - 1$  is the time-index of the  $l$ th block and  $\kappa$ th subband. Then low-rate DFT is applied as follows:

$$\hat{X}_l[s_O, \kappa] = \sum_{n_O=0}^{L_O^{(\kappa)}-1} \hat{x}_l[n_O] W_{L_O^{(\kappa)}}^{s_O n_O}. \quad (3.24)$$

The received subcarriers should be in the range  $\left[L_O^{(\kappa)} - \left\lfloor L_r^{(\kappa)} / 2 \right\rfloor, -1\right] \cup \left[0, \left\lfloor L_r^{(\kappa)} / 2 \right\rfloor - 1\right]$  according to the subcarriers allocation in (3.19). The implementation of the RB-F-OFDM is shown in Figure 3.9.

Basically, the length of low-rate CP-OFDM symbol, which is  $L_s^{(\kappa)}$ , should be a factor of the high-rate length of CP-OFDM symbol  $N_s$ , i.e.,  $L_s^{(\kappa)} = N_s / R^{(\kappa)}$ . Therefore, the choice of the  $L_O$  is governed by  $L_{CP}^{(\kappa)}$  and the  $L_r^{(\kappa)}$ , considering that the choice of the  $L_O^{(\kappa)}$  affects directly the interpolation/decimation factor  $R^{(\kappa)}$ . Basically, the transform of the low-rate OFDM should be greater than the number of the active subcarriers in the subband, i.e.,  $L_O^{(\kappa)} \geq L_r^{(\kappa)}$ . However, the CP length is not usually a factor of the transform size. Therefore, low-rate CP could have non-integer value. For example, the 5 MHz LTE scenario has CP length of 36 samples with transform size of 512. In the case of  $L_r^{(\kappa)} = 12$ , if  $L_O^{(\kappa)} = 16$ , the interpolation/decimation factor is  $R^{(\kappa)} = 32$  with corresponding low-rate CP of  $L_{CP}^{(\kappa)} = 1.125$  samples. This non-integer low-rate CP could not be implemented directly. Therefore, CP length should be considered in the configuration of  $L_O^{(\kappa)}$ . This limitation on  $L_O^{(\kappa)}$  could be formulated as follows:

$$\max\left(2^{\left\lceil \log_2 L_r^{(\kappa)} \right\rceil}, \frac{N}{\gcd(N, N_{CP})}\right) \leq L_O^{(\kappa)} \leq N. \quad (3.25)$$

Accordingly, the minimum transform size of the low-rate OFDM is 128 in 5 MHz LTE scenario with  $L_r^{(\kappa)} = 12$ .

Generally, the transition band of the filter causes ICI with adjacent subbands. Therefore, filters with very sharp transition band could be used with long impulse response. However, this



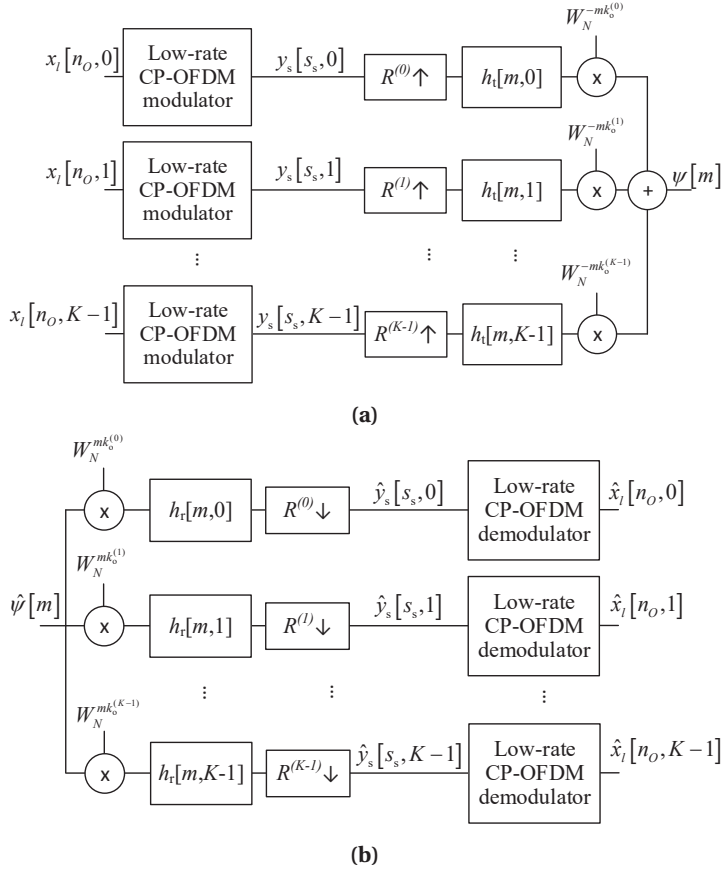


**Figure 3.9:** The implementation of the RB-F-OFDM showing (a) the transmitter, and (b) the receiver.

solution potentially increases the computational complexity significantly. Furthermore, considerable ISI and circular interference are expected at the RB-F-OFDM waveform. Therefore, filters with more relaxed transition bands could be used assuming guard-band between the adjacent filtered subbands. However, this comes with the cost of reduction in the spectral efficiency. Alternatively, the ICI could be tolerated with sufficient equalization at the receiver side.

### 3.2.1 RB-F-OFDM variants

In the literature, many forms of RB-F-OFDM have been proposed in order to provide significant reduction in the OOB emissions, ISI or reduce the computational complexity. UPMC is one of the most commonly studied forms of the RB-F-OFDM [VWS<sup>+</sup>13]. UPMC is distinguished from RB-F-OFDM by two basic features. Firstly, the use of zero prefix (ZP) instead of the CP to absorb the filter tail. Secondly, the filter is designed in such way that filter tail is shorter than the ZP. The receiver of UPMC could be implemented using double size DFT for better compatibility with the OFDM receiver [WWSF14]. This variant is also proposed to overcome the sensitivity of CP-OFDM to carrier frequency offset (CFO) [VWS<sup>+</sup>13]. However, the lack of CP in UPMC makes the time-offsets more destructive if it is not considered in the filter design of the UPMC waveform [WWS15]. Moreover, this scheme has been suggested for short burst

communications [SW14, SWC14]. However, the limitation on the filter length shows increase in the OOB emissions of the UPMC with respect to RB-F-OFDM [AJM15, ZJC<sup>+</sup>15]. Moreover, it has been shown in [AJM15] that RB-F-OFDM has outperformed UPMC in terms of block error rate (BLER) in typical urban channel.

As discussed earlier, RB-F-OFDM is based on multirate filtering. The use of multirate filtering allows for the exploiting of the PPN in the RB-F-OFDM filtering [ZL10, ZL12]. This scheme was denoted as FFT-FBMC. This scheme has been proposed as modified PPN-FBMC scheme that it can exploit CP to simplify the MIMO implementation. Basically, the orthogonality of this system is guaranteed by oversampling the low-rate CP-OFDM by two at the input of the FBMC in similar way as in OQAM. Later, PPN based scheme has been proposed as low-complexity solution for RB-F-OFDM in [LBY14]. This proposed scheme is similar to the FFT-FBMC scheme with one difference. This difference is the dependence on the filters to guarantee small interference with adjacent subbands. Block-filtered OFDM is a modified version of the FFT-FBMC scheme in such way that pre-distortion is introduced to the transmitter filter with special arrangement of the active subcarriers [DGD<sup>+</sup>17]. The main advantage of this scheme is the removal of the filtering at the receiver side with DFT size extension. Another approach is based on dividing the RB-F-OFDM process into CC and CP filtering part [PP19]. The CP processing part is performed used linear convolution and CC part is filtered using DFT/IDFT. Similar technique has been seen earlier in [NNB18] to simplify the implementation of the RB-F-OFDM and more specifically UPMC.

### 3.2.2 FC-F-OFDM

The idea of exploiting multirate behaviour of the RB-F-OFDM has been extended from the PPN based implementation to FC based implementation in [RYL<sup>+</sup>15]. The proposed scheme is denoted as FC-F-OFDM scheme which modulates the low-rate CP-OFDM as a single carrier based FC with two times oversampling. Moreover, the size of the low-rate OFDM transform is equivalent to the size of the FC short transform, i.e.  $L_O^{(k)} = L^{(k)}$ . This condition has been relaxed [RYLV16] to

$$\frac{L_O^{(k)} + L_{CP}^{(k)}}{L^{(k)}} = \frac{N_s}{N}, \quad (3.26)$$

where  $N_s$  is the desired length of the CP-OFDM symbol and  $N$  is the size of the long transform. Besides,  $L^{(k)}$  should be factor of  $N / \gcd(N, N_s)$  to guarantee integer short transform size and  $L^{(k)}$  should be bigger than subband bandwidth. These ideas have been further examined in [YLRV17, YLV<sup>+</sup>17] showing the possibility of implementing RB-F-OFDM with critically sampled FC-FB model. Moreover, FC-F-OFDM has proven superior performance in time-frequency asynchronous and mixed numerology scenarios. In [OUWT18], FC-F-OFDM is employed on the receiver side while transmitter side is implemented using WOLA-OFDM.

Basically, the mathematical analyses of FC-F-OFDM are the combination of FC-FB and RB-F-OFDM discussed in Section 3.2 and Subsection 3.1.1. On the transmitter side, the low-rate input is firstly processed according to (3.19) creating low-rate CP-OFDM symbols of length  $L_O^{(k)} + L_{CP}^{(k)}$ . For mathematical simplicity, the serial-to-parallel process is applied according (3.20). Then, the FC formulas of (3.6), (3.8), (3.10), and (3.12) are applied as typical FC-FB scheme with the same considerations. Similarly for the receiver side, the multirate filtering is applied according to (3.13), (3.14), (3.15), (3.16), and (3.17). The low-rate filtered received complex sequence is then fed to the low-rate CP-OFDM demodulator according to (3.23) and (3.24). Figure 3.10 compares the PSDs of RB-F-OFDM and FC-F-OFDM schemes with CP-OFDM as reference. The filtering schemes are parameterized to transmit single PRB with 180 kHz pass-band filter (assuming 15 kHz subcarrier spacing (SCS)). CP is assumed to be

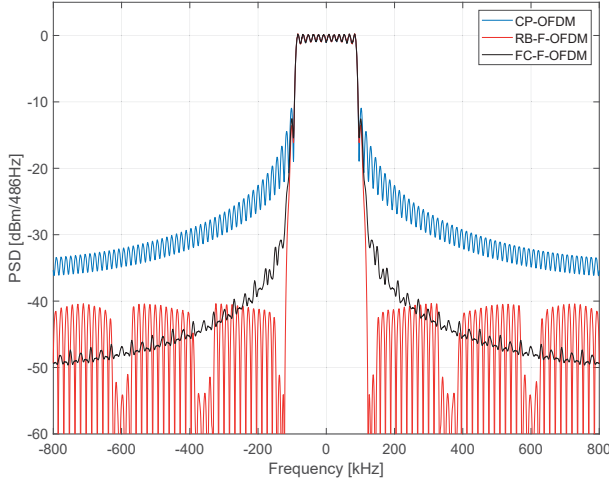


**Figure 3.10:** PSD of PRB transmitted using FC-F-OFDM and RB-F-OFDM schemes. The PSD of CP-OFDM is shown as reference.

8 samples to permit the use of reduced size transform in RB-F-OFDM. For RB-F-OFDM, the used filter is low-pass linear-phase filter with pass-band edge at 90 kHz, stop-band edge at 121.5 kHz, pass-band ripple of 0.01, stop-band ripple of 0.01, and  $N_h = 120$ . In FC-F-OFDM, the pass-band of the filter is simply implemented in frequency domain by assigning ones at the corresponding DFT bins of the active subcarrier locations. Moreover, the transition band is two DFT bins weighted by Hanning window coefficients. Therefore, the short transform size is 16 DFT bins with  $\lambda = 0.5$ . In general, the PSD of FC-F-OFDM has lower OOB emissions than RB-F-OFDM. However, RB-F-OFDM shows lower OOB emissions compared to FC-F-OFDM in the frequency range below 100 kHz from the active RB.

Basically, the parameterization of the low-rate CP-OFDM in (3.25) is usually affected by the length of the CP as in the LTE 5 MHz scenario. The low-rate transform in this case cannot be smaller than 128 although  $L_r^{(k)}$  could be as small as a single PRB or two PRBs. As a result, this influences the parametrization of the FC-F-OFDM in (3.26). This limitation has been resolved in [YKLRP18] by re-arranging the overlapping periods in the transmitter and the receiver sides. Firstly, the overlapping factor is chosen in such way that low-rate OFDM is divided into integer number of FC blocks, i.e.,  $1/(1-\lambda)$  is an integer. Consequently, the CP could be appended in the overlapping region at every  $1/(1-\lambda)$  FC block if OLA is used in the transmitter. Therefore, it is possible to modify the CP length to be a divisor of  $N$ . The modified CP length should be less than targeted CP length. Accordingly, the high-rate overlapping period at every  $1/(1-\lambda)$  FC block considers the high-rate targeted CP in the overlapping period not the newly defined CP at the low rate. Accordingly, the overlapping period in the high-rate is defined as  $N_o/2 - N_{CP}$  samples.

Figure 3.11(a) shows an example of discontinuous FC-F-OFDM transmitter with  $\lambda = 0.5$ . Therefore, each low-rate CP-OFDM symbol is divided into two blocks while the first half contains the modified CP in the overlapping region. After the interpolation, the overlapping regions corresponding to CP are firstly shortened and shifted. The output high-rate has equivalent symbol length to CP-OFDM without considering the length of filter tails. On receiver side, the discontinuous FC-F-OFDM could be achieved by shifting the processed data according to CP with OLS processing. This can be achieved with same condition as  $1/(1-\lambda)$  is an integer.

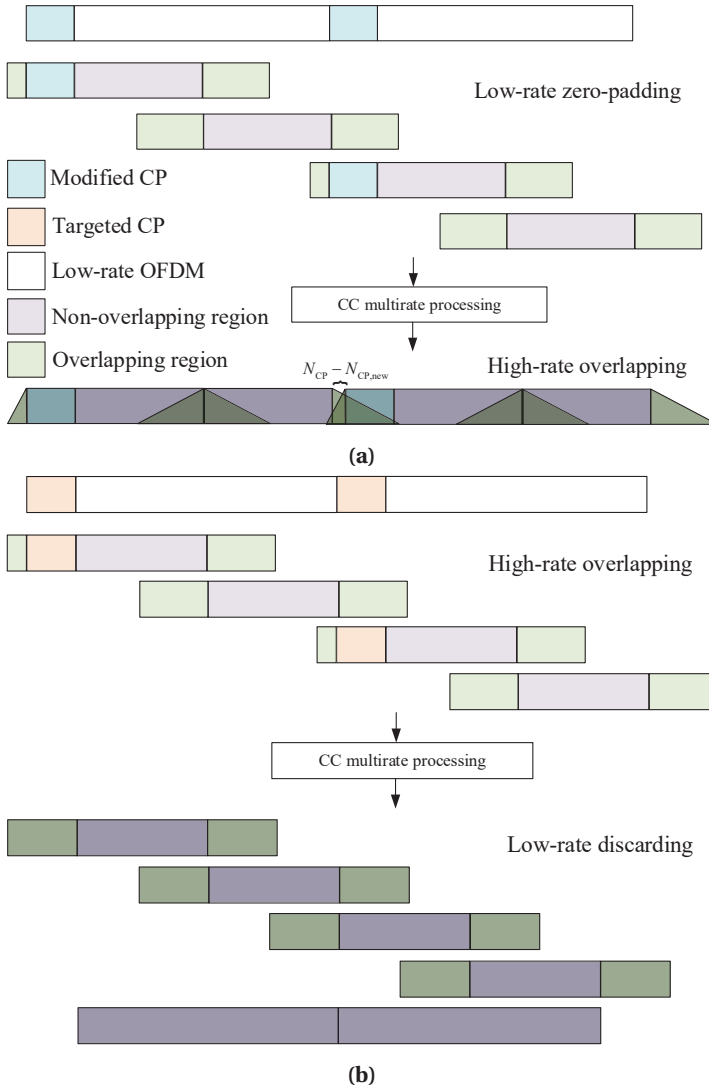


**Figure 3.11:** Symbol arrangements in low-rate and high-rate of the discontinuous FC-F-OFDM with  $\lambda = 0.5$  for (a) the transmitter and (b) the receiver. The CC multirate processing block consists of short transforms, frequency-masking, and long transform.

Figure 3.11(b) shows an example of discontinuous FC-F-OFDM receiver with  $\lambda = 0.5$ . The CP samples are not included in the non-overlapping part. As a result, the CP samples are contained in the overlapping period that is discarded directly at the low-rate side.

The main advantage of the discontinuous FC-F-OFDM scheme is the reduction in the computational complexity. Firstly, it is possible to reduce the sizes of the low-rate OFDM transform and the short transform sizes. Moreover, there is direct reduction on the number of FC blocks needed to process certain number of samples. Accordingly, there is significant reduction in the computational complexity rate.

### 3.3 Computational complexity analyses of multirate schemes

The computational complexity of PPN based FBMC with OQAM (FBMC/OQAM) is analyzed. Furthermore, FC schemes and RB-F-OFDM computational complexities are analyzed in this section. The assumptions of the computational complexity in Section 2.3 apply in this section such as the FFT/IFFT and complex multiplication implementations. Additionally, it is defined here the computational complexity formula for the complex multiplication of complex sequence of length  $N_l$  by twiddle factor  $W_N^{\pm k_o n}$  where  $n = [0, 1, \dots, N_l - 1]$ , which is defined as

$$\sigma_{TW}[N, N_l, k_o] = \begin{cases} 3N_l - \left\lceil \frac{8CN_l}{N} \right\rceil - 2 \left\lceil \frac{4CN_l}{N} \right\rceil, & \frac{N}{C} \notin \{1, 2, 4\} \\ 0, & \text{otherwise,} \end{cases} \quad (3.27)$$

where  $C = \gcd(N, k_o)$ . This formula returns the number of real multiplications which is equivalent to the number of real additions considering 3 real multiplications and 3 real additions for non-trivial multiplications, 2 real multiplications and 2 real additions for non-trivial 8th roots of unity and no arithmetic computations for trivial multiplications. The derivation of this formula is provided in Appendix A.2.

The implementation of the FBMC/OQAM consists of FFT/IFFT, the multiplication by the phase rotation for filter causality  $\beta_k$ , and polyphase filter. The normalization of the computational complexity is directly affected by the use of OQAM. Besides, the alternating real and imaginary inputs of OQAM allow the reduction of the IFFT by dividing IFFT of size  $N$  to two IFFTs of size  $N/2$  [BSRN11]. Generally, the transform implementation of the PPN is subjective to changes depending on the oversampling of the FBMC scheme. In this document, the computational complexity of FBMC/OQAM is represented as an reference for the PPN based implementations. Therefore, the computational complexity of critically sampled FBMC/OQAM is chosen for this purposes. Accordingly, the computational complexity of the FBMC/OQAM is expressed as [BSRN11]

$$\mu_{\text{FBMC}}[N, N_a, A_R] = \frac{2\langle A_R + 1 \rangle_2 \mu[N/2] + A_R (\mu[N] + 4N_a) + 2N_h N + 2N_a}{N_a/2} \quad (3.28a)$$

$$\alpha_{\text{FBMC}}[N, N_a, A_R] = \frac{2\langle A_R + 1 \rangle_2 \alpha[N/2] + A_R (\alpha[N] + 2N_a) + 2(N_h - 1)N}{N_a/2}, \quad (3.28b)$$

for real multiplication and real addition rates, respectively. Here, the computational complexity rates are multiplied by two due to the two times oversampling in OQAM implementations. Moreover, the single-tap equalization is assumed per subcarrier and real components for the polyphase filters. Furthermore, it is assumed that all of the multiplications by  $\beta_k$  are not trivial multiplications. For certain filter lengths, all of values of  $\beta_k$  can be trivial requiring no multiplications. Moreover,  $A_R$  is the receiver modifier that is defined in (2.13).

The computational complexity of the RB-F-OFDM is similar to the complexity of the F-OFDM that is discussed in Section 2.3. Each subband processing is calculated in similar way as in (2.15) with some modifications. Firstly, the complexity in RB-F-OFDM is cumulative over  $K$  subbands affecting also the normalization factor of the scheme. Therefore, the computational

complexity of the RB-F-OFDM is computed as

$$\mu_{\text{RF}}[N, A_R] = \sum_{\kappa=0}^{K-1} \left[ \mu_{\text{OFDM}}[L_O^{(\kappa)}, L_r^{(\kappa)}, A_R] + \frac{2n_a N_h^{(\kappa)} L_s^{(\kappa)} + \sigma_{\text{TW}}[N, N_f^{(\kappa)}, k_o^{(\kappa)}]}{n_a L_r^{(\kappa)}} \right] \quad (3.29a)$$

$$\alpha_{\text{RF}}[N, A_R] = \frac{2\langle A_R + 1 \rangle_2 (K-1) N_s}{\sum_{\kappa=0}^{K-1} L_r^{(\kappa)}} + \sum_{\kappa=0}^{K-1} \left[ \alpha_{\text{OFDM}}[L_O^{(\kappa)}, L_r^{(\kappa)}, A_R] + \frac{2n_a (N_h^{(\kappa)} - 1) L_s^{(\kappa)} + \sigma_{\text{TW}}[N, N_f^{(\kappa)}, k_o^{(\kappa)}]}{n_a L_r^{(\kappa)}} \right], \quad (3.29b)$$

for real multiplication and real addition rates, respectively. Here,  $n_a$  is the number of the processed RB-F-OFDM symbols, and  $N_f^{(\kappa)} = n_a N_s + N_h^{(\kappa)} - 1$  is the total number of transmitted or received samples. In this formula, the normalization factor is calculated based on the fact that each subband is processed independently. Hence, the computational complexity rate (real operation per sample) is computed independently on each subband and then added. Moreover, the OFDM transform and filtering are repeated  $K$  times acquiring intensive computational complexity in base-station cases. Moreover, the normalized computational complexity of the frequency modulation is applied for each subband on the serial samples. Therefore, their computational complexity rate is calculated over the full length of the transmitted signal  $N_f^{(\kappa)}$ .

The FC based FBMC and RB-F-OFDM consists basically of the multirate CC processing, OLA or OLS processing, and QAM, OQAM, or low-rate CP-OFDM processing. The CC multirate processing contains the long-transform part which is  $N$ -IFFT and  $N$ -FFT on the transmitter and the receiver sides, respectively. The long-transform part is usually the dominant complexity factor. The short-transforms part consists of  $K$  transforms each of size  $L^{(\kappa)}$ , the multiplication by the DFT components of the filter, and the multiplication by the phase continuity factor. The OLS process does not require any multiplications or additions. Nevertheless, the OLA process requires extra complex additions at the output of the multirate FC due to the overlapping. Finally, the used modulation affects directly the normalization factor of the multiplication rate. The OQAM and QAM requires oversampling the short transforms inputs by two. On the other hand, the low-rate CP-OFDM consists of low-rate transform. For generic formula, the real multiplication and real addition rates are expressed as

$$\mu_{\text{FC}}[N, A_R, A_{\text{OFDM}}] = \frac{\mu[N] + \mu_{\text{sh}}[A_R, A_{\text{OFDM}}]}{\eta_a[A_{\text{OFDM}}]} + A_{\text{OFDM}} \sum_{\kappa=0}^{K-1} \mu_{\text{OFDM}}[L_O^{(\kappa)}, A_R] \quad (3.30a)$$

$$\alpha_{\text{FC}}[N, A_R, A_{\text{OFDM}}] = \frac{\alpha[N] + \alpha_{\text{sh}}[A_R, A_{\text{OFDM}}]}{\eta_a[A_{\text{OFDM}}]} + A_{\text{OFDM}} \sum_{\kappa=0}^{K-1} \alpha_{\text{OFDM}}[L_O^{(\kappa)}, A_R], \quad (3.30b)$$

where,  $A_{\text{OFDM}}$  is OFDM modifier that is defined as

$$A_{\text{OFDM}} = \begin{cases} 1, & \text{for FC-F-OFDM} \\ 0, & \text{otherwise,} \end{cases} \quad (3.31)$$

and  $\eta_a$  is the normalization factor that returns the number of low-rate symbols processed per FC blocks that is expressed as follows:

$$\eta_a = \begin{cases} (1 - \lambda) \sum_{\kappa=0}^{K-1} \frac{L_r^{(\kappa)} L^{(\kappa)}}{L_s^{(\kappa)}}, & \text{for } A_{\text{OFDM}} = 1 \\ 0.5(1 - \lambda) \sum_{\kappa=0}^{K-1} L^{(\kappa)}, & \text{otherwise.} \end{cases} \quad (3.32)$$

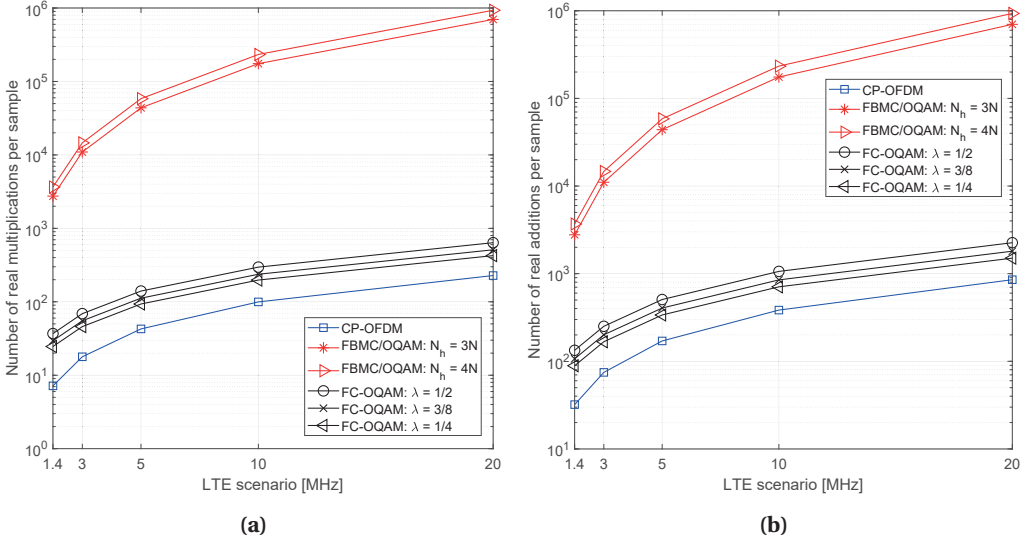


**Figure 3.12:** Computational complexity of FBMC/OQAM in polyphase implementation with  $N_h = \{3N, 4N\}$ , and FC-FB implementation with  $\lambda = \{1/2, 3/8, 1/4\}$  considering 72 active subcarriers in comparison to CP-OFDM. (a) Real multiplication rate. (b) Real addition rate.

In (3.30),  $\mu_{\text{sh}}[A_R, A_{\text{OFDM}}]$  and  $\mu_{\text{sh}}[A_R, A_{\text{OFDM}}]$  are the computational complexity of the short-transforms part that is calculated as

$$\mu_{\text{sh}}[A_R, A_{\text{OFDM}}] = \sum_{\kappa=0}^{K-1} \left[ \mu[L^{(\kappa)}] + 2L_H^{(\kappa)} + 4A_R \langle A_{\text{OFDM}} + 1 \rangle_2 L^{(\kappa)} \right] \quad (3.33a)$$

$$\alpha_{\text{sh}}[A_R, A_{\text{OFDM}}] = 2\theta \langle A_R + 1 \rangle_2 + \sum_{\kappa=0}^{K-1} \left[ \alpha[L^{(\kappa)}] + 2A_R \langle A_{\text{OFDM}} + 1 \rangle_2 L^{(\kappa)} \right], \quad (3.33b)$$

where  $\theta$  is the total number of overlapping DFT bins of two subbands with non-zero weights, and  $L_H^{(\kappa)}$  is the number of non-zero factors in the DFT-components of the filter. Regarding the discontinuous FC-F-OFDM, the computational complexity rate formula is not very different from (3.30). The reduced short transforms size could be substituted directly in short transform complexity formula (3.33). However, the discontinuity in the processing affects the normalization factor as follows:

$$\eta_{\text{ds}} = \frac{1}{(1-\lambda)} \sum_{\kappa=0}^{K-1} L_T^{(\kappa)}. \quad (3.34)$$

### 3.3.1 Numerical results in narrowband scenarios

Figure 3.12 shows the real multiplication and real addition rates for FBMC and FC-FB compared to CP-OFDM as reference in the transmitter. The computation rates of the receiver based FBMC/OQAM, FC-FB or CP-OFDM implementations differ in the equalization complexity. Besides, the receiver side of FBMC/OQAM has approximately  $N$  real multiplication more than the transmitter side. Therefore, the computational complexity of the transmitter side is sufficient for the comparison between different schemes. In this comparison, 72 active subcarriers are allocated in 1.4 MHz, 3 MHz, 5 MHz, 10 MHz and 20 MHz scenarios considering 128, 256, 512, 1024 and 2048 transform sizes, respectively. In FC-FB, the short transforms are chosen to be 16 implying that each subcarrier is upsampled by 16 as well. Therefore, long



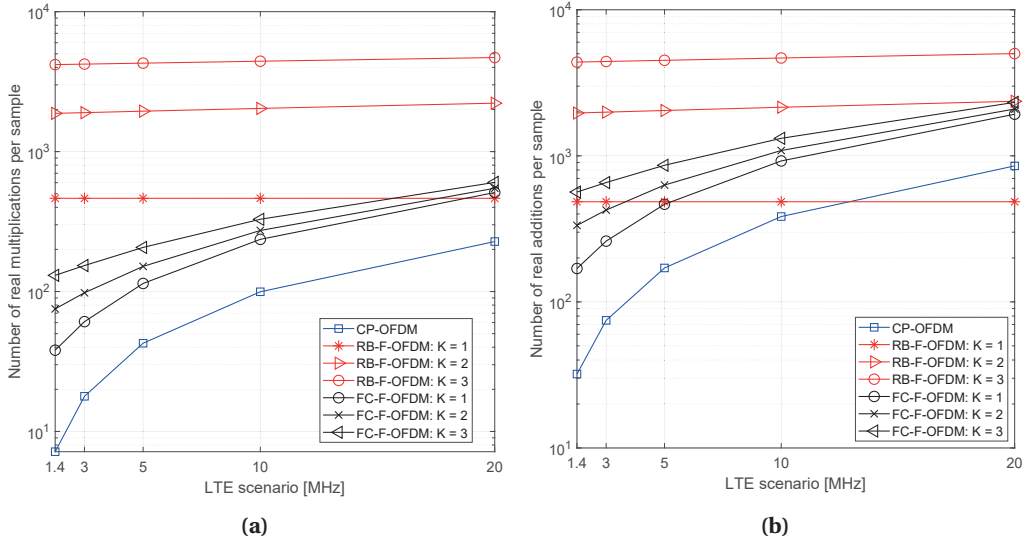


**Figure 3.13:** Computational complexity of RB-F-OFDM implementation with  $N_h = 120$  and FC-F-OFDM implementation with  $\lambda = 0.5$  and  $L = 128$  considering  $K = \{1, 2, 3\}$  subbands and 72 active subcarriers in comparison to CP-OFDM. (a) Real multiplication rate. (b) Real addition rate.

transforms are parameterized with the sizes 1024, 2048, 4096, 8192 and 16384 for 1.4 MHz, 3 MHz, 5 MHz, 10 MHz and 20 MHz LTE scenarios, respectively. Moreover, 72 short transforms are needed considering one short transform per subband. Each subband processes  $(1 - \lambda)16$  samples per subband resulting in  $1152(1 - \lambda)$  per FC block. Besides, it is assumed that the phase continuity factor between FC blocks is set to trivial values. The computational complexity of FBMC/OQAM is shown with two filter lengths of  $3N$  and  $4N$ . Clearly, FBMC/OQAM requires large number of real multiplications and real additions with respect to FC-FB and CP-OFDM. For FC-FB waveform, three alternatives of  $\lambda$  has been chosen to show differences in the computation rates. For example in Figure 3.12b(a), FC-FB requires 202 %, 141 %, and 101 % real multiplication per sample more than CP-OFDM for  $\lambda = 1/2, 3/8$  and  $1/4$  in 5 Hz LTE, respectively.

Secondly, the computational complexity rate of RB-F-OFDM and FC-F-OFDM is compared with 72 active subcarriers in LTE scenario as shown in Figure 3.13. The RB-F-OFDM and FC-F-OFDM waveforms are compared in 1, 2 and 3 active subbands cases. Accordingly, the 72 active subcarriers are divided to groups of 72, 36, and 24 active subcarriers for 1, 2 and 3 active subbands cases, respectively. Regarding the low-rate CP-OFDM configuration, the LTE scenarios of 1.4 MHz, 3 MHz, 5 MHz, 10 MHz, and 20 MHz require CP of lengths 9, 18, 36, 72 and 144 samples, respectively. Therefore, the minimum transform size of the low-rate OFDM is 128 according to (3.25) which is applicable on RB-F-OFDM and FC-F-OFDM. The filter length of RB-F-OFDM is 120 for all LTE scenarios. Regarding FC-F-OFDM, single, two and three short transforms all of size 128 are used for 1, 2 and 3 active subbands cases, respectively. The short transform size is calculated using (3.26) assuming  $N = 128, 256, 512, 1024$ , and 2048 for 1.4 MHz, 3 MHz, 5 MHz, 10 MHz, and 20 MHz scenarios, respectively. The frequency-masks are designed with 72, 36, and 24 DFT points as pass-band and 4 DFT points as transition band for single, two, and three subbands scenarios, respectively. The overlapping factor is 0.5 as it provides significant OOB emission reduction with acceptable computational complexity rates. Hence, each FC block processes approximately 33.6 samples. The computational complexity rate



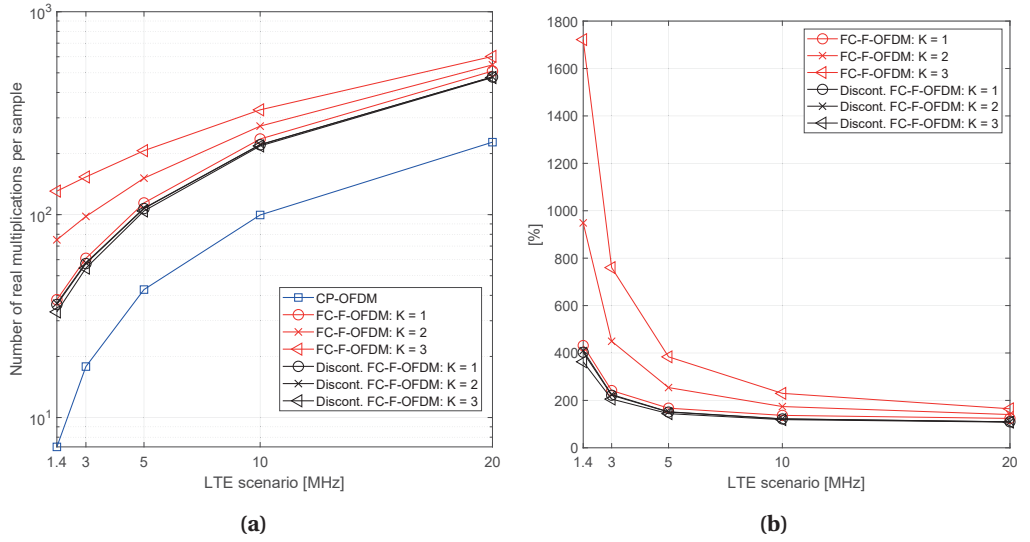


**Figure 3.14:** Computational complexity of FC-F-OFDM  $L = 128$  and discontinuous (discont.) FC-F-OFDM with  $L = \{128, 64, 32\}$  considering  $\lambda = 0.5$ ,  $K = \{1, 2, 3\}$  and 72 active subcarriers in comparison to CP-OFDM. (a) Real multiplication rate. (b) Relative increase in multiplication rate w.r.t. CP-OFDM in percentage.

of the RB-F-OFDM is almost constant with respect to the LTE scenario. Because the sources of the complexity is the low-rate OFDM transform and the filtering that are approximately constant in all LTE scenarios. It should be noted that the filtering is 98.5 %, 91.2 % and 94 % of the RB-F-OFDM multiplication rate with single, two and three subbands cases. Generally, the computational complexity rate of the RB-F-OFDM is higher than FC-F-OFDM and CP-OFDM. Regarding FC-F-OFDM, the computational complexity increases slightly with the increase of the number of the subband due to increase in the number of short transforms.

Figure 3.14 compares the real multiplication rates of FC-F-OFDM and discontinuous FC-F-OFDM with respect to CP-OFDM in LTE scenarios. The parameterization of FC-F-OFDM is equivalent to the configuration of the preceding example of Figure 3.13. Considering discontinuous FC-F-OFDM, the same parameterizations are assumed for long transform sizes, overlapping factor and number of subcarrier per subband. The discontinuous FC-F-OFDM implementation differs in the short transform size depending only on the number of active subcarriers per subband. Accordingly, the short transform sizes are 128, 64 and 32 for the single, two, and three subband cases, respectively. Moreover, the exclusion of the CP from the processing increases the normalization factor to 36, according to (3.34), reducing the real multiplication rate of the discontinuous FC-F-OFDM. The real multiplication rate in Figure 3.14(a) shows that the real multiplication rate of all discontinuous FC-F-OFDM cases are smaller than FC-F-OFDM. Moreover, the discontinuous FC-F-OFDM requires approximately 150 % real multiplications more than CP-OFDM in 5 MHz LTE scenario as shown in Figure 3.14(b). This percentage increases up to 167 %, 254 % and 384 % for FC-F-OFDM in single, two and three subbands, respectively. This shows clear advantage of discontinuous FC-F-OFDM processing in terms of computational complexity with respect to direct FC-F-OFDM processing.

### 3.4 Chapter summary

The use of FBMC delivers highly localized subbands in frequency domain by using per sub-carrier filtering. The chosen example in Figure 3.3 shows significant reduction in the OOB emissions. Nevertheless, in narrowband scenarios traditional polyphase filter bank based FBMC/OQAM requires up to 200-fold multiplication rate with respect to CP-OFDM, as shown in Figure 3.12. This extreme difference in the complexity introduces practical difficulties in implementing the FBMC scheme. FC-FB scheme moves the filtering to the frequency domain by employing FC processing. FC-FB permits a controlled amount of CC interference by adjusting the overlapping factor  $\lambda$ . Also this scheme shows significant reduction in the OOB emissions as shown in Figure 3.8. This is accompanied by reduced computational complexity with respect to polyphase FBMC as shown in Figure 3.12. Nevertheless, FBMC based implementations are not well localized in time domain preventing the use of CP. Consequently, they require more complicated processing to cope with multipath effects and they have essential limitations in certain multi-antenna transmission schemes. 5G-NR adopted another approach, subband-wise OFDM signal generation with filtering or windowing, which has high degree of commonality with previous OFDM systems. RB-F-OFDM uses either dedicated time-domain low-pass filters or uniform polyphase filter banks for this purpose. RB-F-OFDM using separate low-pass subband filters maintains a considerable flexibility by introducing frequency modulator for translating the filtered signal around the desired center frequency. The FC version of this scheme is FC-F-OFDM that moves the filtering from time domain to frequency domain. The complexity calculations show clear advantage of FC-F-OFDM with respect to RB-F-OFDM, as shown in Figure 3.13. The discontinuous implementation of FC-F-OFDM requires even fewer operations. Generally, the computational complexity of the FC based schemes can reach 2 to 5 times the complexity of CP-OFDM.

## Low-Complexity Multicarrier Schemes using Decomposed FC Processing

The advanced multicarrier schemes introduced above provide mainly improved spectral characteristics for the communication system to comply with the demands of the future wireless networks. However, they exhibit significantly increased computational complexity. We have seen in Section 3.3 that FC based schemes provide greatly reduced computational complexity with respect to time-domain filtering schemes. Nevertheless, the computational complexity rates of the FC-FB and FC-F-OFDM are about two times higher than those of CP-OFDM. In this chapter, we consider possibilities to relax the computational complexity of those schemes further by using the decomposition of the multirate CC. First, a generic multirate FC implementation is proposed based on the multirate CC decomposition without any loss in the spectral localization or system performance. This implementation is denoted as decomposed FC-FB (D-FC-FB). D-FC-FB implementation maintains the benefits of the direct FC based waveforms, such as flexible bandwidth allocation with adjustable center frequencies, with slight increase in the computational complexity. When adjusted to certain special scenarios, the decomposed approach brings significant reduction in the computational complexity. One beneficial use-case of the D-FC schemes is in narrowband scenarios in which the number of active subbands is relatively small. Such scenario occurs usually at the UE side where narrowband communication is often sufficient. Especially in mMTC, this is the situation always. Another interesting scenario is uniformly distributed non-overlapping subbands. Such schemes can be exploited for FMT-type multicarrier waveforms. Furthermore, the multirate CC decomposition can be exploited in FC-F-OFDM receivers applying the idea of symbol-synchronized discontinuous FC processing [YKLRP18]. In all these investigated scenarios, D-FC achieves significant reduction in the computational complexity compared to the corresponding implementations using direct FC processing.

In [NNB18], computationally efficient implementation for UFMC was proposed using the decomposition of linear time-domain filtering. Nevertheless, this scheme requires some modifications to the 3GPP LTE specifications and it is limited to the transmitter side. The use of the CC decomposition was proposed in [LYR17] for narrowband FC-FB based transmitters. The generic framework of the FC decomposition considering both transmitter and receiver sides was introduced in [LYR19], including specific schemes for narrowband transmission and uniformly distributed subbands scenarios.

This chapter introduces the implementation aspects of the D-FC schemes based on [LYR19], considering also the special D-FC structures for the narrowband and uniformly distributed

subband cases. Moreover, the application of the decomposition in the symbol synchronized discontinuous FC-F-OFDM implementations is proposed.

### 4.1 The decomposition of circular convolution

The CC process was discussed in Subsection 3.1.1 and it can be expressed mathematically as

$$y_l[n] = \frac{1}{N} \sum_{k=0}^{N-1} X_l[k] H[k] W_N^{-nk}, \quad (4.1)$$

where  $N$  is the length of the CC processing block which is also the length of DFT and IDFT blocks,  $X_l[k]$  is the DFT of the  $l$ th input block  $x_l[n]$  and  $H[k]$  is the DFT of the filter impulse response  $h[n]$ .

The decomposition of the CC is based on the "multi-dimensional cyclic convolution" in [Bla10]. The decomposition of CC re-indexes the input sequence and the filter impulse response in such way that the CC blocks are processed in smaller decimated chunks of samples. The input block and filter impulse response are divided in time-domain using the polyphase model. Accordingly, DFT of size  $N/D$  is applied on the decimated and delayed input sequence and filter response as

$$X_l[k', d_x] = \sum_{r=0}^{\frac{N}{D}-1} x_l[rD + d_x] W_{\frac{N}{D}}^{rk'} \quad (4.2a)$$

$$H[k', d_h] = \sum_{r=0}^{\frac{N}{D}-1} h[rD + d_h] W_{\frac{N}{D}}^{rk'}, \quad (4.2b)$$

where  $d_x = 0, 1, \dots, D-1$  is the delay index of the input,  $d_h = 0, 1, \dots, D-1$  is the delay index of the filter,  $r$  is the decimated time index, and  $k' = 0, 1, \dots, N/D-1$  is the frequency index for the DFT output of size  $N/D$ . Hence, the DFT responses of input sequence and the filter response for the reduced size DFT are expressed as follows:

$$X_l[k] = \sum_{d_x=0}^{D-1} X_l\left[\langle k \rangle_{\frac{N}{D}}, d_x\right] W_N^{d_x k} \quad (4.3a)$$

$$H[k] = \sum_{d_h=0}^{D-1} H\left[\langle k \rangle_{\frac{N}{D}}, d_h\right] W_N^{d_h k}. \quad (4.3b)$$

Accordingly, the CC process can be evaluated by substituting (4.3) in (4.1) as

$$y_l[n] = \frac{1}{N} \sum_{k=0}^{N-1} \sum_{d_h=0}^{D-1} \sum_{d_x=0}^{D-1} Y_l[k, d_x, d_h] W_N^{(d_x+d_h)k} W_N^{-nk}, \quad (4.4)$$

where  $Y_l[k, d_x, d_h] = X_l\left[\langle k \rangle_{\frac{N}{D}}, d_x\right] H\left[\langle k \rangle_{\frac{N}{D}}, d_h\right]$  is a periodic function with period of  $N/D$  samples. Then the output IDFT transform of size  $N$  is decimated at the output. The decimation of DFT output is commonly known as decimation-in-frequency [Mur94, SP99]. Here, IDFT is used assuming time-domain indexes at the output. Accordingly, the same concept is used by splitting the input of the IDFT of size  $N$  to  $D$  contiguous parts and decimating the output. Accordingly, the time index of the IDFT output is remapped to  $n = Dr + d_y$ , where  $d_y = 0, 1, \dots, D-1$  is the delay index of the output. The input of the IDFT is also partitioned as  $k = k' + d_p N/D$ ,

where  $d_p = 0, 1, \dots, D-1$  is the index of the input parts. Therefore, the polyphased output can be expressed as follows:

$$y_l[Dr + d_y] = \frac{1}{N} \sum_{d_h=0}^{D-1} \sum_{d_x=0}^{D-1} \left[ \sum_{d_p=0}^{D-1} W_D^{(d_x+d_h-d_y)d_p} \right] \left[ \sum_{k'=0}^{\frac{N}{D}-1} Y_l[k', d_x, d_h] W_N^{(d_x+d_h-d_y)k'} W_{\frac{N}{D}}^{-rk'} \right]. \quad (4.5)$$

This formula can be simplified by considering sums of complex exponentials over  $d_p$  as

$$\sum_{d_p=0}^{D-1} W_D^{(d_x+d_h-d_y)d_p} = \begin{cases} D, & \text{for } d_x + d_h - d_y = a_{CC}D \\ 0, & \text{otherwise,} \end{cases} \quad (4.6)$$

where  $a_{CC}$  is an integer. The equality can be solved as follows:

$$\begin{aligned} d_h + d_x &= a_{CC}D + d_y & d_y - d_h &= d_x - a_{CC}D \\ \langle d_h + d_x \rangle_D &= \langle a_{CC}D + d_y \rangle_D & \text{or,} & \langle d_y - d_h \rangle_D = \langle d_x - a_{CC}D \rangle_D, \\ \langle d_h + d_x \rangle_D &= d_y & & \langle d_y - d_h \rangle_D = d_x. \end{aligned} \quad (4.7)$$

The value of  $a_{CC}$  can take one of the following choices:

$$\begin{aligned} \left\lfloor \frac{d_h + d_x}{D} \right\rfloor &= \left\lfloor a_{CC} + \frac{d_y}{D} \right\rfloor & \text{or,} & \left\lfloor \frac{d_h - d_y}{D} \right\rfloor = \left\lfloor a_{CC} - \frac{d_x}{D} \right\rfloor, \\ \left\lfloor \frac{d_h + d_x}{D} \right\rfloor &= a_{CC} & & \left\lfloor \frac{d_h - d_y}{D} \right\rfloor = a_{CC} \end{aligned} \quad (4.8)$$

Accordingly, the polyphase output can be calculated as follows:

$$y_l[Dr + d_y] = \frac{D}{N} \sum_{d_h=0}^{D-1} \sum_{k'=0}^{\frac{N}{D}-1} Y_l[k', \langle d_y - d_h \rangle_D, d_h] W_{\frac{N}{D}}^{a_{CC}k'} W_{\frac{N}{D}}^{-rk'}. \quad (4.9)$$

Therefore, the output transform can be replaced by  $D$  transforms of size  $N/D$ .

Figure 4.1 shows three examples of the decomposition of CC with  $D = 2$ . Figure 4.1(a) represents the generic case of CC with  $D = 2$ . The input signal is decimated by two and delayed, in such way that the odd and even halves of the sequence are inputs of two separate DFTs of size  $N/2$ , according to (4.3a). Then, each branch is multiplied by the stored decomposed filter coefficients  $H[k', d_h]$  that are calculated according to (4.3b). Then, the result of the multiplication is multiplied by the required twiddle factors, added, and finally fed to IDFT of size  $N/2$  as in (4.9). Finally, CC output is obtained by upsampling and delaying the resulting sequences from the two branches. Figure 4.1(b) is an example of the CC decomposition with upsampled input. In this case, half of the input sequence is zero-valued. Therefore, the lower branch of the input can be removed along with the corresponding processes. Therefore, three transforms of size  $N/2$  are needed compared to two transforms of size  $N$  in the direct CC implementation as depicted in Figure 3.6(c). Figure 4.1(c) shows an example of decomposed CC with decimated output and  $D = 2$ . Accordingly, half of the output samples are not needed and the corresponding operations can be ignored. This shows also reduction in the transform sizes compared to the direct implementation of CC. These multirate CC examples are a good indication of the possible reduction in the computational complexity of the FC based multirate implementation since CC is the core computation module in the FC processing.

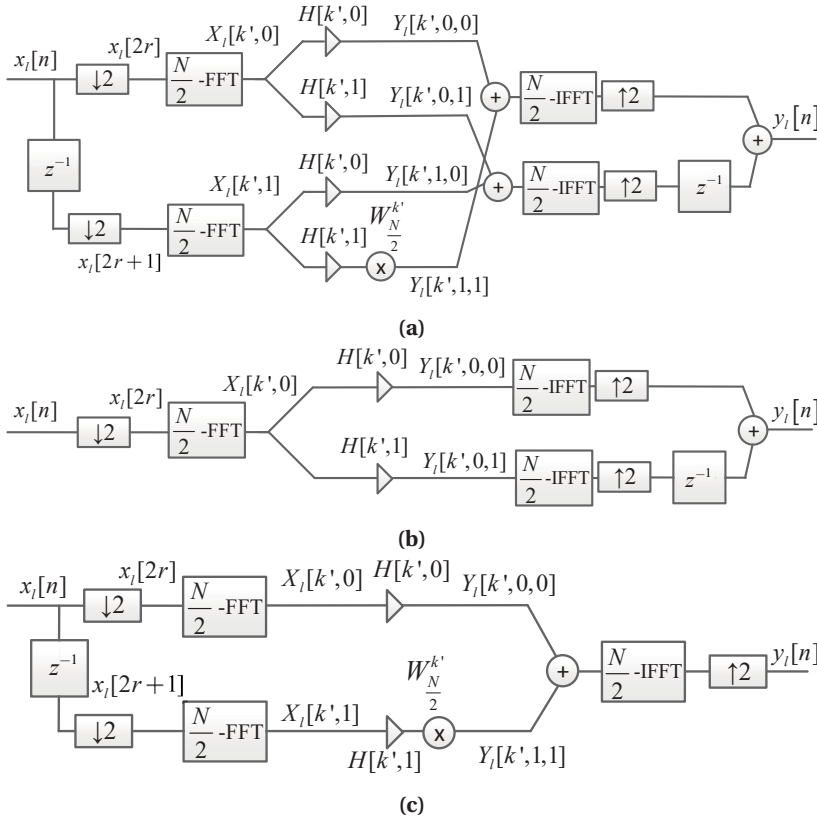


**Figure 4.1:** The implementation of decomposed CC (a) without multirate processing, (b) with upsampled input, and (b) with decimated output. Single-rate models are used in (b) and (c) to highlight their connection with (a). Each line connecting the blocks represents  $N/2$  input/output samples, except for  $x_l[n]$  and  $y_l[n]$  which represent  $N$  input/output samples.

## 4.2 The decomposition of the multirate CC

The use of multirate CC decomposition in FC processing leads to various decomposed FC schemes. However, some of those variants are not beneficial as they are not computationally efficient or limit the flexibility of the FC processing. In the following subsection, the generic D-FC based scheme is formulated. Then the computationally efficient variants are proposed in the later subsections.

### 4.2.1 Generic decomposition scheme for multirate FC based schemes

For efficient use of CC decomposition, the decomposition factor  $D$  should be chosen such that the low-rate inputs or outputs require a single branch of processing, as shown in Figures 4.1(b) and (c). The decomposition factor  $D$  specifies the decimation or upsampling factor at the input or the output of the decomposed CC. Moreover, FC schemes interpolate or decimate each subband by  $R^{(k)}$ . Therefore, the chosen decomposition factor should satisfy

$$D \leq R_{\min}, \quad (4.10)$$

where  $R_{\min}$  is the minimum interpolation/decimation factor in  $K$  subbands.

In the transmitter side, the low-rate input of the multirate FC is overlapped or zero-padded as (3.6). Then, the input of the multirate CC process  $c_l[s, \kappa]$  is interpolated by the factor  $R^{(\kappa)}$ . Accordingly, the decimation of the oversampled  $c_l[s, \kappa]$  by  $D$  results in  $c_l[s, \kappa, d_x] = 0$  for all values of  $d_x \neq 0$ . For  $d_x = 0$ , the low-rate input is equivalent to the decomposed input, i.e.,  $c_l[s, \kappa, 0] = c_l[s, \kappa]$ . According to (4.2a), the short transform output considering the decomposition is updated as follows:

$$C_l[k', \kappa, d_x] = \begin{cases} C_l[k', \kappa], & \text{for } d_x = 0 \\ 0, & \text{for } d_x = 1, 2, \dots, D-1. \end{cases} \quad (4.11)$$

Consequently, the filter is needed to be decomposed as in (4.2b). The FC processing requires DFT domain coefficients for the filter. Generally, the DFT response of the filter is defined as

$$H_s[k, \kappa] = P[\langle k - k_o^{(\kappa)} \rangle_N, \kappa] W_N^{-\tau^{(\kappa)} k}, \quad (4.12)$$

where  $\tau^{(\kappa)}$  is the delay term and  $P[k, \kappa]$  is the zero-phase DFT response of the filter. The zero-phase DFT response should be defined to contain non-zero real coefficient in the period  $[-L^{(\kappa)}/2, L^{(\kappa)}/2 - 1]$ . To obtain the decomposed filter components according to (4.3b), the frequency-mask coefficients should be obtained in time-domain, downsampled, and then transformed by applying the reduced size DFT. This can be summarized as follows:

$$H_s[k', \kappa, d_h] = \frac{1}{N} W_N^{-k_o^{(\kappa)}(d_h + \tau^{(\kappa)})} \sum_{k=0}^{N-1} P[\langle k \rangle_N, \kappa] W_N^{-k(d_h + \tau^{(\kappa)})} \sum_{r=0}^{\frac{N}{D}-1} W_{\frac{N}{D}}^{r(k' - k - k_o^{(\kappa)})}. \quad (4.13)$$

To simplify the mathematical analyses, the subband index  $\kappa$  should be re-indexed based on the center frequency of the subband  $k_o^{(\kappa)}$ . Accordingly, the center frequencies are remapped as

$$k_o^{(\kappa)} - \frac{L^{(\kappa)}}{2} = \Delta \frac{N}{D} + k'_o, \quad (4.14)$$

where  $\Delta$  and  $k'_o$  are defined as

$$\Delta = \left\lfloor \frac{k_o^{(\kappa)} - L^{(\kappa)}/2}{N/D} \right\rfloor \quad (4.15a)$$

$$k'_o = \left\langle k_o^{(\kappa)} - \frac{L^{(\kappa)}}{2} \right\rangle_{\frac{N}{D}}, \quad (4.15b)$$

respectively. Accordingly, the sum of exponentials in (4.13) can be solved as

$$\sum_{r=0}^{\frac{N}{D}-1} W_{\frac{N}{D}}^{r(k' - k - \Delta \frac{N}{D} - \frac{L^{(\Delta, k'_o)}}{2} - k'_o)} = \begin{cases} \frac{N}{D} & \text{for } k' - k - \Delta \frac{N}{D} - \frac{L^{(\Delta, k'_o)}}{2} - k'_o = a_H \frac{N}{D} \\ 0, & \text{otherwise,} \end{cases} \quad (4.16)$$

where  $a_H$  is an integer. Here, the interval of  $k$  is redefined considering the interval of  $P[\langle k \rangle_N, \kappa]$  as  $k + L^{(k'_o, \Delta)}/2 \in \{0, 1, \dots, L^{(k'_o, \Delta)} - 1\}$ . Considering the intervals of  $k'$  and  $k'_o$ , the value of  $a_H$  is a negative integer that is calculated as

$$a_H = -(\Delta + A[k', k'_o]), \quad (4.17)$$

where  $A[k', k'_o]$  is a conditional function that is defined as follows:

$$A[k', k'_o] = \begin{cases} 0, & \text{for } k' \geq k'_o \\ 1, & \text{for } k' < k'_o. \end{cases} \quad (4.18)$$

Consequently, the decimated and delayed branch of the filter can be expressed as

$$H_s[k', \Delta, k'_0, d_h] = \frac{1}{D} W_N^{-d_h k'} W_D^{-d_h(\Delta + A[k', k'_0])} G[k', \Delta, k'_0], \quad (4.19)$$

where  $G[k', \Delta, k'_0]$  is the DFT response of the decomposed filter without the decomposition twiddle factors that is defined as follows:

$$G[k', \Delta, k'_0] = W_N^{-\tau^{(\Delta, k'_0)}(k' + \frac{N}{D}(\Delta + A[k', k'_0]))} P \left[ \left\langle k' - k'_0 - \frac{L(\Delta, k'_0)}{2} + \frac{N}{D} A[k', k'_0] \right\rangle_N, \Delta, k'_0 \right]. \quad (4.20)$$

Here, the effect of  $A[k', k'_0]$  is the added frequency shift and phase shift. These shifts are needed due to division of the DFT points of length  $N$  to spectral sections of length  $N/D$  bins. Hence, the intersection of the non-zero components of  $H_s[k, \kappa]$  with two spectral section results in adding frequency shifts to  $G[k', \Delta, k'_0]$  and phase shift to  $H[k', \Delta, k'_0, d_h]$ . This only happens when  $k'_0 > k'$ . On the other hand, there is no added shifts when the non-zero components of  $H_s[k, \kappa]$  intersecting with  $N/D$  spectral sections due to  $k'_0 \leq k'$ . Therefore, the components of  $G[k', \Delta, k'_0]$  is equivalent to  $H_s[k, \kappa]$  but circularly shifted around  $N/D$  DFT points.

The final step involves the decomposition of the multirate CC output  $y_l[n]$  in (3.11) according to (4.9) considering (4.7). It has been concluded in (4.11) that only  $d_x = 0$  case has a non-zero value. Accordingly, (4.7) is updated as follows:

$$d \equiv d_y = \langle d_h \rangle_D. \quad (4.21)$$

As a consequence,  $a_{CC}$  equals zeros as in (4.8). Therefore, the polyphased output of the multirate is expressed as

$$y_l[r, d] = \frac{D}{N} \sum_{k'=0}^{\frac{N}{D}-1} Y_l[k', d] W_N^{-r k'}, \quad (4.22)$$

where  $Y_l[k', d]$  is the sum of filtered subbands as follows:

$$Y_l[k', d] = \frac{1}{D} W_N^{-k' d} \sum_{\substack{\Delta=0 \\ k'_0 \in K_0}}^{D-1} Y_l[k', \Delta, k'_0] W_D^{-(\Delta + A[k', k'_0])d}. \quad (4.23)$$

Here,  $K_0 \in \{0, 1, \dots, N/D - 1\}$  and  $Y_l[k', \Delta, k'_0]$  equals the rotated filter  $G[k', \Delta, k'_0]$  and the short transform output  $C_l[k', \Delta, k'_0, 0]$  as follows:

$$Y_l[k', \Delta, k'_0] = G[k', \Delta, k'_0] C_l \left[ \left\langle k' - k'_0 \right\rangle_{\frac{N}{D}}, \Delta, k'_0, 0 \right]. \quad (4.24)$$

In (4.23), the sum of complex exponentials over  $\Delta$  represents an IDFT process of size  $D$ . The IDFT of size  $D$  is needed at least  $N/D$  times because it is defined with respect to  $k'$ . Moreover,  $D$  transforms of size  $N/D$  are needed because the transforms in (4.22) is defined with respect to  $d = 0, 1, \dots, D-1$ . The inputs of the  $k'$ th IDFT of size  $D$  are allocated from the decimated frequency points  $[k', k' + N/D, \dots, k' + (D-1)N/D]$ . The effect of  $A[k', k'_0]$  is neglected when  $k' \geq k'_0$ . However,  $A[k', k'_0]$  shifts the input of the  $k'$ th transform of size  $D$  from  $\Delta$  to  $\Delta + 1$ . Therefore, no complex multiplications are needed. Finally, the  $d$ th output of the  $k'$ th transform of size  $D$  is fed to  $k'$ th input of the  $d$ th transforms of size  $N/D$ . Figure 4.2(a) shows D-FC-FB implementation on the transmitter side. The subbands have equal bandwidths and they are not overlapping to simplify the illustration. Furthermore, the figure shows only the decomposed multirate CC part. Other combinations of overlapping subbands, different bandwidths, and/or center frequencies are also possible with D-FC-FB.



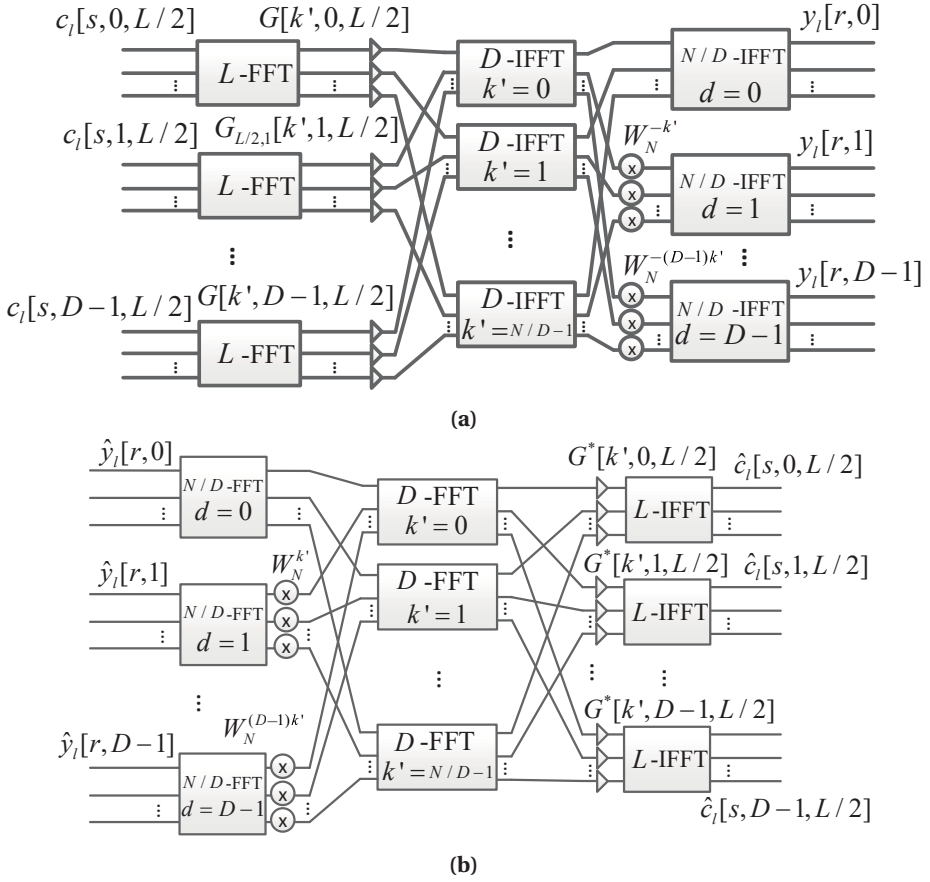


**Figure 4.2:** The structure of the decomposed CC-part of D-FC-FB. (a) SFB/transmitter. (b) AFB/receiver. The subbands are assumed to have equal sizes of  $L$  and centered at  $L/2$  with respect to  $k'$ . Arbitrary subband sizes and center frequencies are possible with D-FC-FB.

Similar analyses apply for the receiver side. The condition in (4.10) applies for restricting the decomposition factor  $D$ . The definition on the receiver filter is the conjugation of the filter of the transmitter side as follows:

$$H_a[k, \kappa] = P[\langle k - k_o^{(\kappa)} \rangle_N, \kappa] W_N^{\tau^{(\kappa)} k}. \quad (4.25)$$

Hence, the decomposition of the receiver filter is expressed as

$$H_a[k', \Delta, k'_o, d_h] = \frac{1}{D} W_N^{-d_h k'} W_D^{-d_h(\Delta + A[k', k'_o])} G^*[k', \Delta, k'_o], \quad (4.26)$$

using the subband indexing concept of (4.14) and (4.15). Here,  $G[k', \Delta, k'_o]$  is defined in (4.20). The input of the multirate CC  $\hat{y}_l[n]$  in (3.13) is firstly decomposed as in (4.3a) defining  $\hat{Y}_l[k', d_y]$ . Considering the decimation of the multirate CC output, the decomposed low-rate output is defined as:

$$\hat{c}_l[k', \Delta, k'_o, 0] = \begin{cases} \hat{c}_l[k', \Delta, k'_o], & \text{for } \hat{d}_x = 0 \\ 0, & \text{for } \hat{d}_x = 1, 2, \dots, D-1. \end{cases} \quad (4.27)$$

Accordingly, the relation between delay indexes in (4.7) can be updated as follows:

$$\langle -\hat{d} \rangle_D \equiv \hat{d}_y = \langle -\hat{d}_h \rangle_D. \quad (4.28)$$

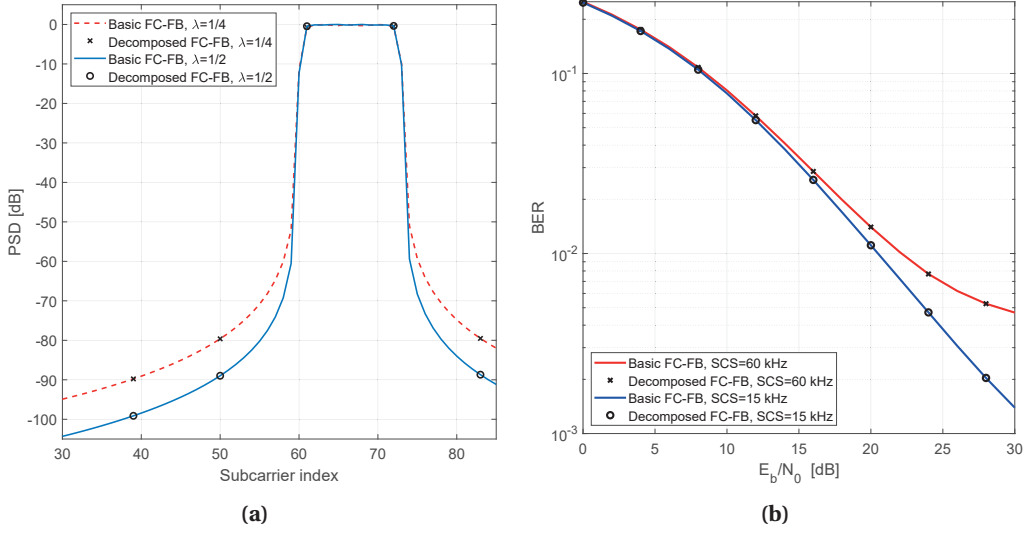


**Figure 4.3:** (a) PSDs of D-FC-FB and FC-FB with  $L = 16$  and overlap factor  $\lambda \in \{1/2, 1/4\}$ . The PSDs are integrated over the subcarrier spacing of 15 kHz, while using 12 active subcarriers out of 2048 in total. (b) BER performance of D-FC-FB and FC-FB with  $\lambda = 3/8$  in TDL-C channel with 1  $\mu$ s RMS channel delay considering 15 kHz and 60 kHz subcarrier spacings (SCS).

Then, the decomposed output is calculated as

$$\hat{c}_l[Dr] = \frac{D}{N} \sum_{k'=0}^{\frac{N}{D}-1} \hat{C}_l \left[ \langle k' + k'_0 \rangle_{\frac{N}{D}}, \Delta, k'_0 \right] W_{\frac{N}{D}}^{-k'r}, \quad (4.29)$$

where  $\hat{C}_l[k', \Delta, k'_0]$  is the input of the short transform that is defined as

$$\hat{C}_l[k', \Delta, k'_0] = \frac{1}{D} G^* [k', \Delta, k'_0] \sum_{\substack{\hat{d}=0 \\ k'_0 \in K_0}}^{D-1} \hat{Y}_l[k', \hat{d}] W_N^{\hat{d}k'} W_D^{\hat{d}(\Delta + A[k', k'_0])}, \quad (4.30)$$

Here,  $\langle -\hat{d} \rangle_D$  is redefined as  $D - \hat{d}$ . This helps to change the negative sign of the twiddle factors in (4.26) to positive. As a result, the implementation of the D-FC-FB on the receiver side is a dual case of the transmitter side as shown in Figure 4.2(b).

The mathematical analyses of the D-FC-FB scheme shows that the output of the D-FC-FB is equivalent to the corresponding FC-FB scheme (while not considering the effects of wordlength implementations). Figure 4.3 shows the PSD and BER of the decomposed implementation to the generic FC-FB with  $N = 2048$ ,  $L = 16$ , and  $K = 1$ . Figure 4.3(a) shows the PSDs of D-FC-FB compared to FC-FB with different overlapping factors. Clearly, the PSD of D-FC-FB is equivalent to the PSD of the FC-FB concluding the equality of both schemes on the transmitter side. Figure 4.3(b) shows that BER performance of the D-FC-FB is identical to that of FC-FB with different subcarrier spacings, indicating the equality of both schemes on the receiver side. Furthermore, the long transform is the only affected part of the CC by the decomposition. Accordingly, D-FC implementations inherit the flexibility in controlling the subbands bandwidths and center frequencies. Moreover, it does not affect the frequency-mask design or channel equalization processes.

#### 4.2.1.1 D-FC-FB with Cooley-Tukey algorithm

An equivalent implementation of the multirate FC scheme can be obtained using the Cooley-Tukey algorithm [CT65]. This is achieved by decomposing the long transforms using Cooley-Tukey algorithm. Then, all of the resulted transforms are implemented using split-radix FFT [SBJ88, SB93].

On transmitter side, the decomposition of the long transform requires the re-indexing of the frequency bins as

$$k = \Delta \frac{N}{D} + k', \quad (4.31)$$

where  $\Delta = \lfloor Dk/N \rfloor$  and  $k' = \langle k \rangle_{\frac{N}{D}}$ . Moreover, the time index is re-indexed as

$$n = rD + d, \quad (4.32)$$

where  $r = \lfloor n/D \rfloor$  and  $d = \langle n \rangle_D$ . Accordingly, the output of the decomposed long transform is expressed as

$$y_l[rD + d] = \frac{1}{N} \sum_{k'=0}^{\frac{N}{D}-1} W_N^{-dk'} W_{\frac{N}{D}}^{-rk'} \sum_{\Delta=0}^{D-1} Y_l \left[ k' + \frac{N}{D} \Delta \right] W_D^{-d\Delta}, \quad (4.33)$$

where  $Y^{(l)}[k]$  is defined as follows:

$$Y_l[k] = \sum_{\kappa=0}^{K-1} H_s[k, \kappa] X_l[\langle k - k_o^{(\kappa)} \rangle_N, \kappa]. \quad (4.34)$$

It can be concluded by comparing (4.33) with (4.22) and (4.23) that using CC decomposition or Cooley-Tukey algorithms results into equivalent approach. Cooley-Tukey algorithm can be applied on the receiver side in similar way resulting in equivalent implementation of (4.29). This statement holds if (4.10) is maintained with the CC decomposition and the filter. Besides, the DFT response of the filter should zero at the period  $\lfloor L_b/2, N - L_b/2 - 1 \rfloor$ .

Cooley-Tukey algorithm targets at decomposing the transform only. The decomposition of the long transform can be done regardless the interpolation/decimation ratio or the filter parameterization. Therefore, the idea can be straightforwardly exploited in pruning the DFT/IDFT transforms. The decomposition of multirate CC tackles the whole CC part, including the short transform, frequency-mask and long transform. Therefore, the decomposed CC is more generic in such as way that it can be used with any multirate filtering process.

#### 4.2.2 The decomposition of multirate CC in narrowband scenarios

In this subsection, the D-FC-FB scheme is applied in narrowband scenarios, resulting in significant reduction of the computational complexity. Here, a narrowband scenario is a case where the number of active DFT bins is relatively small in order to be able to prune all the transforms of size  $D$ . Each of those transforms should have a single input or output for transmitter and receiver sides, respectively. Therefore, those transform can be replaced by a set of twiddle factors  $W_D^{-d\delta}$  and  $W_D^{d\delta}$  for transmitter and receiver sides, respectively, where  $\delta \in \{0, 1, \dots, D-1\}$  is the subband index with respect to the  $N/D$  spectral sections. These twiddle factors can be combined with  $W_N^{-dk'}$  and  $W_N^{dk'}$  resulting in  $W_N^{-d(k' + \frac{N}{D}\delta)}$  and  $W_N^{d(k' + \frac{N}{D}\delta)}$  for transmitter and receiver sides, respectively. This variant of the decomposition is denoted as narrowband D-FC-FB (NB-FC-FB) and it is illustrated in Figure 4.4 for transmitter and receiver sides.

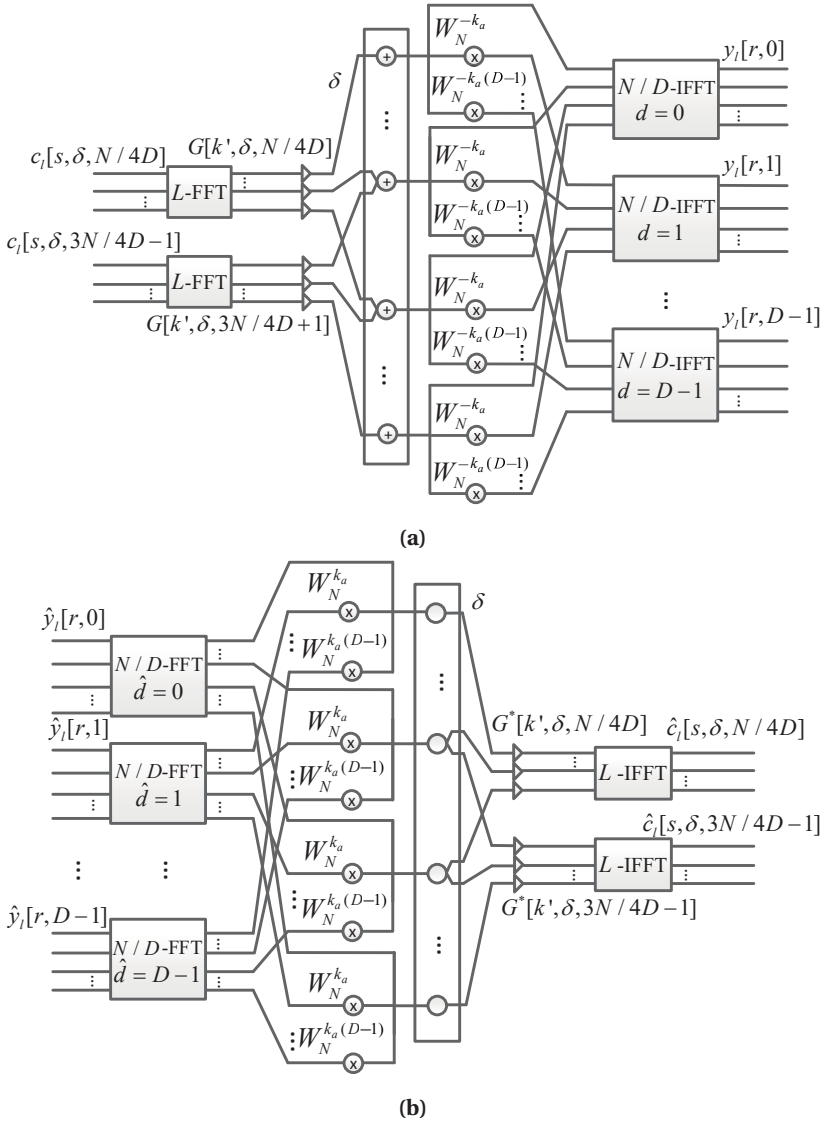


**Figure 4.4:** The implementation of NB-FC-FB in (a) SFB/transmitter, and (b) AFB/receiver, for two active subbands of width  $L = N/2D + 1$ . The two subbands are allocated in the  $\delta$ th section of the spectrum, where  $k_a = k' + \frac{N}{D}\delta$ .

The narrowband implementation is applicable with two conditions. Firstly, the DFT points in each of the sets  $[k', k' + N/D, \dots, k' + (D-1)N/D]$  should contain at most one non-zero bin. Secondly, the decomposition factor should be limited to

$$D \leq \frac{N}{N_k}, \quad (4.35)$$

where  $N_k$  is the number of active DFT bins. Hence, all contiguous sets of less than or equal  $N/D$  active DFT bins can exploit the narrowband decomposition approach. Furthermore, certain non-contiguous set are also possible if the conditions are met. Figure 4.4 shows a single

case of NB-FC-FB with contiguous set of  $N/D$  active DFT points.

This approach is also possible to derive using the Cooley-Tukey algorithm. The ideas of the narrowband decomposition can be directly applied for pruning the DFT/IDFT while considering the narrowband decomposition conditions. Therefore, dynamic pruning of DFT with arbitrary inputs or outputs can be reached using a similar concept.

#### 4.2.3 Decomposed scheme for uniformly distributed subband scenario

The scenario is considered as uniformly distributed if three conditions are met. Firstly, the zero-phase responses of frequency-masks are identical. Secondly, the subband are not overlapping in the DFT domain. Thirdly, the center frequencies of all subbands are uniformly distributed such that  $k'_0$  is constant. These conditions imply constant size of the short transforms  $L$ . Accordingly, the zero-phase response is denoted as  $P[k]$  for all subbands. The interpolation/decimation factor  $R$  is also constant for all subband. Finally, the third condition implies that the decomposition factor should equal  $R$ . Accordingly, the short transform size is expressed as

$$L = \frac{N}{D}, \quad (4.36)$$

with  $D = R$ . Accordingly, the total number of subbands in the multirate FC based scheme is found as follows:

$$K_{\text{tot}} = \frac{N}{L} = D. \quad (4.37)$$

Considering constant  $k'_0$ , the subband indexes are remapped using  $\Delta$  only. Therefore, the DFT response of the polyphase frequency-mask in (4.19) is expressed as

$$H_s[k', \Delta, d_h] = \frac{1}{D} W_N^{-(k' + L(\Delta + A[k']))(d_h + \tau)} P_{\text{rot}}[k'], \quad (4.38)$$

for transmitter side. For the receiver side, it is expressed as follows:

$$H_a[k', \Delta, d_h] = \frac{1}{D} W_N^{-(k' + L(\Delta + A[k']))(d_h - \tau)} P_{\text{rot}}[k']. \quad (4.39)$$

Here  $P_{\text{rot}}$  is defined as follows:

$$P_{\text{rot}}[k'] = P \left[ \left\langle k' - k'_0 - \frac{L}{2} + LA[k'] \right\rangle_N \right]. \quad (4.40)$$

The zero-phase response is independent from the subband indexing. Therefore, the coefficients of the filter can be combined with the twiddle factor  $W_N^{-dk}$  and  $W_N^{\hat{d}k}$  on the transmitter and receiver sides, respectively. As a result, the input of the transforms of size  $N/D$  is expressed as

$$Y_l[k', d] = \frac{1}{D} W_N^{-(k' + LA[k'])(d + \tau)} P_{\text{rot}}[k'] \sum_{\Delta=0}^{D-1} C_l[\langle k' - k'_0 \rangle, \Delta] W_D^{-\Delta(d + \tau)}, \quad (4.41)$$

for transmitter side. The output of the DFT of size  $D$  can be circularly shifted by  $\tau$  when  $\tau$  is integer, i.e.,  $C_l[k', d + \tau]_D$ .

On the receiver side, the input of the  $\Delta$ th short transform is expressed as follows:

$$\hat{C}_l[k', \Delta] = \frac{1}{D} \sum_{\hat{d}=0}^{D-1} \hat{Y}_l[\langle k' + k'_0 \rangle_{\frac{N}{D}}, \hat{d}] P_{\text{rot}}[\langle k' + k'_0 \rangle_{\frac{N}{D}}] W_N^{(k' + LA[k'])(\hat{d} + \tau)} W_D^{\Delta(\hat{d} + \tau)}. \quad (4.42)$$

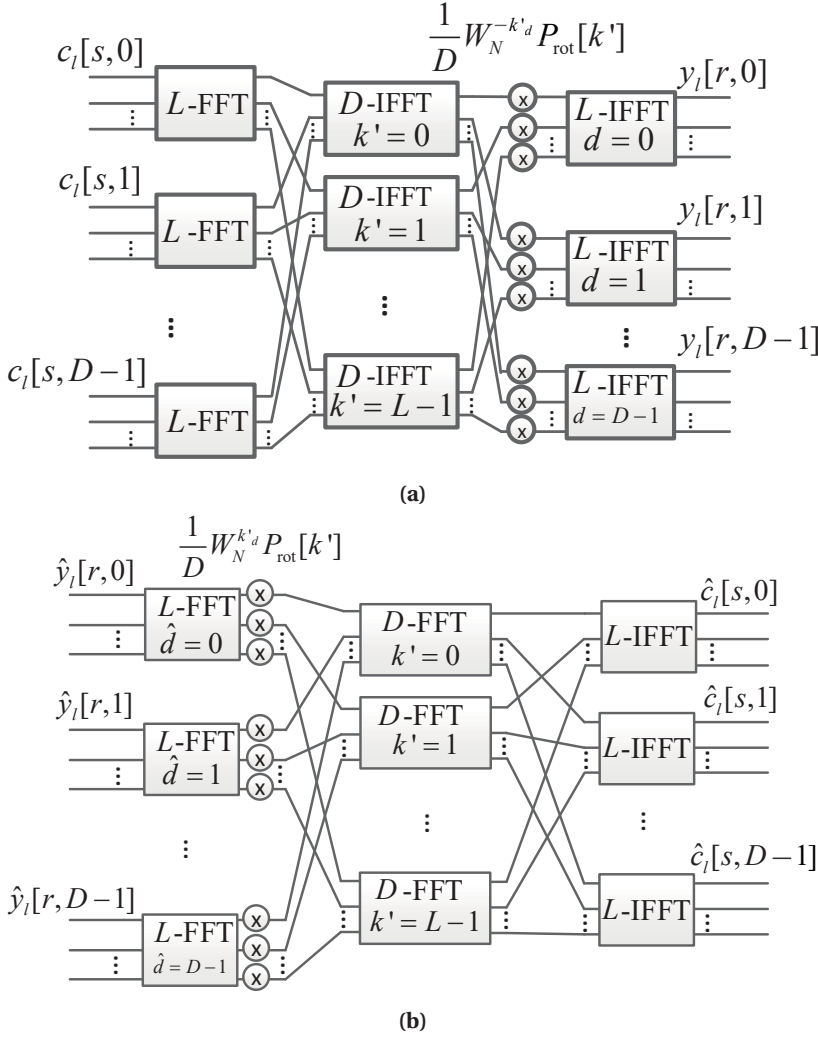


**Figure 4.5:** The structure of UD-FC-FB in (a) SFB/transmitter, and (b) AFB/receiver, where  $k'_d = (k' + LA[k'])(d + \tau)$  and  $\hat{k}'_d = (k' + LA[k'])(\hat{d} + \tau)$ , respectively.

Here,  $\tau$  can be applied by circular shift at the input of the DFT of size  $D$ , only if  $\tau$  is an integer. Figure 4.5 shows the implementation UD-FC-FB for transmitter and receiver sides.

The resulting structure of UD-FC-FB is close to the generic D-FC-FB except for the multiplication by frequency masks. In UD-FC-FB, the frequency-mask is combined with the twiddle factors of the decomposition. However, UD-FC-FB introduces some limitations. Firstly, sub-band overlapping is not possible with this scheme. For example, FBMC/OQAM waveform cannot be realized with this scheme. Obviously, non-uniform subbands are not possible in this scheme. Also, the frequency-domain equalization cannot be embedded with the filter weights. The filter equalization parameter stays before the short transforms. Nevertheless, the scheme is very useful for FMT waveform generation and processing. Specifically, UD-FC-FB shows significant reduction in the computational complexity in the oversampled FMT scenario. With oversampling, the number of  $D$  transforms can be reduced by a factor equal to the

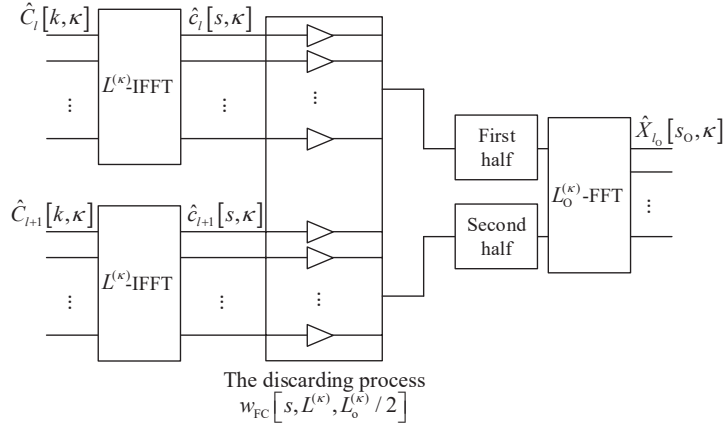


**Figure 4.6:** The processing of the short transform and low-rate OFDM transform at symbol-synchronized FC-F-OFDM receiver with  $\lambda = 0.5$ . The upper and lower short transforms represent the processing of the preceding and following FC blocks, respectively.

oversampling ratio.

#### 4.2.4 Simplified symbol-synchronized FC-F-OFDM receiver

The basic FC-F-OFDM scheme of Section 3.1.1 processes the CP-OFDM signal as a continuous stream of overlapping FC blocks with fixed-length non-overlapping and overlapping parts. With the typical and convenient parametrization, the FC block length is equal to the main OFDM symbol duration (without CP). In this case, the FC blocks are not synchronized to the OFDM symbols. As discussed in [YKLRP18] regarding the transmitter side, there are various benefits if the non-overlapping parts are synchronized to the main parts of the OFDM symbols. This can be achieved by choosing the parameters in such a way that the main OFDM symbol length is an integer multiple of the non-overlapping FC block length. In practice, it is then necessary to arrange the FC blocks non-uniformly with respect to incoming time-domain sequence, basically by not including the CP parts in the non-overlapping parts of FC blocks. In [YKLRP18] this is referred to as symbol-synchronized discontinuous FC processing. One benefit of this approach is that in narrowband allocations, the low sampling rate can be chosen lower than the minimum sampling rate in the basic FC processing model, which is limited by the requirement that the CP length should correspond to an integer number of samples. Furthermore, combining symbol-synchronized FC model with decomposed FC processing results in significant additional savings in the computational complexity of FC-F-OFDM receiver processing also with wideband allocations.

In symbol-synchronized FC-F-OFDM, the overlapping factor should make  $1/(1 - \lambda)$  an integer. This follows from the idea that a low-rate OFDM symbol should consist of an integer number of FC blocks. Figure 4.6 shows the arrangement of the short transforms and low-rate OFDM transform for single subband with  $\lambda = 0.5$ . Each low-rate OFDM symbol is constructed using two FC blocks. Therefore, the upper short transform represents the processing of the first half of the low-rate OFDM symbol, and the lower short transform represents the processing of the second half of the low-rate OFDM symbol. This example can also be generalized for  $\lambda = 3/4, 7/8$ , etc. However,  $\lambda = 1/2$  remains as the practically interesting case due to excessive overlap in the other feasible cases. The structure of Figure 4.6 represents CC processing, and

the decomposition of the CC is applicable in this case. To simplify this implementation, the transform size of low-rate OFDM is assumed to equal the short transform.

Accordingly, the output of the decomposed short transform is defined according to (4.3a) as follows:

$$\hat{c}_l[s, \kappa, \hat{d}_c] = \sum_{k=0}^{\frac{L^{(\kappa)}}{D}-1} \hat{C}_l[Dk + \hat{d}_c, \kappa] W_{\frac{L^{(\kappa)}}{D}}^{-sk}. \quad (4.43)$$

Hence, the output of the short transform at the  $\kappa$ th subband and the  $l$ th FC block is decomposed as follows:

$$\hat{c}_l[s, \kappa] = \sum_{\hat{d}_c=0}^{D-1} \hat{c}_l[s, \kappa, \hat{d}_c] W_{L^{(\kappa)}}^{-\hat{d}_c k}. \quad (4.44)$$

Here, it is assumed that  $D = 1/(1 + \lambda)$ . The discarding process is time-windowing (c.f. (3.7)) that is considered CC process in frequency-domain. The time-window is defined as

$$w_l[s, \kappa] = w_{FC} \left[ s + l \frac{L^{(\kappa)}}{D} + L_0^{(\kappa)}/2, L^{(\kappa)}, L_0^{(\kappa)}/2 \right], \quad (4.45)$$

which is decomposed in the following way:

$$\hat{w}_l[s, \kappa] = W_D^{\hat{d}_w l} W_{L^{(\kappa)}}^{s \hat{d}_w}. \quad (4.46)$$

Finally, the output of the decomposed CC is computed as

$$\begin{aligned} \hat{U}[Dk' + \hat{d}_U, \kappa] &= \sum_{s=0}^{\frac{L^{(\kappa)}}{D}-1} \sum_{\hat{d}_w=0}^{D-1} \sum_{k=0}^{\frac{L^{(\kappa)}}{D}-1} \hat{Q}[s, \kappa, \langle \hat{d}_U - \hat{d}_w \rangle_D, \hat{d}_w] \\ &\quad \times W_{L^{(\kappa)}}^{s \left( \hat{d}_w - \frac{L_0^{(\kappa)}}{2} \langle \hat{d}_U - \hat{d}_w \rangle_D \right)} W_{\frac{L^{(\kappa)}}{D}}^{a_{CC} s} W_{\frac{L^{(\kappa)}}{D}}^{k' s} W_{\frac{L^{(\kappa)}}{D}}^{-k s}, \end{aligned} \quad (4.47)$$

which is the output of the low-rate OFDM transform. Here,  $\hat{Q}[s, \kappa, \langle \hat{d}_U - \hat{d}_w \rangle_D, \hat{d}_w]$  is calculated as follows:

$$\hat{Q}[k, \kappa, \langle \hat{d}_U - \hat{d}_w \rangle_D, \hat{d}_w] = \frac{1}{N} \sum_{l=0}^{D-1} \hat{C}_l[k, \kappa, \langle \hat{d}_U - \hat{d}_w \rangle_D] W_D^{\hat{d}_w l}. \quad (4.48)$$

Accordingly, such processing requires  $L^{(\kappa)}$  DFTs of size  $D$ . Moreover, this implementation requires  $D^2$  transforms of size  $L^{(\kappa)}$ .

Basically, this approach is mostly suitable for  $\lambda = 0.5$  where the decomposition factor  $D = 2$ . This is due to the effect of the  $\lambda$  on the normalization factor of the scheme. Therefore, the increase in the non-overlapping factor results in increase in the computations rates. Moreover, the number of the twiddle factors in (4.47) increases accordingly. Figure 4.7 shows the implementation of the simplified discontinuous FC-F-OFDM with  $\lambda = 0.5$ . Here, three transforms of size  $L^{(\kappa)}$  is replaced by four transforms of size  $L^{(\kappa)}/2$  with two sets of twiddle factors. Every box contains transform and set of twiddle factor. Those components can be implemented as odd-DFT/IDFT block. An efficient implementation of the odd-DFT/IDFT block can be found in [PL96]. This reduces the computational complexity further in the case of  $\lambda = 0.5$ . Detailed discussion about odd-DFT is presented in Appendix A.3.



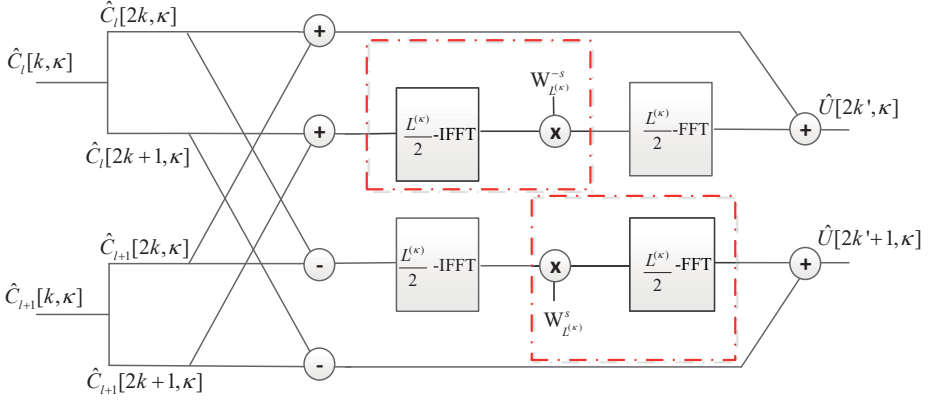


**Figure 4.7:** The implementation of the simplified FC-F-OFDM with  $\lambda = 0.5$ . The red boxed represents the odd-DFT that can be implemented in efficient way.

### 4.3 Analysis of the computational complexity of the decomposed variants

The computational complexity of the decomposition based variant is investigated in this section. We define two functions  $\mu_{\text{GFFT}}[N, D, d]$  and  $\alpha_{\text{GFFT}}[N, D, d]$  that give the required number of real multiplications and real additions, respectively, to implement FFT/IFFT of size  $N/D$  with input or output multiplied by  $W_N^{\pm dk}$  where  $k = 0, 1, \dots, N/D - 1$ . The two functions are defined as

$$\mu_{\text{GFFT}}[N, D, d] = \begin{cases} \mu\left[\frac{N}{D}\right], & \text{for } C \in \{N, \frac{N}{2}, \frac{N}{4}\} \\ \frac{N}{D} \log_2 \frac{N}{D} - \frac{N}{D}, & \text{for } C = \frac{D}{2} \\ \mu\left[\frac{N}{D}\right] + \sigma_{\text{TW}}\left[N, \frac{N}{D}, d\right], & \text{otherwise,} \end{cases} \quad (4.49a)$$

$$\alpha_{\text{GFFT}}[N, D, d] = \begin{cases} \alpha\left[\frac{N}{D}\right], & \text{for } C \in \{N, \frac{N}{2}, \frac{N}{4}\} \\ 3 \frac{N}{D} \log_2 \frac{N}{D} - \frac{N}{D}, & \text{for } C = \frac{D}{2} \\ \alpha\left[\frac{N}{D}\right] + \sigma_{\text{TW}}\left[N, \frac{N}{D}, d\right], & \text{otherwise,} \end{cases} \quad (4.49b)$$

where  $C = \text{gcd}[N, d]$ . Here, the cases of  $C = D/2$  result in the odd-DFT case [PL96]. Furthermore, we define here the needed computational complexity for pruned FFT/IFFT of size  $N$  with single input at index  $k$  and providing the output in the period  $[0, D - 1]$  as

$$\sigma_{\text{Pr}}[N, D, k] = \begin{cases} \frac{N}{2C} - 2 & \text{for } \frac{N}{C} \notin \{1, 2, 4\}, \frac{N}{C} \leq D \\ D + \frac{N}{4C} - 2 & \text{for } \frac{N}{C} \notin \{1, 2, 4\}, \frac{N}{8C} < D < \frac{N}{4C} \\ 3D - 3 & \text{for } \frac{N}{C} \notin \{1, 2, 4\}, D \leq \frac{N}{8C} \\ 0, & \text{otherwise,} \end{cases} \quad (4.50)$$

where  $C = \text{gcd}[N, k]$ . This formula is applicable for both real multiplications and real additions for single input pruning. For single output at  $k$ th index with  $D$  inputs, the required real multiplications are found using (4.50) and the required real additions are found as follows:

$$\alpha_{\text{Pr}}[N, D, k] = \begin{cases} 2 \frac{N}{C} - 2D - 16 & \text{for } \frac{N}{C} \notin \{1, 2, 4\}, \frac{N}{C} \leq D \\ 4D - 2 \left\lceil \frac{8CD}{N} \right\rceil & \text{for } \frac{N}{C} \notin \{1, 2, 4\}, \frac{N}{4C} \leq D < \frac{N}{8C} \\ 3D + \frac{N}{4C} - 4 & \text{for } \frac{N}{C} \notin \{1, 2, 4\}, \frac{N}{8C} < D < \frac{N}{4C} \\ 5D - 5 & \text{for } \frac{N}{C} \notin \{1, 2, 4\}, D \leq \frac{N}{8C} \\ 2D - 2, & \text{otherwise.} \end{cases} \quad (4.51)$$

In (4.50) and (4.51), the computational complexity for  $D \geq N/(4C)$  is based on discarding the redundant multiplications by trigonometric components [Bon86]. In this case, the complex multiplication is realized by four real multiplication and two real additions. This is more effective than the three real multiplications and three real additions realization of complex multiplications. The proof of the formulas (4.49), (4.50) and (4.50) are shown in Appendix A.3 and A.4.

The implementation of D-FC-FB is concluded to be similar to the FC-FB except for the change in the long transform part. Therefore, the short transform complexity formula in (3.33), and the normalization factors in (3.32) and (3.34) are used for computational complexity calculations of D-FC-FB. Regarding the long transform part, the computational complexity is found as follows:

$$\mu_D[N, D] = \sum_{d=0}^{D-1} \mu_{\text{GFFT}}[N, D, d] + \frac{N}{D} \mu[D] \quad (4.52a)$$

$$\alpha_D[N, D] = \sum_{d=0}^{D-1} \alpha_{\text{GFFT}}[N, D, d] + \frac{N}{D} \alpha[D]. \quad (4.52b)$$

The generic decomposed scheme requires  $\langle D-4 \rangle_4$  more real multiplication than the corresponding direct FC scheme. Moreover, the real additions of the decomposed FC increases by the same amount with respect to direct FC schemes.

Similarly, the computational complexity of the short transforms part is computed using (3.33) and the normalization factor is computed using (3.32) and (3.34) for narrowband D-FC (NB-FC) scheme. NB-FC-FB scheme affects only the long transform part. Therefore, the computational complexity of the long transform is computed as

$$\mu_{\text{NB}}[N, D] = D\mu\left[\frac{N}{D}\right] + \sum_{k \in \mathbf{K}} \sigma_{\text{Pr}}[N, D, k] \quad (4.53a)$$

$$\alpha_{\text{NB}}[N, D, A_R] = D\alpha\left[\frac{N}{D}\right] + \sum_{k \in \mathbf{K}} [\langle A_R + 1 \rangle_2 \sigma_{\text{Pr}}[N, D, k] + A_R \alpha_{\text{Pr}}[N, D, k]], \quad (4.53b)$$

for real multiplications and real additions, respectively. Here  $\mathbf{K} \in \{0, 1, \dots, N-1\}$  is the set of active DFT points. The computational complexity of NB-FC-FB scheme has three dominant factors, namely,  $N$ ,  $D$  and  $N_k$ . The complexity of the NB-FC-FB is proportional with  $N$  and  $N_k$ . Nevertheless, the parameterization of the  $N$  and  $N_k$  is not specified by the computational complexity. Therefore, the decomposition factor is the only remaining factor to control the computational complexity. Accordingly, the decomposition factor  $D$  can be determined as

$$D_{\text{lst}} = \frac{N}{(3N_k + 4) \ln 2}, \quad (4.54)$$

for fixed values of  $N$  and  $N_k$  to minimize (4.53a). The optimization of  $D_{\text{lst}}$  is found at the commonly occurring cases in (4.50) which is  $D \leq N/(8C)$ . The value of  $D_{\text{lst}}$  is usually non-power of two. In this document,  $D$  is assumed to be power of 2. Therefore, the actual value of  $D$  should be found empirically by substituting the next smaller and larger power of two values in (4.53a) and comparing the results. For very low number of active DFT point  $N_k \leq 7$ , the optimal value can be obtained by using the condition in (4.35). In general, the NB-FC based scheme reduces the computational complexity by decomposing the long transform part. The long transform is replaced by  $D$  transforms of size  $N/D$  combined with multiplications by twiddle factors. The use of FFT/IFFT pruning reduces the computational complexity of the NB-FC with respect to D-FC. This due to the relation between the number of active DFT bins with the number of multiplication by the twiddle factors of the decomposition. Therefore, the

complexity significance of the NB-FC based scheme appears with low number of active DFT bins. Correspondingly, increase in the number of active bins leads to marginal reduction in computational complexity.

Regarding the UD-FC scheme, it differs from the D-FC scheme in the combination of the frequency-mask coefficients with the twiddle factors of the decomposition. Accordingly, the short transform part of uniformly distributed D-FC (UD-FC) scheme contains only the short transforms. The computational complexity of the short transform part is computed as

$$\mu_{\text{UD-sh}} = B\mu \left[ \frac{L}{o} \right] \quad (4.55a)$$

$$\alpha_{\text{UD-lng}} = B\alpha \left[ \frac{L}{o} \right], \quad (4.55b)$$

where  $o$  is the oversampling factor. Therefore, the scheme is critically sampled when  $o = 1$  and it is oversampled when  $o > 1$ . The short transform in the oversampled case can be implemented by reducing the short transform sizes by the factor of  $o$ . This is also applicable for the FC-FB scheme. The long transform part contains  $L/o$  transforms of size  $D$ ,  $D$  transforms of size  $L$  and the multiplication by the combined filter weights with the twiddle factors of the decomposition. The complexity of the long transform part in UD-FC scheme is computed as

$$\mu_{\text{UD-lng}} = D\mu[L] + \frac{L}{o}\mu[D] + 3D(L-1) \quad (4.56a)$$

$$\alpha_{\text{UD-lng}} = D\alpha[L] + \frac{L}{o}\alpha[D] + 3D(L-1), \quad (4.56b)$$

The complexity reduction of the UD-FC scheme depends on the number of active subbands and the number of the non-zero components in the frequency-mask. Therefore, the UD-FC scheme requires fewer real multiplications than the corresponding direct FC scheme when  $B$  satisfies

$$B > \frac{DL(\frac{1}{o} - 1)(\log_2 D - 3) + 4\frac{L}{o} + D - 4}{2L_H}, \quad (4.57)$$

for given  $N$  and  $L$ . As a result,  $L_H$  is the key parameter defining the computational complexity benefit of UD-FC. Moreover, the complexity reduction becomes more significant when the oversampling factor is increased, depending on the demands of the application.

The reduction in the computational complexity of the simplified discontinuous FC-F-OFDM is only in the short transforms and the low-rate OFDM transform. Those transforms are assumed to be equivalent of size  $L$ . Therefore, the complexity discussion is showing the complexity of this part only without considering frequency-masking and long transform part. Basically, the simplified discontinuous FC-F-OFDM receiver consists mainly of  $L$  transforms of size  $D$  and  $D^2$  transforms of size  $L/D$ . Moreover, around  $D^2$  sets of twiddle factors are required. Therefore, the computational complexity of the simplified discontinuous FC-F-OFDM as

$$\mu_{\text{smp}} = L\mu[D] + D\mu \left[ \frac{L}{D} \right] + \sum_{\hat{d}_U=0}^{D-1} \sum_{\hat{d}_W \in \mathbb{D}[\hat{d}_U]} \mu_{\text{GFFT}}[L, D, \phi[\hat{d}_U, \hat{d}_W]] \quad (4.58a)$$

$$\alpha_{\text{smp}} = L\alpha[D] + D\alpha \left[ \frac{L}{D} \right] + 2\frac{L}{D}(D-1) + \sum_{\hat{d}_U=0}^{D-1} \sum_{\hat{d}_W \in \mathbb{D}[\hat{d}_U]} \alpha_{\text{GFFT}}[L, D, \phi[\hat{d}_U, \hat{d}_W]], \quad (4.58b)$$

for real multiplications and real additions, respectively. Here,  $\phi[\hat{d}_U, \hat{d}_W] = \hat{d}_W - \langle \hat{d}_U - \hat{d}_W \rangle_D L_0/2 + D[(\hat{d}_W - \hat{d}_U)/D]$  is the phase rotation as result of the decomposition in (4.47), and  $\mathbb{D}[\hat{d}_U] = \{0, 1, \dots, D-1\}$  except for the value of  $\hat{d}_U$ . Here, the computation of  $\mu_{\text{GFFT}}$  and  $\alpha_{\text{GFFT}}$  is repeated  $D(D-1)$  times.

**Table 4.1:** The Decomposition Factor Configuration of NB-D-FC Scheme for  $N_k = 32$  active DFT bins and for  $N_k = 64$  active DFT bins in bold fond.

$N$	$N/N_k$	$D_{\max}$	$D_{\text{lst}}$	$D_{\text{opt}}$
128	4/2	4/2	1.71/ <b>0.91</b>	2/2
256	8/4	8/4	3.42/ <b>1.81</b>	4/2
512	16/8	16/8	6.84/ <b>3.62</b>	8/4
1024	32/16	32/16	13.68/ <b>7.24</b>	16/8
2048	64/32	64/32	27.36/ <b>14.48</b>	32/16

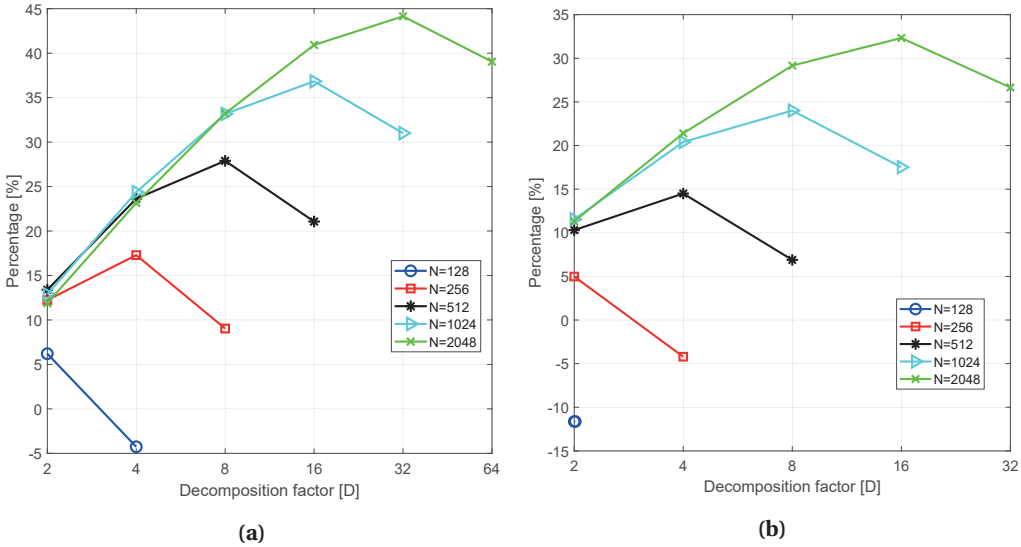


**Figure 4.8:** The reduction in real multiplications given in percentages for NB-FC with respect to direct FC with (a)  $N_k = 32$  and (b)  $N_k = 64$  active frequency bins.

### 4.3.1 Numerical results

The first evaluation compares the computational complexity of NB-FC scheme with respect to the direct FC scheme. As mentioned, the difference in the computational complexity between both schemes occurs in the long transform. Therefore, the following results can be used also to show the effectiveness of the decomposition by pruning DFT with inputs or outputs restricted as mentioned in Subsection 4.2.2. The main factor of the NB-FC approach is the choice of the decomposition factor  $D$ . Considering  $N = 128, 256, 512, 1024$  and  $2048$ , the number of active DFT points is chosen to be 32 or 64 for all values of  $N$ . The number of active frequency bins  $N_k$  is chosen to be 32 and 64 that are equivalent to three and seven overlapping active FBMC/OQAM subbands with  $L = 16$  in FC multirate, respectively. Therefore, the subbands overlap with adjacent subbands in 8 frequency bins. Considering DFT pruning, the choice represents small number of active inputs/outputs with respect to the transform size. The active inputs/outputs are allocated in contiguous way. The parameterization of  $D$  is shown in Table 4.1 where  $D_{\max}$  is the maximum value of  $D$  according to (4.35),  $D_{\text{lst}}$  is the optimal value according to (4.54), and  $D_{\text{opt}}$  is the most efficient power-of-two value of  $D$  near to  $D_{\text{lst}}$ . Figure 4.8(a) shows the reduction in the number of real multiplication for NB-FC with respect

**Table 4.2:** The minimum number of active subbands  $B$  according to (4.57) for achieving complexity reduction in the UD-FC scheme with respect to the direct FC scheme for different values of  $N$  with  $L = 16$ . Two values are considered for the number of non-trivial components in the filter mask,  $L_H \in \{2, 14\}$ . The normal font values are for  $o = 1$  and the bold font values are for  $o = 2$ .

$N$	128	256	512	1024	2048
$L_H = 2$	17/9	19/- <b>21</b>	23/- <b>113</b>	31/- <b>361</b>	47/- <b>985</b>
$L_H = 14$	2.43/ <b>1.3</b>	2.71/- <b>3</b>	3.29/- <b>16.14</b>	4.43/- <b>51.57</b>	6.71/- <b>140.71</b>

to the corresponding direct FC-FB with  $N_k = 32$ . The results shows that the reduction in the real multiplications increases with the increase in the ratio  $N/N_k$ . Moreover, the results confirm the formulation in (4.54). These conclusions are confirmed with  $N_k = 64$  in Figure 4.8(b). Accordingly, NB-FC shows more significance in terms of computational complexity when the number of active DFT points is decreased. The figure shows also cases where the NB-FC approach increases the complexity due to relatively high number of active DFT points.

The second evaluation shows the computational complexity reduction of UD-FC with respect to the corresponding direct FC based scheme. The main complexity factors of the UD-FC scheme are the long transform size  $N$ , the short transform size  $L$ , the oversampling factor  $o$ , the number of non-zero components of the frequency-mask  $L_H$ , and the decomposition factor. Generally, there is no flexibility in the choice of  $D$  since it is defined as  $D = N/L$ . In the following UD-FC test, the short transforms size is fixed to  $L = 16$ . Then, the decomposition factor  $D$  is chosen to be 8, 16, 32, 64, and 128 for long transforms sizes of 128, 256, 512, 1024 and 2048, respectively. Table 4.2 shows the minimum number of active subbands required for effective implementation of the UD-FC in the cases of  $L_H = 2$  and 14 and  $o = 1$  and 2. The required number of active subbands  $B$  is rather high for the critically sampled UD-FC scheme with  $L_H = 2$ . For example with  $N = 128$ ,  $B$  should be greater than the number of available subbands. The increase in  $L_H$  leads to significant decrease in the  $B$  requirement in critically sampled UD-FC. Introducing 2x-oversampling to UD-FC reduces the  $B$  requirement to negative values for  $N > 128$ . This means that complexity reduction is achieved with any number of active subbands. Figure 4.9(a) shows the reduction in real multiplications in percentage for UD-FC scheme with respect to the corresponding direct FC scheme with  $o = 1$  and  $L_H = 14$ . The results show up to 15 % reduction in real multiplications when 87.5 %, 81.25 %, 84.3 %, 90.6 %, and 100 % of total subbands are active for  $N = 128, 256, 512, 1024$ , and 2048, respectively. In Figure 4.9(b), the complexity reduction is shown for 2x-oversampling scenarios, i.e.,  $o = 2$ . The oversampling by 2 shows more reduction in the computational complexity than the critically sampled scenario. For example, 20 % reduction in real multiplications is achieved when the active subbands are 87.5 %, 50 %, and 25 % of the available subbands for  $N = 128, 256$  and 512, respectively. With  $N = 1024$  and  $N = 2048$ , UD-FC scheme provides 20.4 % and 24.2 % reduction in the real multiplication rate, respectively, for single active subband. Generally, the results reveal that the UD-FC scheme achieves systematically increasing complexity benefit with increasing number of active subbands. Furthermore, oversampling decreases significantly the relative computational complexity of UD-FC scheme. There is no reason to use oversampling per scenario but if it is demanded by the application, then the use of UD-FC relaxes the complexity growth. Again, the negative values in Figure 4.9 indicate the cases where UD-FC does not help to reduce the complexity due to low number of active subbands, not satisfying (4.57).

Regarding the simplified discontinuous FC-F-OFDM receiver, the following evaluation considers only the computational complexity of the short FC transforms and the low-rate OFDM

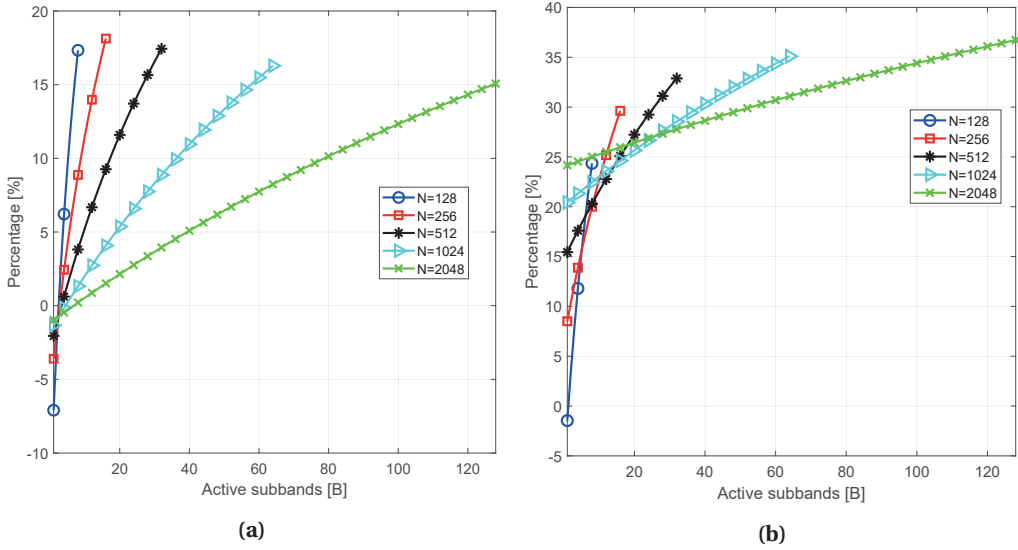


**Figure 4.9:** The reduction in real multiplications given in percentages for UD-FC with respect to direct FC with  $L = 16$  and  $L_H = 14$ . (a) Critically sampled,  $o = 1$ . (b) 2x-oversampling,  $o = 2$ .

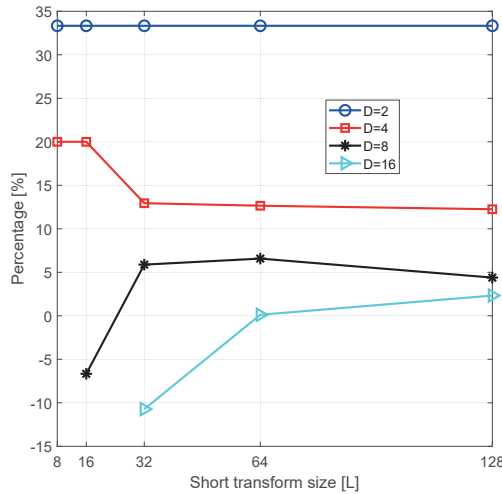


**Figure 4.10:** The reduction in real multiplication rate for the short FC transforms and low-rate OFDM transform of the simplified symbol-synchronized FC-F-OFDM with respect to direct FC implementation.

transform. The computational complexity is computed for  $D = 2, 4, 8$  and 16 representing overlapping factors of  $\lambda = 1/2, 3/4, 7/8$  and  $15/16$ , respectively. Figure 4.10 shows the reduction in the real multiplication rate for simplified symbol-synchronized FC-F-OFDM with respect to the direct FC implementation of the same scheme. The results show that the simplified implementation reduces the real multiplication by 33% for  $D = 2$ , i.e., with 50 % overlap. With higher values of  $D$  the complexity reduction is smaller, and also the complexity of the direct FC scheme grows significantly, so these cases are hardly interesting in practice.

Next, the computational complexities of direct FC-FB and NB-FC-FB based FBMC/OQAM is

**Table 4.3:** The decomposition factor configurations for the pruned CP-OFDM for 5 MHz in normal font and 20 MHz in bold font.

PRBs	$N/N_k$	$D_{\max}$	$D_{\text{lst}}$	$D_{\text{opt}}$
1	43/ <b>171</b>	32/ <b>128</b>	18.47/ <b>73.87</b>	16/ <b>64</b>
2	21/ <b>85</b>	16/ <b>64</b>	9.72/ <b>38.88</b>	8/ <b>32</b>
3	14/ <b>57</b>	8/ <b>32</b>	6.60/ <b>26.38</b>	8/ <b>32</b>
4	11/ <b>43</b>	8/ <b>32</b>	4.99/ <b>19.96</b>	4/ <b>16</b>
5	9/ <b>34</b>	8/ <b>32</b>	4.01/ <b>16.06</b>	4/ <b>16</b>

**Table 4.4:** The decomposition factor configurations for NB-FC-OQAM for 5 MHz in normal font and 20 MHz in bold font.

PRBs	$N/N_k$	$D_{\max}$	$D_{\text{lst}}$	$D_{\text{opt}}$
1	39/ <b>158</b>	32/ <b>128</b>	18.70/ <b>74.80</b>	16/ <b>64</b>
2	20/ <b>82</b>	16/ <b>64</b>	9.78/ <b>39.13</b>	8/ <b>32</b>
3	14/ <b>55</b>	8/ <b>32</b>	6.62/ <b>26.50</b>	8/ <b>32</b>
4	10/ <b>43</b>	8/ <b>32</b>	5.00/ <b>20.03</b>	4/ <b>16</b>
5	8/ <b>34</b>	8/ <b>32</b>	4.02/ <b>16.01</b>	4/ <b>16</b>

evaluated in 5 MHz and 20 MHz LTE-like scenarios. These schemes are denoted as FC-OQAM and NB-FC-OQAM. Moreover, pruned CP-OFDM based on the narrowband decomposition is included in the comparison, together with basic CP-OFDM and traditional polyphase FB based FBMC/OQAM systems as a reference schemes. The latter ones are based on the Phydys prototype filter with overlap factors  $K = 3$  and  $K = 4$ . In FC schemes, the overlapping factor is chosen as  $\lambda = 1/2$ . The CP-OFDM transform lengths are 512 and 2048 for the two cases. Choosing the short transform size as  $L = 16$ , the long transform sizes of the FC based schemes become 4096 and 16384. The computational complexities are evaluated for 1, 2, 3, 4, and 5 active PRBs of 12 subcarriers, corresponding to narrowband allocations, e.g., in an UE transmitter. The decomposition factor configurations for the pruned CP-OFDM for both scenarios are shown in Table 4.3. Besides, the decomposition factors for NB-FC-OQAM in both scenarios are shown in Table 4.4. Figure 4.11 shows the comparison in terms of real multiplications per transmitted symbol. Very significant complexity reduction can be seen for FC based schemes with respect to traditional polyphase FBMC/OQAM, and with narrow allocations, the benefit of the decomposed scheme with respect to direct FC-FB are significant as well. With single active PRB, NB-FC-OQAM requires 31.2 % and 43.5 % lower multiplications rate than FC-OQAM in 5 MHz and 20 MHz scenarios, respectively. Moreover, pruned CP-OFDM reduces the required number of real multiplications by 83.5 % and 87.4 % compared to CP-OFDM in 5 MHz and 20 MHz scenarios, respectively.

The complexity comparison in 5 MHz and 20 MHz LTE scenarios is repeated for F-OFDM considering both direct FC and narrowband decomposed FC schemes. Both schemes use here symbol-synchronized discontinuous processing with  $\lambda = 0.5$  and  $N_H = 2$ . The short transforms sizes are configured to be  $L = 16, 32, 64, 64$ , and  $64$  for 1, 2, 3, 4, and 5 active PRBs, respectively. Simplified discontinuous receiver processing is applied only with NB-FC-F-OFDM, showing the effect of the simplification compared to the decomposition effect. The decomposition



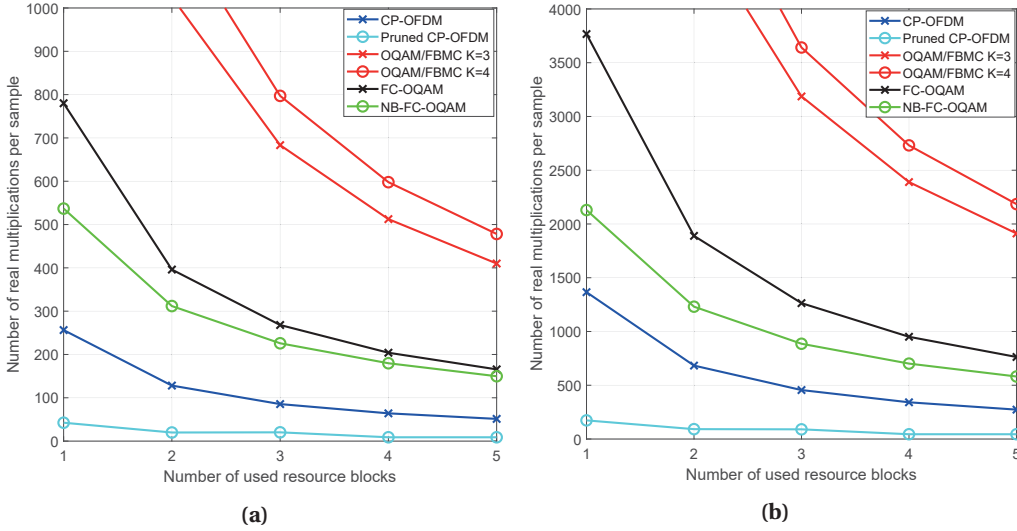


**Figure 4.11:** The real multiplication rates for NB-FC-OQAM compared to FC-OQAM with overlapping factor  $\lambda = 1/2$  and pruned CP-OFDM compared to CP-OFDM in (a) 5 MHz and (b) 20 MHz LTE scenarios.

**Table 4.5:** The decomposition factor configurations for NB-FC-F-OFDM for 5 MHz in normal font and 20 MHz in bold font.

PRBs	$N/N_k$	$D_{\max}$	$D_{\text{lst}}$	$D_{\text{opt}}$
1	32/ <b>128</b>	32/ <b>128</b>	14.21/ <b>56.82</b>	16/ <b>64</b>
2	18/ <b>73</b>	16/ <b>64</b>	8.39/ <b>33.58</b>	8/ <b>32</b>
3	13/ <b>51</b>	8/ <b>32</b>	5.96/ <b>23.83</b>	8/ <b>32</b>
4	10/ <b>39</b>	8/ <b>32</b>	4.62/ <b>18.47</b>	4/ <b>16</b>
5	8/ <b>32</b>	8/ <b>32</b>	3.77/ <b>15.07</b>	4/ <b>16</b>

factor configurations for NB-FC-F-OFDM are evaluated in Table 4.5.

Moreover, RB-F-OFDM with  $N_h = 120$  is included in the comparison as a time-domain filtering based reference scheme. Figure 4.12(a) shows the real multiplication rates for the mentioned schemes in 5 MHz LTE scenario. All FC based schemes are superior with respect to RB-F-OFDM and narrowband decomposition gives clear benefit with low number of subcarriers. Nevertheless, the simplified scheme does not achieve significant reduction in complexity because of low number and size of the short transforms. Similar advantage for discontinuous NB-FC-F-OFDM is achieved in the 20 MHz scenario, as shown in Figure 4.12(b). Furthermore, the decomposed schemes reach lower multiplication rates than the basic CP-OFDM with 1, 2, and 3 active PRBs.

The complexity significance of the simplified discontinuous FC-F-OFDM scheme can be shown in dense spectrum use. Figure 4.13 compares the real multiplication rate of simplified discontinuous FC-F-OFDM with discontinuous FC-F-OFDM and CP-OFDM, as reference, in 5 MHz LTE scenario. In the Figure, 15 to 25 active PRB are assumed, each processed by short transform size of 16. The results show that the simplification reduces the total complexity up to 15 %.

Finally, different FC based FMT schemes are compared in terms of the normalized real multipli-



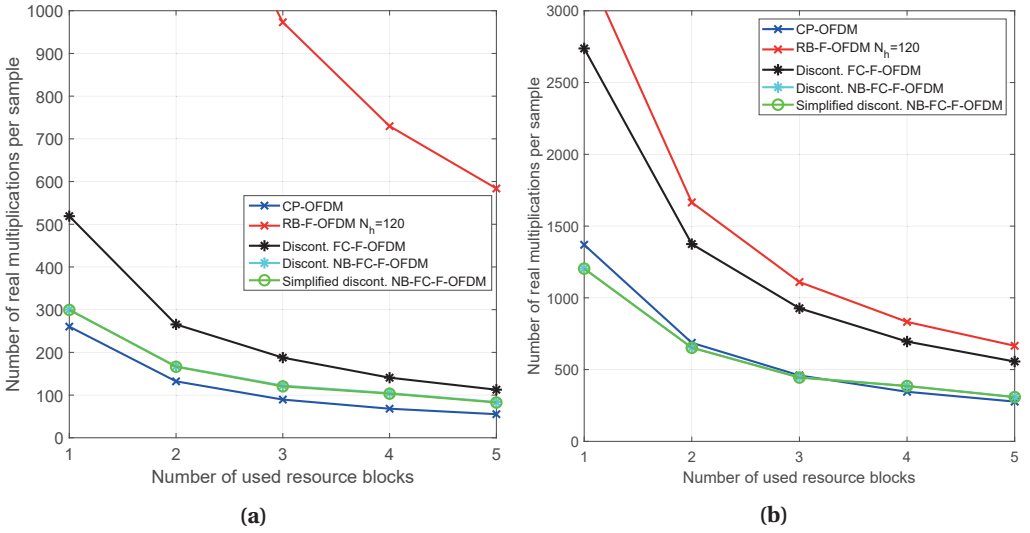


**Figure 4.12:** The real multiplication rates for symbol-synchronized discontinuous FC-based receivers with overlapping factor  $\lambda = 1/2$  and  $L = \{16, 32, 64\}$ . Basic CP-OFDM and time-domain filtered RB-F-OFDM included as reference schemes. (a) 5 MHz LTE-like scenario. (b) 20 MHz LTE-like scenario.

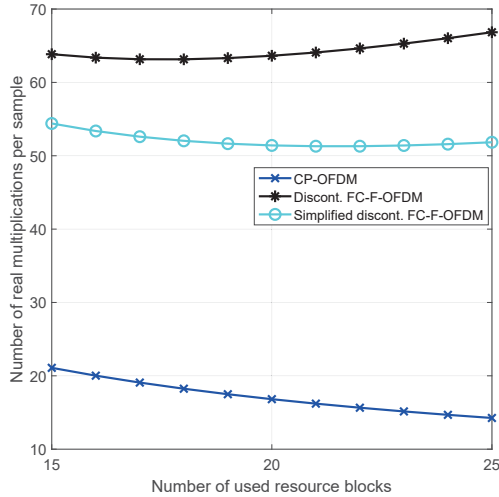


**Figure 4.13:** The real multiplication rate in the 5 MHz LTE scenario for simplified discontinuous FC-F-OFDM compared to discontinuous FC-F-OFDM, both with overlapping factor  $\lambda = 1/2$  and  $L = 16$ . CP-OFDM included as reference.

cation rate. The comparison includes direct FC and UD-FC based FMT with two overlapping factors  $\lambda = 1/2$  and  $1/4$ . 2x-oversampling is assumed, since it provides alias-free subband signals for channel equalization, enhancing the detection performance. Therefore, the subband of size of 16 requires short transforms of size 8. Figure 4.14 shows an example of the real multiplication rate of UD-FC-FMT compared to FC-FMT in 480 kHz bandwidth scenario (i.e., 32 subcarriers with 15 kHz subcarrier spacing) with relatively large number of active subbands. UD-FC provides a significant reduction in the real multiplication rate, from 25.1 to 32.9 %.

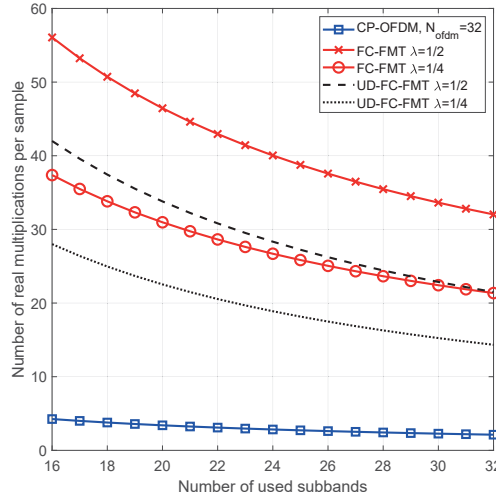


**Figure 4.14:** The normalized number of real multiplications per QAM symbol for UD-FC-FMT and direct FC-FMT as a function of the active bandwidth in 480 kHz bandwidth scenario.

#### 4.4 Chapter summary

In this chapter, the decomposition of CC has been proposed for the implementation of FC based schemes. The decomposed structures are proven to have identical responses with the generic FC implementations. Figure 4.3 provides an evidence to the equality between the D-FC and generic FC based schemes. Generally, the decomposition permits the removal of redundant operations in special transmission cases. For instance, NB-FC scheme has been proposed for the narrowband scenarios with small number of active DFT bins. Analyzing the narrowband scenario with the decomposition reveals a considerable amount of unnecessary operations. The results of Figure 4.8 show that NB-FC scheme is computationally more efficient when the the long transform size increases while the number of active DFT bins remains the same. This complies with complexity formula of NB-FC in (4.53) that shows that the complexity is proportional to the number of active DFT points. Figures 4.11 and 4.12, examining the NB-FC in LTE scenarios show significantly reduced complexity compared to the direct FC based schemes as well as PPN-FBMC and RB-F-OFDM. Moreover, dynamic pruned CP-OFDM based on NB-FC has been proposed showing significant reduction in the computational complexity compared to plain CP-OFDM.

The second decomposition form is proposed for the case of uniformly distributed and non-overlapped subbands cases. The UD-FC schemes show significant complexity reduction especially in the oversampling scenarios. Figure 4.9 confirms the significance of the complexity formula provided in (4.57). The main conclusion is that UD-FC implementation is efficient in terms of computational complexity with the increasing number of active subcarriers and the increasing oversampling rate. In the provided scenarios, 25 % to 33 % reduction in the number of real multiplications has been achieved with dense spectrum use and two times oversampling. Such implementation can be useful on the base station side which usually employs most of the spectral resources.

Finally, the simplified FC-F-OFDM receiver has been proposed to reduce the computational complexity on the low-rate side in the corresponding symbol-synchronized FC-F-OFDM receiver introduced in Chapter 3. This scheme reduces the computational complexity of

FC-F-OFDM by reducing the number of processed FC blocks per OFDM symbol as shown in Figure 3.14. This complexity has been reduced even further using D-FC techniques. The most efficient case is with  $\lambda = 1/2$  which reaches 33 % reduction in the real multiplications, as depicted in Figure 4.10. The overall complexity of the short transforms increases with increasing number of active RBs. Therefore, the reduction in the computational complexity using the simplified FC-F-OFDM becomes more significant in dense spectral use. Figure 4.13 provides an example of the potential reduction in the real multiplication rate by using the simplified FC-F-OFDM with respect to the original symbol-synchronized FC-F-OFDM in 5 MHz scenario.



## Multiplierless Filtered-OFDM Transmitter for Narrow-Band IoT Devices

The future wireless networks are expected to connect the devices, industrial appliances, and even traffic equipment to the internet. This idea is commonly known as internet-of-things (IoT) [SM15, CHW<sup>+</sup>17]. IoT networks are expected to connect massive number of wireless devices to the wireless network. In wide-area narrow-band scenarios, tens of billions of low-power devices with short-burst transmissions use the wireless network in so-called massive machine-type communications (mMTC). 3GPP has proposed a new standard referred to as narrow-band (NB)-IoT for deploying the IoT in stand-alone operation or co-existing with cellular broadband signals such as LTE and GSM. Basically, NB-IoT exploits the current LTE specifications to connect massive number of ultra low-power devices with wide coverage UEs [RMZ<sup>+</sup>16, WLA<sup>+</sup>17, XYW<sup>+</sup>18, MLT<sup>+</sup>18]. In the stand-alone deployment option, NB-IoT can occupy one GSM carrier of 200 kHz leaving the 10 kHz guard-bands on both sides of the spectrum. Besides, NB-IoT can be deployed utilizing the unused RBs within the LTE guard-band or in the active band of the LTE spectrum in so-called guard-band or in-band deployment options, respectively. In these options, the interference with co-existing technologies has to be minimized.

The LTE standard uses CP-OFDM in the downlink and single-carrier frequency-division multiple access (SC-FDMA) (also known as DFT-spread-OFDM (DFT-s-OFDM)) in the uplink. The downlink is defined as the connection from the base-station to UE while the uplink is the connection from the UE to the base-station. Due to the power-efficiency considerations of the low-cost UEs, the UE uses highly non-linear PA making the PAPR a critical issue. Therefore, SC-FDMA is adopted for uplink communication in LTE to mitigate the PAPR issue with multicarrier waveforms. However, SC-FDMA comes with high OOB emissions as in CP-OFDM, which causes interference in coexistence deployments and in asynchronous transmissions. Therefore, 3GPP has allowed transmitter-side spectral enhancements that are transparent to the receiver side [LPP<sup>+</sup>19]. The difficulties in the guard-band and in-band deployments are addressed in [XYW<sup>+</sup>18, RTM<sup>+</sup>17]. Considering small guard-band configurations, highly selective filter with long impulse response is required imposing hardware difficulties for NB-IoT UEs. Therefore, the required spectral enhancements can be achieved by effective subband filtering to relax these issues. Furthermore, 3GPP has introduced new SCS of 3.75 kHz besides the typical SCS of 15 kHz [3GP18a]. This can be considered mixed numerology scenario, especially, with guard-band and in-band deployments. Accordingly, filtering the NB-IoT transmission becomes crucial in this context.

In Chapters 2 and 3, different waveforms with well-localized spectrum have been discussed. FBMC systems based either on time-domain filtering or FC filtering are not compatible with NB-IoT waveform due to the OQAM scheme of FBMC. On the other hand, FC-F-OFDM and RB-F-OFDM are basically constructed upon the CP-OFDM waveform. Therefore, they could be received using typical CP-OFDM receiver. Furthermore, spectrum enhancement techniques such as WOLA-OFDM can be employed in this context with transparent operation to the receiver. These schemes can be considered as candidates to meet the stringent spectral requirements of NB-IoT. However, especially time-domain filtering based solutions require high computational complexity when compared to plain CP-OFDM while providing considerably better spectral localization than WOLA-OFDM. This challenges the implementation of the filtering scheme in low-cost and low-power devices. Furthermore, WOLA-OFDM technique has problems satisfying the OOB emission mask of 3GPP LTE specifications. Moreover, this scheme lacks the potential of enhancing the spectrum for future wireless networks.

This chapter proposes multiplierless filtering solutions for the NB-IoT uplink on the transmitter side. The proposed scheme is based on first generating all the possible time-domain output vectors for each possible complex input sample or group of input samples and then storing those vectors into a look-up table (LUT) for straightforward access [SWA<sup>+</sup>16, SW17]. Hence, the waveform output is reconstructed based on the complex input samples by using the corresponding stored waveform. By using this approach, the IFFT and filtering can be avoided reducing the computational complexity to memory accesses and few real additions. The LUT approach is presented with techniques simplifying the access of the stored waveform. Additionally, LUT variant with no additional computations is also proposed. However, this scheme has high memory requirement for high modulation orders and the memory requirement further increases as the number of subcarriers increases. Therefore, it is feasible only with few active subcarriers. Generally, the LUT approach is also suitable for CP-OFDM and WOLA-OFDM in narrowband scenarios. Besides, it is also possible to implement other schemes such as narrowband FBMC using the LUT approach. The main findings of this chapter are found in [LYL<sup>+</sup>19].

## 5.1 NB-IoT overview

The 3GPP specifications for LTE standard use SC-FDMA and CP-OFDM schemes for uplink and downlink, respectively [DPS14]. LTE standard offers different bandwidths from 1.4 MHz up to 20 MHz with 15 kHz SCS. NB-IoT channel waveform has bandwidth of 180 kHz which is equivalent to a single PRB of LTE. For 15 kHz SCS, 180 kHz corresponds to the 12 subcarriers or 48 subcarriers for 3.75 kHz SCS. NB-IoT supports 1, 3, 6, and 12 subcarrier allocations for 15 kHz SCS while only single subcarrier allocation is allowed for 3.75 kHz SCS. Therefore, transform size of 128 can be used for NB-IoT with 15 kHz SCS. For 3.75 kHz SCS, single carrier transmitter with CP inclusion is sufficient for the implementation. Here, the focus is on the 15 kHz SCS due to the wider variety of subcarrier allocations, while the LUT based implementations are also possible with 3.75 kHz SCS.

Considering frequency-division duplexing (FDD), the frame duration of NB-IoT is 10 ms following the LTE standard. Each frame is divided into 10 subframes that each subframe is divided into two slots. Consequently, the slot duration is 0.5 ms containing 7 symbols. NB-IoT is implemented using normal CP configuration of LTE [XYW<sup>+</sup>18]. Therefore, the CP length within the slot varies such that the CP length of the first symbol is 10 samples or 5.2  $\mu$ s and 9 samples or 4.7  $\mu$ s for the rest of the symbols. The baseband model of NB-IoT assumes the symmetrical allocation of 12 subcarriers around the zero frequency.

Generally, NB-IoT uses quadrature phase-shift keying (QPSK) for multi-tone transmission. However, rotated constellations of  $\pi/2$ -binary phase-shift keying (BPSK) and  $\pi/4$ -QPSK are used for single-tone transmission [3GP18b]. In this chapter, the discussions include the BPSK for multi-tone allocations to extend the LUT approach for possible future developments. Therefore, the constellations of the input samples of the NB-IoT could be defined as

$$X_l[k] = \begin{cases} \frac{1+j}{\sqrt{2}}(-j)^{\Lambda_{k,l}}, & \text{for QPSK} \\ \frac{1+j}{\sqrt{2}}(-1)^{\Lambda_{k,l}}, & \text{for BPSK} \\ \left(\frac{1+j}{\sqrt{2}}\right)^{\langle l \rangle_2 + 1} W_N^{-\Theta_l[k]}(-j)^{\Lambda_{k,l}}, & \text{for } \pi/4\text{-QPSK} \\ j^{\langle l \rangle_2} \left(\frac{1+j}{\sqrt{2}}\right) W_N^{-\Theta_l[k]}(-1)^{\Lambda_{k,l}}, & \text{for } \pi/2\text{-BPSK}, \end{cases} \quad (5.1)$$

where  $\Lambda_{k,l}$  represents the input sample mapping of the  $k$ th subcarrier in  $l$ th OFDM symbol with  $\Lambda_{k,1} \in \{0, 1, \dots, \mathfrak{D} - 1\}$ . Here,  $\mathfrak{D} = 4$  for QPSK and  $\pi/4$ -QPSK and  $\mathfrak{D} = 2$  for BPSK and  $\pi/2$ -BPSK. The phase rotation in the single-tone  $W_N^{-\Theta_l[k]}$  is defined to maintain the phase continuity between consecutive symbols. This is important for  $\pi/2$ -BPSK and  $\pi/4$ -QPSK constellations that are used to reduce PAPR. Therefore, phase continuity is defined as follows:

$$\Theta_l[k] = \sum_{l_c=0}^l (k + 0.5) (N + N_{\text{CP}}[l_c]). \quad (5.2)$$

The phase continuity factor accumulates over the slots making it periodic over 4 slots. Therefore, the phase difference between consecutive slots is  $\pm\pi/2$ . In this document, the single tone with and without phase continuity is also investigated.

## 5.2 Single-input sample models for uplink transmitter

SC-FDMA is the single-carrier version of the CP-OFDM. The SC-FDMA spreads the input sample block of  $K$  subcarriers by DFT of size  $K$ . Those spreaded subcarriers are processed as CP-OFDM symbols in (2.1). Consequently, WOLA or time-domain low-pass filtering can be applied for constructing what is referred here as WOLA based SC-FDMA (WOLA-SC-FDMA) and time-domain filtering based SC-FDMA (F-SC-FDMA). Focusing on F-SC-FDMA, the time-domain filtering uses fixed low-pass filter of bandwidth equal to the channel bandwidth, e.g., 180 kHz for NB-IoT channel. WOLA-SC-FDMA applies time-domain RC window with sufficient roll-off to reduce the OOB emission. Considering normal CP configuration, different CP length is defined for different symbols in the slot. Therefore, the symbol length and the CP length are determined as a function of the symbol index  $l$ , i.e.,  $N_s[l]$  and  $N_{\text{CP}}[l]$ . The variation in the CP length occurs only in the first symbol while the other symbols have the same length. Therefore, the symbol length and the CP length of the first symbol are defined as  $\tilde{N}_s$  and  $\tilde{N}_{\text{CP}}$ , respectively. Besides, the remaining symbol lengths and CP lengths in the slot are denoted as  $\hat{N}_s$  and  $\hat{N}_{\text{CP}}$ , respectively.

In Figure 5.1, F-SC-FDMA based on single-input model is illustrated. The illustrated single-input model is the waveform representation due to single active subcarrier at the  $l$ th processing block. Therefore, this model is crucial for the LUT analyses in the following Section. As discussed in the previous Chapters, the actual implementations of those schemes combine the waveforms produced for each input sample in the final transform. The produced waveform due to single-input sample is expressed as

$$\mathbf{y}_{N_c[l] \times 1}^{(k,l)} = \mathbf{f}_{N_c[l] \times 1}^{(k,l)} X_l[k], \quad (5.3)$$

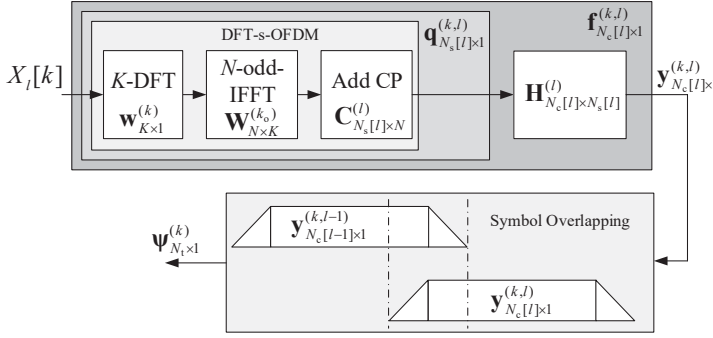


**Figure 5.1:** Single input model for F-SC-FDMA waveform. This model is the basis for LUT implementation. The output is the sum of all waveforms produced by  $K$  subcarriers and  $n_a$  symbols.

where  $k = 0, 1, \dots, K-1$  is the input index of the spreading DFT with size  $K$  in case of SC-FDMA based schemes and  $k = 0, 1, \dots, N-1$  for CP-OFDM based schemes. The length of the output waveform due to single-input sample is defined as  $N_c[l]$ . Considering filtering based processing,  $N_c[l] = N_s[l] + N_h - 1$  is the length of the acyclic or linear convolution. Besides,  $N_c[l] = N_s[l] + 2N_{EX}$  is the length of the time-domain RC window for WOLA based processings. Furthermore,  $N_c[l] = N_s[l]$  is defined for SC-FDMA and CP-OFDM. Here,  $N_s[l] = N + N_{CP}[l]$  is the length of OFDM symbol. In (5.3),  $\mathbf{f}_{N_c[l] \times 1}^{(k,l)}$  is the single-input processing vector for symbol index  $l$  that is expressed as

$$\mathbf{f}_{N_c[l] \times 1}^{(k,l)} = \mathbf{H}_{N_c[l] \times N_s[l]}^{(l)} \mathbf{q}_{N_s[l] \times 1}^{(k,l)}, \quad (5.4)$$

where  $\mathbf{H}_{N_c[l] \times N_s[l]}^{(l)}$  is the acyclic convolution (linear convolution) matrix for low-pass filtering. Here,  $\mathbf{q}_{N_s[l] \times 1}^{(k,l)}$  is the DFT-s-OFDM operator that is defined as

$$\mathbf{q}_{N_s[l] \times 1}^{(k,l)} = \mathbf{C}_{N_s[l] \times N}^{(l)} \mathbf{W}_{N \times K}^{(k_o)} \mathbf{w}_{K \times 1}^{(k)}, \quad (5.5)$$

where  $\mathbf{w}_{K \times 1}^{(k)}$  is the spreading DFT vector that is expressed as

$$\mathbf{w}_{K \times 1}^{(k)} = \left[ 1, W_K^k, \dots, W_K^{k(K-1)} \right]^T, \quad (5.6)$$

and  $\mathbf{W}_{N \times K}^{(k_o)}$  is a modified IDFT matrix with inputs of length  $K$  with  $k_o$  as the first (lowest) subcarrier of the allocation as expressed as

$$\left( \mathbf{W}_{N \times K}^{(k_o)} \right)_{(n+1)(k+1)} = W_N^{-n(k_o+k)} W_N^{-0.5k}, \quad (5.7)$$

where  $n+1$  and  $k+1$  are the matrix row and column indices, respectively, with  $n = 0, 1, \dots, N-1$  is the output index of the odd-IDFT of size  $N$ . Here, the first twiddle factor represents the typical DFT process of single subcarrier while the second twiddle factor represents the half SCS frequency shift. In (5.5),  $\mathbf{C}_{N_s[l] \times N}^{(l)}$  is the CP insertion matrix that is expressed as follows:

$$\mathbf{C}_{N_s[l] \times N}^{(l)} = \begin{bmatrix} \mathbf{0}_{N_{CP}[l] \times (N-N_{CP}[l])} & \mathbf{I}_{N_{CP}[l]} \\ & \mathbf{I}_N \end{bmatrix}. \quad (5.8)$$

For SC-FDMA, the processing vector of the single input model is defined as  $\mathbf{f}_{N_c[l] \times 1}^{(k,l)} = \mathbf{q}_{N_c[l] \times 1}^{(k,l)}$ .

Considering WOLA-SC-FDMA, the single-input processing vector is defined as

$$\mathbf{f}_{N_c[l] \times 1}^{(k,l)} = \mathbf{R}_{N_c[l] \times N_c[l]}^{(l)} \mathbf{q}_{N_c[l] \times 1}^{(k,l)}, \quad (5.9)$$



where  $\mathbf{R}_{N_c[l] \times N_c[l]}^{(l)}$  is diagonal matrix that contains the time-domain window coefficient values  $w_{RC}[n]$  in (2.6). Besides,  $\mathbf{q}_{N_c[l] \times 1}^{(k,l)}$  is defined for WOLA-SC-FDMA as

$$\mathbf{q}_{N_c[l] \times 1}^{(k,l)} = \mathbf{E}_{N_c[l] \times N}^{(l)} \mathbf{W}_{N \times K}^{(k_o)} \mathbf{w}_{K \times 1}^{(k)}, \quad (5.10)$$

where  $\mathbf{R}_{N_c[l] \times N}^{(l)}$  is the matrix for adding cyclic extensions as follows:

$$\mathbf{E}_{N_c[l] \times N}^{(l)} = \begin{bmatrix} \mathbf{0}_{(N_{CP}[l] + N_{EX}) \times (N - (N_{CP}[l] + N_{EX}))} & \mathbf{I}_{N_{CP}[l] + N_{EX}} \\ & \mathbf{I}_N \\ \mathbf{I}_{N_{EX}} & & \mathbf{0}_{N_{EX} \times (N - N_{EX})} \end{bmatrix}. \quad (5.11)$$

The twiddle factors in (5.10) are defined as in (5.6) and (5.7).

The baseband signal due to multiple inputs is produced by the summing all the generated waveforms obtained using the single input model. Therefore, the generation overall baseband waveform is expressed as

$$\boldsymbol{\psi}_{N_t \times 1} = \sum_{k=0}^{K-1} \boldsymbol{\psi}_{N_t \times 1}^{(k)} = \sum_{k=0}^{K-1} \sum_{l=0}^{n_a-1} \mathbf{S}_{N_t \times N_c[l]}^{(l)} \mathbf{v}_{N_c[l] \times 1}^{(k,l)}, \quad (5.12)$$

where  $n_a$  is the total number of OFDM symbols and  $\mathbf{S}_{N_t \times N_c[l]}^{(l)}$  is a shift matrix that is used to represent the overlapping between consecutive symbols for F-SC-FDMA and WOLA-SC-FDMA. For SC-FDMA, the shift matrix acts as parallel-to-serial (P/S) operation. Therefore,  $\mathbf{S}_{N_t \times N_c[l]}^{(l)}$  is expressed as

$$\mathbf{S}_{N_t \times N_c[l]}^{(l)} = \begin{bmatrix} \mathbf{0}_{N_c[l] \times N_v[l]} & \mathbf{I}_{N_c[l]} & \mathbf{0}_{N_c[l] \times N_e[l]} \end{bmatrix}^T, \quad (5.13)$$

where  $N_v[l]$  is the shift of the  $l$ th SC-FDMA symbol in the subframe and it is expressed as

$$N_v[l] = \sum_{l_c=0}^l N_s[l_c - 1], \quad (5.14)$$

with  $N_s[-1] = 0$  and  $N_e[l]$  is the number of remaining samples in the unused parts of the transmission that is defined as

$$N_e[l] = N_t - N_v[l] - N_c[l], \quad (5.15)$$

and  $N_t$  is the total number of the modulated samples in the transmitted waveform as defined as

$$N_t = \left( \sum_{l=0}^{n_a-1} N_s[l] \right) + \alpha, \quad (5.16a)$$

with

$$\alpha = \begin{cases} N_h - 1, & \text{for F-SC-FDMA} \\ 2N_{EX}, & \text{for WOLA-SC-FDMA} \\ 0, & \text{for SC-FDMA.} \end{cases} \quad (5.16b)$$

The single input model proposed in this section can be extended for other waveforms than DFT-s-OFDM by properly modifying the matrix in (5.5). Therefore, the relevant formula (5.5) is replaced by

$$\mathbf{q}_{N_s[l] \times 1}^{(k,l)} = \mathbf{C}_{N_s[l] \times N}^{(l)} \mathbf{W}_{N \times 1}^{(k_o)}, \quad (5.17)$$

for CP-OFDM and F-OFDM. Besides, the formula (5.10) is replaced by the following:

$$\mathbf{q}_{N_c[l] \times 1}^{(k,l)} = \mathbf{E}_{N_c[l] \times N}^{(l)} \mathbf{W}_{N \times 1}^{(k_o)}. \quad (5.18)$$

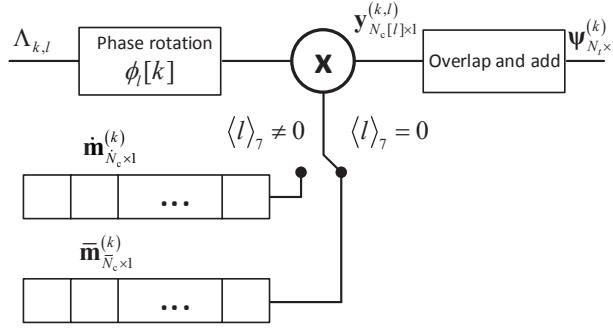


**Figure 5.2:** Basic LUT-OFDM implementation for NB-IoT with BPSK and QPSK modulation. The block diagram shows the processing for the  $k$ th input symbol. Here,  $\bar{\mathbf{m}}_{N_c \times 1}^{(k)}$  and  $\mathbf{m}_{N_c \times 1}^{(k)}$  stand for the stored data for the first symbol and for the rest of symbols in a slot, respectively.

### 5.3 Look-up table based implementations

Considering LUT based implementations, the single-input model is necessary for generating the LUT vectors. The basic concept of LUT is to save the single-input vector  $\mathbf{f}_{N_c[l] \times 1}^{(k,l)}$  for all possibilities. Then, the input sample  $X_l[k]$  is used to fetch the stored waveform. In this section, the details of the LUT-based approach are discussed showing several efficient variants of this technique.

#### 5.3.1 Basic input symbol with LUT

Considering, the formulation of  $X_l[k]$  in (5.1), it is noted that some components of the constellations are independent from the mapping of the input-sample  $\Lambda_{k,l}$ . Therefore, the basic idea is to separate the independent components in (5.1) and store the single-input model as follows:

$$\mathbf{m}_{N_c[l] \times 1}^{(k,l)} = \begin{cases} \frac{1+j}{\sqrt{2}} \mathbf{f}_{N_c[l] \times 1}^{(k,l)}, & \text{for BPSK and QPSK} \\ \left( \frac{1+j}{\sqrt{2}} \right)^{\langle l \rangle_2 + 1} W_N^{-\Theta_l[k]} \mathbf{f}_{N_c[l] \times 1}^{(k,l)}, & \text{for } \pi/4\text{-QPSK} \\ j^{\langle l \rangle_2} \left( \frac{1+j}{\sqrt{2}} \right) W_N^{-\Theta_l[k]} \mathbf{f}_{N_c[l] \times 1}^{(k,l)}, & \text{for } \pi/2\text{-BPSK.} \end{cases} \quad (5.19)$$

As a results,  $\mathbf{m}_{N_c[l] \times 1}^{(k,l)}$  contains  $\mathbf{f}_{N_c[l] \times 1}^{(k,l)}$  that represents all of the necessary processing such as spreading DFT, filtering or time-windowing, and IDFT. This leaves only trivial phase rotations that are depended on the input sample mapping  $\Lambda_l[k]$ . This phase rotation is defined as follows:

$$\phi_l[k] = \begin{cases} (-1)^{\Lambda_{k,l}}, & \text{for } \pi/2\text{-BPSK and BPSK} \\ (-j)^{\Lambda_{k,l}}, & \text{for } \pi/4\text{-QPSK and QPSK.} \end{cases} \quad (5.20)$$

Consequently, it is possible to obtain (5.3) using the stored data in (5.19) that is multiplied by the required phased rotation (5.20) as follows:

$$\mathbf{y}_{N_c[l] \times 1}^{(k,l)} = \phi_l[k] \mathbf{m}_{N_c[l] \times 1}^{(k,l)}. \quad (5.21)$$

This is followed by the overlap-and-add in (5.12) which results in the desired waveform. This process is shown in Figure 5.2 for the BPSK and QPSK cases, showing the waveform generation with basic LUT scheme. For BPSK and QPSK modulations, the stored vector depends on the symbol index  $l$  due to single-input vector  $\mathbf{f}_{N_c[l] \times 1}^{(k,l)}$ . This vector is the same for symbol indices  $l$  with  $\langle l \rangle_7 \neq 0$ . Therefore, two  $\mathbf{m}_{N_c[l] \times 1}^{(k,l)}$  vectors need to be stored for representing single

input samples. Therefore,  $2K$  vectors of  $\mathbf{m}_{N_c[l] \times 1}^{(k,l)}$  are needed for all  $K$  inputs. Let us denote by  $\tilde{\mathbf{m}}_{N_c[l] \times 1}^{(k,l)}$  the vector corresponding to first symbol in the slot and by  $\dot{\mathbf{m}}_{N_c[l] \times 1}^{(k,l)}$  the vector corresponding to rest of the symbols.

For  $\pi/2$ -BPSK case, the stored vector is also dependent on the symbol index  $l$  due to the terms of  $W_N^{-\Theta_l[k]}$  and  $j^{\langle l \rangle 2}$ . The latter term is trivial multiplication that can be omitted from the stored vector. Therefore, two vectors of  $\mathbf{m}_{N_c[l] \times 1}^{(k,l)}$  per input are also needed for  $\pi/2$ -BPSK case when the phase continuity is not assumed. However, in the phase continuous case, altogether seven vectors of  $\mathbf{m}_{N_c[l] \times 1}^{(k,l)}$  vectors per input are needed considering  $\pm\pi/2$  phase rotation between consecutive slots. Regarding  $\pi/4$ -QPSK, the stored vector is dependent on  $((1+j)\sqrt{2})^{\langle l \rangle 2}$  which is non-trivial multiplication. Complex multiplication is needed for odd values of  $l$ . Hence, two  $\mathbf{m}_{N_c[l] \times 1}^{(k,l)}$  vectors are needed for odd and even values of  $l$ . Considering normal CP configuration, four vectors of  $\mathbf{m}_{N_c[l] \times 1}^{(k,l)}$  per input are required without considering phase continuity. This number increases to 14 vectors per input when phase continuity is included. These arrangement in the single-tone implementation are necessary to guarantee multiplication-free implementation of the LUT based approaches.

In this section, the basic LUT implementation does not require any multiplications. However, complex additions are required due to the overlap-and-add processing between the consecutive symbols. Moreover, complex additions are needed to sum the waveforms over the  $K$  inputs. Generally, the analyses in this section can be generalized for higher modulation orders while still maintaining the multiplication-free implementation. However, the number of stored vector will increase dramatically considering also the number of input symbols [SWA<sup>+</sup>16, SW17].

### 5.3.2 Input symbol grouping

The number of complex additions of basic multiplierless LUT scheme can be reduced by processing the input samples group-wise. Now, the stored waveform corresponding to the group of samples should contain all of the possible combinations of  $\Lambda_{k,n}$ . Without loss of generality, assume the grouping of  $K$  input samples into  $N_G$  groups of  $G$  input samples such that  $G = K/N_G$ . Therefore, input sample index  $k$  can be re-indexed for  $r = [0, 1, \dots, N_G - 1]$  and  $g = [0, 1, \dots, G - 1]$  by using the mapping of  $k = rG + g$ .<sup>1</sup> Accordingly, the stored data should contain  $P = G^{\mathfrak{D}}$  vectors for each group of input samples. This number could be reduced to  $P = G^{(\mathfrak{D}-1)}$  if phase rotation is exploited as in the basic form. Each possible combination of the input symbols takes an address index  $p \in \{0, 1, \dots, P - 1\}$ . Each address value represents the location of the stored waveform vectors  $\tilde{\mathbf{m}}_{N_c[l] \times 1}^{(k,l)}$  and  $\dot{\mathbf{m}}_{N_c[l] \times 1}^{(k,l)}$  for one combination such that  $p_l[r]$  is defined as

$$p_l[r] = \check{\Lambda}_{0,r,l} \mathfrak{D}^{G-1} + \check{\Lambda}_{1,r,l} \mathfrak{D}^{G-2} + \dots + \check{\Lambda}_{G-1,r,l}, \quad (5.22)$$

where  $\check{\Lambda}_{g,r,l}$  is the possible mappings of the input-samples that is defined as  $\check{\Lambda}_{0,r,l} = 0$  and  $\check{\Lambda}_{g,r,l} \in \{0, 1, \dots, \mathfrak{D} - 1\}$  for  $g = [1, 2, \dots, G - 1]$ . Consequently, the addresses of the input-sample combinations can be arranged in ascending way as

$$(\mathbf{J}_{G \times P})_{(g+1)(p+1)} = \left\langle \left\lfloor \frac{p}{\mathfrak{D}^{G-(g+1)}} \right\rfloor \right\rangle_{\mathfrak{D}}, \quad (5.23)$$

where  $g+1$  and  $p+1$  are the matrix row and column indices, respectively. As a result, the alternativity matrix  $\mathbf{J}_{G \times P}$  is constructed such that the elements in this matrix counts in the base- $\mathfrak{D}$  numerals. Example of the alternativity matrix with  $\mathfrak{D} = 4$ ,  $G = 3$ , and  $P = 16$  is shown in Figure 5.3. The alternativity matrix helps to provide the required phase rotations of  $G$

<sup>1</sup>Any one-to-one mapping of  $k$  to  $r$  and  $g$  is also possible.

$$\mathbf{J}_{3 \times 16} = \begin{bmatrix} 0 & 0 & 0 & 0 & 0 & 0 & 0 & 0 & 0 & 0 & 0 & 0 & 0 & 0 & 0 & 0 \\ 0 & 0 & 0 & 0 & 1 & 1 & 1 & 1 & 2 & 2 & 2 & 2 & 3 & 3 & 3 & 3 \\ 0 & 1 & 2 & 3 & 0 & 1 & 2 & 3 & 0 & 1 & 2 & 3 & 0 & 1 & 2 & 3 \end{bmatrix}$$

**Figure 5.3:** The alternativity matrix  $\mathbf{J}_{G \times P}$  for QPSK with  $P = 16$  and  $G = 3$  constructed using (5.23). Each column represent one possible combination.

input samples for simple calculation of the memory equivalent of all possible combinations. Consequently,  $P$  waveforms are stored for  $G$  input samples per group as defined as

$$\mathbf{M}_{N_c[l] \times P}^{(r,l)} = \begin{cases} \mathbf{F}_{N_c[l] \times G}^{(r,l)} (-j)^{\circ \mathbf{J}_{G \times P}}, & \text{for QPSK} \\ \mathbf{F}_{N_c[l] \times G}^{(r,l)} (-1)^{\circ \mathbf{J}_{G \times P}}, & \text{for BPSK,} \end{cases} \quad (5.24)$$

where  $(\cdot)^{\circ}$  is element-wise power operation and  $\mathbf{F}_{N_c[l] \times G}^{(r,l)}$  is a matrix constructed as follows:

$$\mathbf{F}_{N_c[l] \times G}^{(r,l)} = [\mathbf{f}_{N_c[l] \times 1}^{(0,r,l)}, \mathbf{f}_{N_c[l] \times 1}^{(1,r,l)}, \dots, \mathbf{f}_{N_c[l] \times 1}^{(G-1,r,l)}]. \quad (5.25)$$

The resulting stored waveform matrix contains all the possible combinations of input-sample mapping while assuming  $\Lambda_{0,r,l} = 0$ . Therefore, phase rotation per group should be defined as follows:

$$\phi_l[r] = \begin{cases} (-1)^{\Lambda_{0,r,l}}, & \text{for } \pi/2\text{-BPSK and BPSK} \\ (-j)^{\Lambda_{0,r,l}}, & \text{for } \pi/4\text{-QPSK and QPSK.} \end{cases} \quad (5.26)$$

The waveform address in the memory represents a column of the stored matrix  $\mathbf{M}_{N_c[l] \times P}^{(r,l)}$ . The waveform address should be modified to the correct address  $\rho_l[r]$  of specific set of  $G$  inputs considering the phase rotation  $\phi_l[r]$ . This means that the waveform address is selected according to the  $G$  input samples as follows:

$$\rho_l[r] = \langle \Lambda_{1,r,l} - \Lambda_{0,r,l} \rangle \mathfrak{D} \mathfrak{D}^{G-2} + \langle \Lambda_{2,r,l} - \Lambda_{0,r,l} \rangle \mathfrak{D} \mathfrak{D}^{G-3} + \dots + \langle \Lambda_{G-1,r,l} - \Lambda_{0,r,l} \rangle \mathfrak{D}. \quad (5.27)$$

Finally, the LUT waveform per group can be calculated as

$$\boldsymbol{\psi}_{N_t \times 1}^{(r)} = \sum_{l=0}^{n_a-1} \phi_l[r] \mathbf{S}_{N_t \times N_c[l]}^{(l)} \mathbf{A}_{N_c[l] \times 1}^{(r,l)}, \quad (5.28)$$

where  $\mathbf{A}_{N_c[l] \times 1}^{(r,l)}$  is the  $(\rho_l[r] + 1)$ th column of the stored matrix  $\mathbf{M}_{N_c[l] \times P}^{(r,l)}$ . Accordingly, the total output is the sum over all input groups  $r = 0, 1, \dots, N_G - 1$ . The input sample grouping and the idea of fetching the waveform from the pre-calculated memory is shown in Figure 5.4 for  $G = 3$  and  $P = 16$ .

In normal CP configuration, the first symbol in the slot requires  $N_G$  matrices of the stored waveforms for each group. Moreover, another  $N_G$  matrices per group is needed for the remaining symbols of the slot. Hence,  $2N_G$  matrices of  $\mathbf{M}_{N_c[l] \times P}^{(r,l)}$  is required with input sample grouping approach. Hence, significant increase in the memory requirement is expected with input-sample grouping based LUT (G-LUT). Nevertheless, the number of additions needed for G-LUT implementation is reduced because the number of produced waveforms is reduced from  $K$  waveforms to  $N_G$  waveforms.

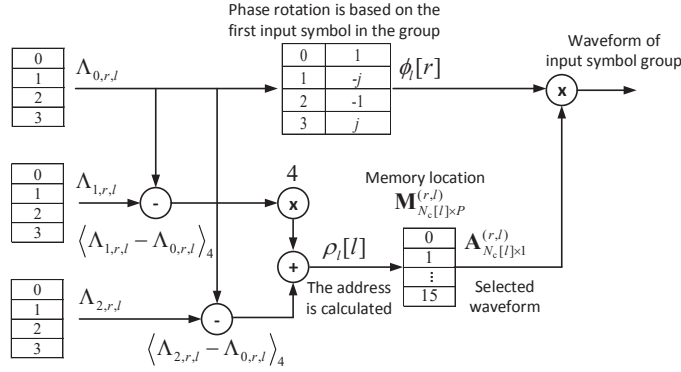


**Figure 5.4:** Example of waveform construction and data allocation of grouped  $G$  input samples of LUT using QPSK. The number of samples in group is  $G = 3$  and the number of alternatives is  $P = 16$  for the  $r$ th group.

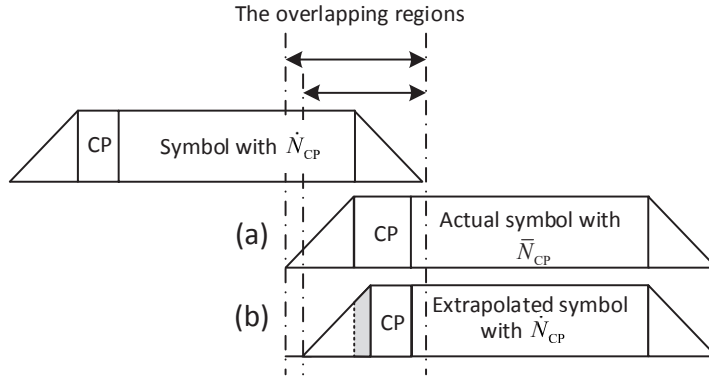


**Figure 5.5:** Illustration of the overlapping with (a) long CP and (b) extrapolated CP. The shaded parts of the symbol represents the extrapolated section of the CP.

### 5.3.3 LUT based scheme with CP extrapolation

In the presented LUT variants, the memory size increases due to the varying CP length in the slot. Single waveform matrix should be stored for the first symbol of the slot, while 6 symbols in the slot need one waveform matrix to be stored in the memory. The idea is to reduce the CP length of the first symbol in the slot to match the other CP lengths for the remaining symbol. Considering NB-IoT configuration, the extra length of this CP is zero-padded. Accordingly, the CP can be roughly extrapolated by the filtering or WOLA process. This should be performed without changing the shift matrix  $\mathbf{S}_{N_t \times N_c[l]}^{(l)}$  in (5.13). It was verified by simulations that the effect of this approach on the link performance is insignificant. Figure 5.5 shows the overlapping process with CP extrapolation. This modification updates the CP matrix for the first symbol in the slot as

$$\bar{\mathbf{C}}_{\tilde{N}_s \times N} = \begin{bmatrix} \mathbf{0}_{(\tilde{N}_{CP} - \tilde{N}_{CP}) \times N} \\ \mathbf{0}_{\tilde{N}_{CP} \times (N - \tilde{N}_{CP})} & \mathbf{I}_{\tilde{N}_{CP}} \\ \mathbf{I}_N \end{bmatrix}, \quad (5.29)$$

for F-SC-FDMA. Considering WOLA-SC-FDMA, cyclic extension is added as follows:

$$\tilde{\mathbf{E}}_{\tilde{N}_c \times N}^{(l)} = \begin{bmatrix} \mathbf{0}_{(\tilde{N}_{CP} - \dot{N}_{CP}) \times N} & & \\ \mathbf{0}_{(\dot{N}_{CP}[l] + N_{EX}) \times (N - (\dot{N}_{CP}[l] + N_{EX}))} & \mathbf{I}_{\dot{N}_{CP}[l] + N_{EX}} & \\ & \mathbf{I}_N & \\ \mathbf{I}_{N_{EX}} & & \mathbf{0}_{N_{EX} \times (N - N_{EX})} \end{bmatrix}. \quad (5.30)$$

Therefore, the stored waveform matrix for the first symbol in slot is equivalent to stored waveform matrix of the other symbols in the slot except for  $(\tilde{N}_{CP} - \dot{N}_{CP})$  zeros at the beginning of the stored waveform matrix. Accordingly, the stored data consists of  $N_G$  matrices of  $\mathbf{M}_{\tilde{N}_c \times P}^{(r)}$  that are calculated according to (5.24) for all values of  $l$ . In this document, CP extrapolation with LUT is denoted as extrapolated CP based LUT (E-LUT).

### 5.3.4 Storing the symbol overlap-and-add

The number of complex additions can be reduced even more by storing the overlapping parts of F-SC-FDMA and WOLA-SC-FDMA symbols. Actually, the LUT based schemes can be implemented with very low-complexity by properly modifying the way how the waveforms are stored in the memory. It has been shown that the adjacent symbols in WOLA and filtering based implementations overlap requiring complex additions. Accordingly, the LUT can contain also all the alternative combinations of the overlaps between the adjacent symbols. In this approach, the waveform creation and storage are similar to the input-sample grouping considering the extrapolation ideas. Generally, the processed symbol by WOLA or filtering can be divided into two main parts. The non-overlapping part corresponds to the samples within the symbol that are not interfered with the adjacent symbol. The stored waveform matrix for the non-overlapping part can be obtained according to (5.24) with addressing according to (5.27). The second part of the symbol is the overlapping part that is analyzed in the following discussion. To store all the possible combinations of the overlapping parts, the number of the possible combinations is found as  $P' = \mathfrak{D}^{2G-1}$  considering the grouping of the input samples to  $N_G$  groups of  $G$  input samples. Let the address index of  $p' \in \{0, 1, \dots, P' - 1\}$  for the stored overlapping regions be

$$\begin{aligned} p'_l[r] = & \check{\Lambda}_{0,r,l} \mathfrak{D}^{2G-1} + \check{\Lambda}_{1,r,l} \mathfrak{D}^{2G-2} + \dots + \check{\Lambda}_{G-1,r,l} \mathfrak{D}^G \\ & + \check{\Lambda}_{0,r,l+1} \mathfrak{D}^{G-1} + \check{\Lambda}_{1,r,l+1} \mathfrak{D}^{G-2} + \dots + \check{\Lambda}_{G-1,r,l+1}, \end{aligned} \quad (5.31)$$

where  $\check{\Lambda}_{g,r,l}$  is the possible mapping of the  $l$ th input-sample that is defined as  $\check{\Lambda}_{0,r,l} = 0$  and  $\check{\Lambda}_{g,r,l} \in \{0, 1, \dots, \mathfrak{D} - 1\}$  for  $g = [1, 2, \dots, G - 1]$ . Besides,  $\check{\Lambda}_{g,r,l+1}$  is the possible mapping of the  $(l + 1)$ th input-sample that is defined as  $\check{\Lambda}_{g,r,l+1} \in \{0, 1, \dots, \mathfrak{D} - 1\}$  for  $g = [0, 1, \dots, G - 1]$ . Accordingly, the alternativity matrix for overlap storing is created in similar way as (5.23) such that  $g = 0, 1, \dots, 2G - 1$  and  $p = 0, 1, \dots, P' - 1$ . Consequently the stored matrix of the overlapping waveform can be computed as

$$\mathbf{M}_{\tilde{N}_c[l] \times P'}^{(r,l)} = \begin{cases} \mathbf{T}_{\tilde{N}_T[l] \times 2G}^{(r,l)} (-j)^{\circ \mathbf{J}_{2G \times P'}}, & \text{for QPSK} \\ \mathbf{T}_{\tilde{N}_T[l] \times 2G}^{(r,l)} (-1)^{\circ \mathbf{J}_{2G \times P'}}, & \text{for BPSK,} \end{cases} \quad (5.32)$$

where  $N_T[l] = N_h - 1 - (N_{CP}[l] - \dot{N}_{CP})$  for F-SC-FDMA scheme and  $N_T[l] = 2N_{EX} - (N_{CP}[l] - \dot{N}_{CP})$  for WOLA-SC-FDMA scheme. Here,  $\mathbf{T}_{\tilde{N}_T[l] \times 2G}^{(r,l)}$  is constructed as

$$\mathbf{T}_{\tilde{N}_T[l] \times 2G}^{(r,l)} = \left[ \mathbf{f}_{N_T[l] \times 1}^{(0,r,l)}, \mathbf{f}_{N_T[l] \times 1}^{(1,r,l)}, \dots, \mathbf{f}_{N_T[l] \times 1}^{(G-1,r,l)}, \mathbf{f}_{N_T[l+1] \times 1}^{(0,r,l+1)}, \mathbf{f}_{N_T[l+1] \times 1}^{(1,r,l+1)}, \dots, \mathbf{f}_{N_T[l+1] \times 1}^{(G-1,r,l+1)} \right], \quad (5.33)$$

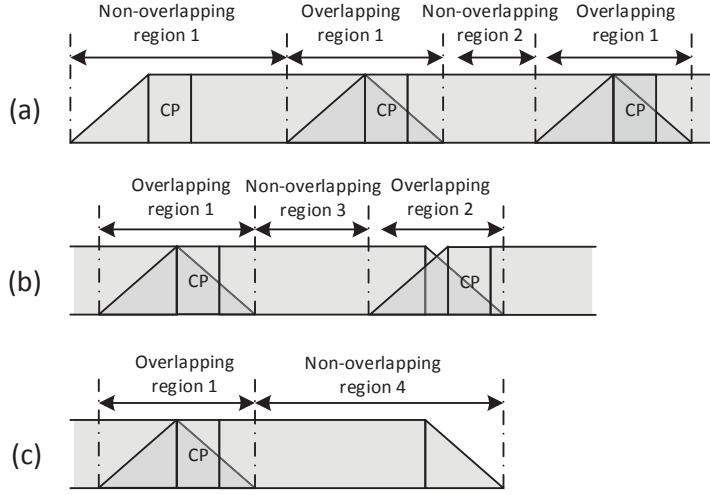


**Figure 5.6:** Illustration of non-overlapping and overlapping parts at the (a) beginning, (b) middle and (c) end of the transmitted symbols.

where  $\mathbf{f}_{N_T[l] \times 1}^{(g,r,l)}$  is the last  $N_T[l]$  samples of  $\mathbf{f}_{N_C[l] \times 1}^{(g,r,l)}$  and  $\mathbf{f}_{N_T[l+1] \times 1}^{(g,r,l+1)}$  is the first  $N_T[l+1]$  samples of  $\mathbf{f}_{N_C[l+1] \times 1}^{(g,r,l+1)}$ .

The address of the stored overlapping waveform can be computed considering  $\Lambda_{0,r,l}$  as follows:

$$\begin{aligned} \rho'_l[r] = & \langle \Lambda_{1,r,l} - \Lambda_{0,r,l} \rangle \mathfrak{D}^{2G-2} + \dots + \langle \Lambda_{G-1,r,l} - \Lambda_{0,r,l} \rangle \mathfrak{D}^G \\ & + \langle \Lambda_{0,r,l+1} - \Lambda_{0,r,l} \rangle \mathfrak{D}^{G-1} + \dots + \langle \Lambda_{G-1,r,l+1} - \Lambda_{0,r,l} \rangle \mathfrak{D}. \end{aligned} \quad (5.34)$$

Then, the overlapping waveform is  $(\rho'_l[r] + 1)$ th column of  $\mathbf{M}_{N_C[l] \times P'}^{(r,l)}$  that is multiplied by  $(-1)^{\Lambda_{0,r,l}}$  for BPSK and  $(-j)^{\Lambda_{0,r,l}}$  for QPSK.

Figure 5.6 shows the overlapping and non-overlapping parts of the symbol. Overlapping region 2 represents the boundaries between the slots and overlapping region 1 represents all other symbol boundaries within a slot. The boundaries between the slots contain the extrapolated CP. Therefore, the stored overlapping waveform contains two  $N_G$  overlap waveform matrices. The non-overlapping regions 1 and 4 represent the beginning and the end of the transmission, respectively. Non-overlapping regions 2 and 3 represent the middle part of the symbol in the middle of the transmission. Therefore, the stored waveform contains one set of  $N_G$  different waveforms matrices  $\mathbf{M}_{N_C \times P}^{(r)}$  which are sufficient for the implementation of all the non-overlapping regions. In this document, overlap storing with LUT is denoted as overlap storing based LUT (O-LUT).

## 5.4 LUT wordlength requirements

In the NB-IoT implementations, the channel bandwidth is 180 kHz and, therefore, the smallest possible transforms size is 128 in order to have an integer CP length. The output of the LUT based implementation is expected to be equivalent to the corresponding waveform from the conventional implementation apart from the finite wordlength effects. Considering finite-wordlength implementations, the number of arithmetic operations in LUT approach are considerably lower than in conventional time-domain filtering or windowing based approaches.

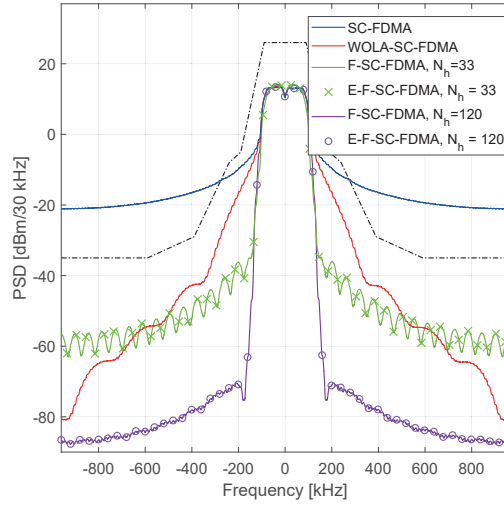


**Figure 5.7:** PSDs of the infinite-precision 12-tone SC-FDMA and WOLA-SC-FDMA waveforms with  $N_{EX} = 5$  and  $N_W = 10$  as well as F-SC-FDMA waveform with filter lengths of  $N_h = \{33, 120\}$  considering normal and extrapolated CP configurations.

In finite-precision realizations, the truncation of the wordlength after the arithmetic operations introduces quantization error that accumulates through the waveform processing resulting to so-called quantization noise. In this section, LUT based waveforms are evaluated in finite-wordlength implementations showing the minimum wordlength requirements in different cases. This evaluation focuses on WOLA-SC-FDMA based LUT (LUT-W) and F-SC-FDMA based LUT (LUT-F) approaches with different variants. The finite-wordlength implementations are scaled based on worst-case scaling. In other words, the internal signal levels are scaled such that no overflow occurs. Focusing of NB-IoT specification, the LUT based schemes are evaluated for in-band and OOB emissions and EVM specified by 3GPP in [3GP18a]. The baseband model is used in the simulations considering single-tone, 3-tone, 6-tone, and 12-tone cases corresponding to 1, 3, 6 and 12 subcarriers, respectively. The subcarriers are allocated at the edge of 180 kHz allocation, which is the most challenging scenario in the sense of OOB emissions. The simulations use the maximum power of class-C which is 23 dBm for transmission bandwidth. This comes with maximum power reduction of 0.5 dB, 1 dB, and 2 dB for edge allocations of 3-tone, 6-tone and 12 tone, respectively. As a result, the transmission power is 23 dBm, 22.5 dBm, 22 dBm and 21 dBm for single-tone, 3-tone, 6-tone and 12-tone allocations, respectively. The following simulations have been evaluated using 50 subframes. In addition, F-SC-FDMA and LUT-F use RRC low-pass filter with impulse response length of  $N_h = \{33, 120\}$ , 180 kHz bassband, and 30 kHz transition band. WOLA-SC-FDMA and LUT-W use time-domain window with  $N_{EX} = 5$  and  $N_W = 10$ . Figure 5.7 shows the PSDs of SC-FDMA, WOLA-SC-FDMA, F-SC-FDMA with  $N_h = 33$ , and F-SC-FDMA with  $N_h = 120$  considering maximum power class-C maximum power reduction (MPR) with infinite-precision arithmetic and linear PA. This shows that the plain CP-OFDM does not satisfy the OOB mask requiring spectral enhancement techniques. F-SC-FDMA is examined in the extrapolated CP and the non-extrapolated CP cases. The resulted PSDs of the extrapolated cases are indistinguishable from the normally implemented CP for  $N_h = 33$  and 120. Therefore, the extrapolation technique has a negligible effect on the PSD when employed with the LUT approach.

Figure 5.8 shows the OOB and in-band emissions for SC-FDMA and F-SC-FDMA with infinite-



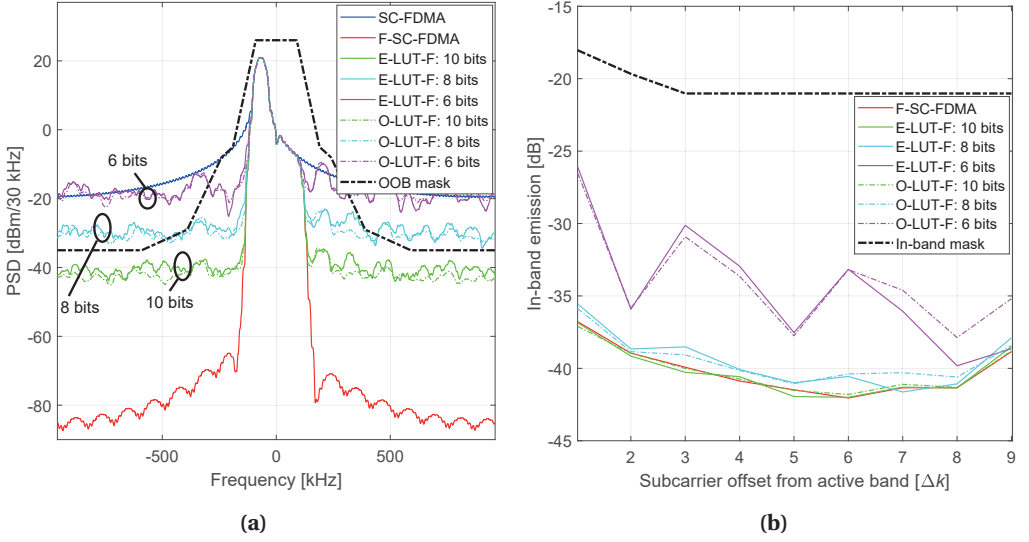


**Figure 5.8:** (a) OOB and (b) in-band emissions for the three-tone case with group size of one with 6, 8, and 10 bit LUT wordlengths, QPSK modulation, filter length of  $N_h = 120$ , and 22.5 dBm transmission power assuming linear PA. SC-FDMA and F-SC-FDMA are shown with infinite-precision as references, along with the OOB and in-band emission masks of 3GPP specification [3GP18b].

precision arithmetic and F-SC-FDMA based E-LUT (E-LUT-F) and F-SC-FDMA based O-LUT (O-LUT-F) with 6, 8, and 10 bit wordlength in 3-tone case. The filtering based schemes use filter length of  $N_h = 120$  and LUT based schemes consider group size of one ( $G = 1$ ) with linear PA. The OOB emissions show the leakage power outside the NB-IoT channel while in-band emissions show the relative power of the unused subcarriers to the average received power on active subcarriers. The basic SC-FDMA does not produce any in-band interference because the evaluation is performed with linear PA and without noise and channel. The OOB emissions of SC-FDMA are always higher than OOB mask while F-SC-FDMA reduces the OOB emissions to  $-80$  dB as shown in Figure 5.8(a). With finite-precision arithmetic, the OOB emissions of the LUT-F variants increase as the wordlength decreases. Therefore, the OOB mask is not satisfied by OOB emissions of LUT-F variants with 6 and 8 bit wordlengths. With 10 bit wordlength, OOB emissions of LUT-F variants satisfy the OOB mask. On the other hand, all of the LUT-F variants satisfy the in-band emission mask as shown in Figure 5.8(b). Moreover, the difference between E-LUT-F and O-LUT-F in OOB and in-band emissions is negligible. Generally, the difference between E-LUT and O-LUT variants is quite insignificant in terms of minimum wordlength requirements.

Figure 5.9 shows the resulting EVM for single-tone  $\pi/2$ -BPSK and 12-tone cases with QPSK for E-LUT-F with  $N_h = 33$ , E-LUT-F with  $N_h = 120$ , and WOLA-SC-FDMA based E-LUT (E-LUT-W). The EVM results show the imperfections due to the finite wordlength and filtering. The used filtering harms the orthogonality of the subcarriers resulting in non-zero EVM in any case. 3GPP specifications allow 17.5 % (15.2 dB) EVM with QPSK modulation. However, only the level of 14 % (20 dB) of maximum EVM can be reached due to quantization. Generally, filtering with long filter and WOLA processing provide better EVM than the filtering with short filter. Moreover, the input-sample grouping reduces the EVM due to the reduction in the quantization error. The minimum wordlengths for different LUT configurations are shown in Table 5.1. It is indicated that 5 to 7 bit wordlengths are sufficient to satisfy the targeted EVM requirements.

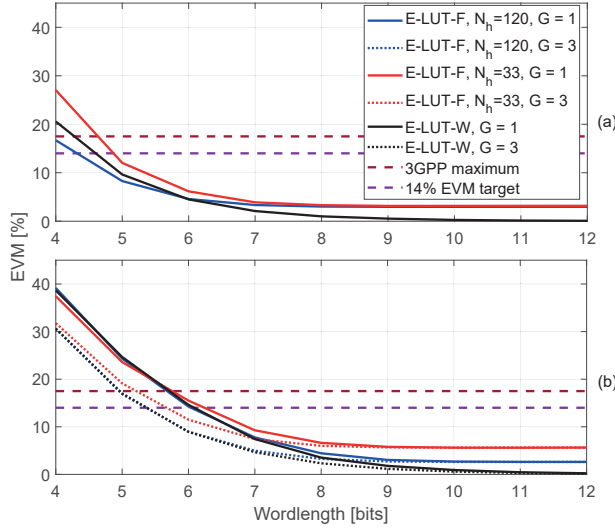


**Figure 5.9:** EVM as a function of the wordlength in bits for E-LUT-W and E-LUT-F with filter length of  $N_h = 120$  or  $N_h = 33$ . (a) Single-tone case with  $\pi/2$ -BPSK and (b) 12-tone case with QPSK.

**Table 5.1:** The minimum wordlengths required to reach the OOB and in-band emissions masks and at most 14 % EVM for different CP extrapolation based LUT configurations. The upper numbers represent WOLA-based LUT and the middle and lower numbers represent filter lengths of  $N_h = \{33, 120\}$ , respectively. Single entry indicates common value for all cases.

Subband size	Group size	Wordlength limiting metric		
		OOB	In-band	EVM
1	1	10		
		10	4	5
		9		
3	1		5	
		10	6	6
	3	9	4	5
6	1		7	
		10	7	6
	3		6	
		9	5	5
12	1	10	-	7
	3	10	-	
		9	-	6
		10	-	

The results shown in Table 5.1 indicate that the OOB emission mask is the most critical metric for specifying the minimum wordlength requirement. Generally, the grouping with  $G = 3$  reduces the minimum requirements by 1 bit in single-tone, 3-tone, and 6-tone cases. The minimum required wordlength considering OOB, in-band, and EVM requirements is 9 or 10

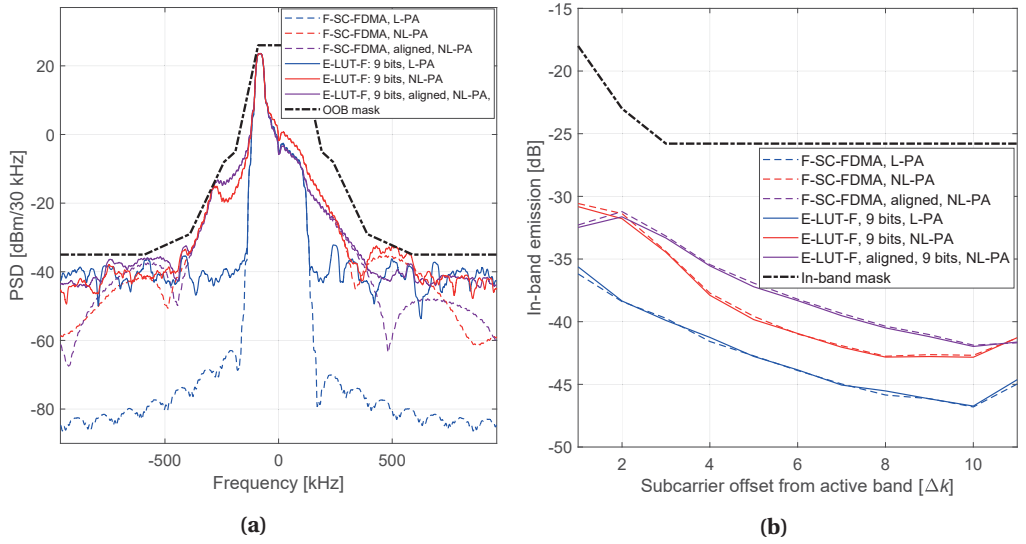


**Figure 5.10:** (a) OOB and (b) in-band emissions for the single-tone case with  $\pi/2$ -BPSK modulation, filter length  $N_h = 120$ , 9 bit LUT wordlength, and 23 dBm transmission power with linear (L-PA) and non-linear PA (NL-PA) models. The E-LUT-F results are shown with phase continuity (aligned) and without phase continuity. F-SC-FDMA cases without quantization are shown as reference along with the OOB masks of 3GPP specification [3GP18b].

bits. With 12 to 14 bit wordlengths, LUT based schemes can satisfy 3GPP specification with reduced OOB emissions.

Then, LUT is evaluated with practical non-linear PA model for NB-IoT transmitter. The PA model is a memoryless AM-AM and AM-PM conversion model based on measurements of a commercial CMOS power amplifier for mMTC devices. The following results evaluate the effect of the phase continuity for single-tone allocation with non-linear PA. Figure 5.10 shows the OOB and in-band emissions of single-tone E-LUT-F with infinite-precision DFT-s-OFDM waveform as a reference. The results indicate that the OOB emissions of E-LUT-F are below the OOB mask with and without phase continuity. Moreover, the effect of the phase continuity on in-band emission is insignificant. Generally, PA effects appear as spectral regrowth in the OOB emissions. However, the effect of finite-precision arithmetic is clearly visible in frequencies with 400 kHz offset from the channel center. Moreover, the impact of the phase alignment in single-tone case is negligible, that is, the phase-aligned single-tone waveform did not provide clear benefit over the non-aligned one. For other tone allocations, the simulations with non-linear PA show that the minimum wordlength requirements of Table 5.1 are also valid for LUT-F. Nevertheless, in certain cases, the minimum wordlength to satisfy the in-band mask increases to 7 and 8 for 3-tone and 6-tone of  $G = 1$ , respectively.

Figure 5.11 compares the OOB emissions of E-LUT-F with  $N_h = \{33, 120\}$  and E-LUT-W in 1-tone and 12-tone cases. Moreover, non-LUT based schemes are realized with linear PA and infinite-precision arithmetic. In single tone, E-LUT-W with 9 bit wordlength does follow the OOB emission mask with non-linear PA. However, E-LUT-F with short filter follows the OOB emission mask. Although both filtering cases follow the OOB emission mask; the longer filter provides larger margin than the shorter filter.

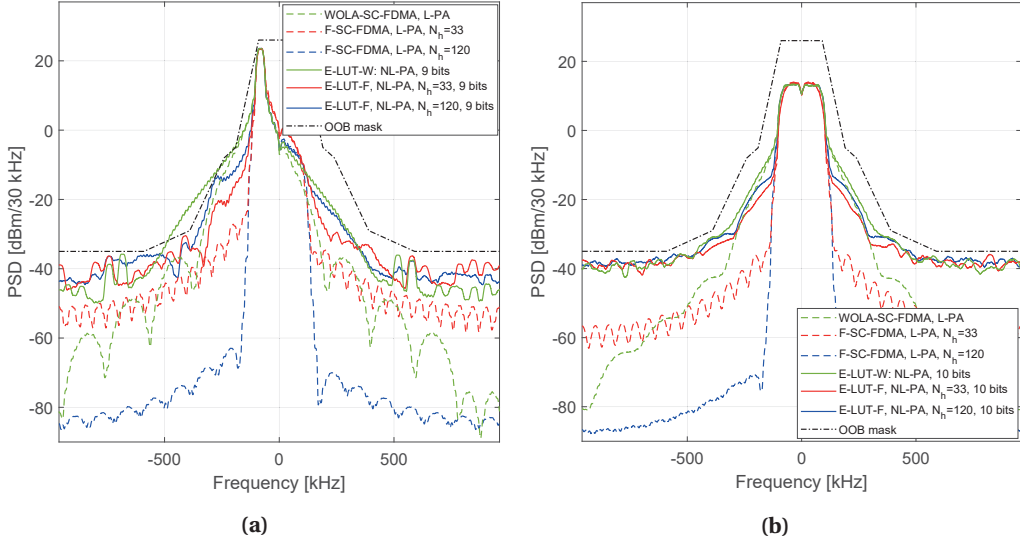


**Figure 5.11:** OOB emissions for E-LUT-W and E-LUT-F with nonlinear PA (NL-PA). (a) Single-tone with phase continuity,  $\pi/2$ -BPSK modulation and 9 bit wordlength. (b) 12-tone case with QPSK modulation and 10 bit wordlength. The transmission power is 23 dBm and 21 dBm for single-tone and 12-tone cases, respectively. Non-quantized cases with linear PA (L-PA) are shown as reference with the 3GPP emission mask [3GP18b].

## 5.5 Computational complexity analyses of LUT variants

Different LUT-OFDM variants require only additions for their implementations. Since the waveforms are stored in the memory, the memory requirement of the LUT becomes the crucial factor of the implementation. In this section, the computational complexity and the memory requirements of the LUT variants are present for NB-IoT in normal CP configuration. Here, the real addition rate is divided into the real additions needed to combine the waveform produced by the LUT ( $\alpha_s$ ) and the real additions needed to combine the overlaps between the adjacent symbol ( $\alpha_o$ ). Accordingly, the generic formula for LUT based implementations is expressed as follows:

$$\alpha = \frac{1}{n_a K} (\alpha_s + \alpha_o). \quad (5.35)$$

Nevertheless, the SC-FDMA or CP-OFDM does not employ overlap between adjacent symbol making  $\alpha_o = 0$  for these cases. In the following, the formulas for  $\alpha_o$  are found for LUT-W and LUT-F.

Considering the basic LUT implementation, the number of required additions is expressed as

$$\alpha_s^{(B)} = 2(K-1)(N_t + (n_a - 1)N_{ol}) \quad (5.36a)$$

$$\alpha_o^{(B)} = 2(n_a - 1)N_{ol}, \quad (5.36b)$$

where  $N_{ol}$  is the number of overlapping samples that is defined as follows:

$$N_{ol} = \begin{cases} 0, & \text{for LUT based SC-FDMA} \\ 2N_{EX}, & \text{for LUT-W} \\ N_h - 1, & \text{for LUT-F.} \end{cases} \quad (5.37)$$

The required memory for basic LUT implementation is expressed as

$$\epsilon_B = 2^q K (\tilde{N}_c + \dot{N}_c), \quad (5.38)$$

where  $q = 2$  for single-tone  $\pi/4$ -QPSK and  $q = 1$  otherwise.

The input sample grouping reduces the number of real additions by the factor  $G$  as follows:

$$\alpha_s^{(G)} = 2(N_G - 1)(N_t + (n_a - 1)N_{ol}) \quad (5.39a)$$

$$\alpha_o^{(G)} = 2(n_a - 1)N_{ol}. \quad (5.39b)$$

Nevertheless, the grouping increases the memory requirements by the factor  $P/G$ . Accordingly, the memory requirement is expressed as

$$\epsilon_G = 2PN_G(\tilde{N}_c + \dot{N}_c), \quad (5.40)$$

With E-LUT, the require memory units is  $2\tilde{N}_cPN_G$  fewer than the required memory units of grouping without CP extrapolation  $\epsilon_G$ . Additionally, the number of real additions is reduced as

$$\alpha_s^{(E)} = 2n_aN_c(N_G - 1) \quad (5.41a)$$

$$\alpha_o^{(E)} = 2\left((n_o - 1)N_{ol} - \left(\frac{n_a}{N_b} - 1\right)(\tilde{N}_{CP} - \dot{N}_{CP})\right), \quad (5.41b)$$

where  $N_b$  is the number symbols per slot. The reduced memory is expressed as follow:

$$\epsilon_E = 2^qPN_GN_c. \quad (5.42)$$

O-LUT reduces the number of additions required due to the overlapping processing. Therefore, the number of real additions due to the filter can be set to zero, i.e.,  $\alpha_o = 0$ . However, the drawback is the significant increase in the memory requirements. The number of required real additions is expressed as follows:

$$\alpha_s^{(o)} = 2(N_G - 1)(N_t - (\tilde{N}_{CP} - \dot{N}_{CP})). \quad (5.43)$$

Subsequently, the memory requirements are expressed as follows:

$$\epsilon_o = \epsilon_E + 2^qP'N_G(2N_{ol} - (\tilde{N}_{CP} - \dot{N}_{CP})). \quad (5.44)$$

Here, the memory requirement is expressed partly based on (5.42) because non-overlapping parts of the symbol are processed according to the E-LUT scheme. The latter terms represents memory requirements of the overlapping part.

The complexity of LUT based schemes and variants are compared with other alternative implementations for single-tone, 3-tone, 6-tone, and 12-tone allocations. These alternative schemes are SC-FDMA, WOLA-SC-FDMA, F-SC-FDMA with  $N_h = \{33, 120\}$ , FC-F-SC-FDMA, and NB-FC-F-SC-FDMA. The LUT based schemes are E-LUT-W, E-LUT-F, WOLA-SC-FDMA based O-LUT (O-LUT-W), and O-LUT-F. The transform size used for SC-FDMA is  $N = 128$ . For WOLA based schemes, the time-domain window is RC with  $N_{EX} = 5$  and  $N_w = 10$ . For FC-F-SC-FDMA and NB-FC-F-SC-FDMA, the sizes of the long transform, short transform, and low-rate OFDM are 128. The decomposition factor  $D$  is chosen to be 16, 8, 8, and 4 for single-tone, 3-tone, 6-tone, and 12-tone allocations, respectively.

Starting with memory requirements, two memory units in bit wordlength are used to represent complex coefficient. The memory requirements of the non-LUT schemes are 61 memory units

**Table 5.2:** The requirements of memory units for E-LUT-F and O-LUT-F with filter length of  $N_h = \{33, 120\}$  represented by the upper and lower numbers, respectively. Single-tone results are for  $\pi/2$ -BPSK and  $\pi/4$ -QPSK without phase continuity. The bold font represents the potentially practical memory sizes.

Subband size	Group size	Extrapolation		Overlap storing	
		BPSK	QPSK	BPSK	QPSK
1	1	<b>338</b>	<b>676</b>	<b>590</b>	<b>1684</b>
		<b>512</b>	<b>1024</b>	<b>1460</b>	<b>4816</b>
3	1	<b>1014</b>	<b>1014</b>	<b>1770</b>	<b>2526</b>
		<b>1536</b>	<b>1536</b>	<b>4380</b>	<b>7224</b>
	3	<b>1352</b>	<b>5408</b>	<b>5384</b>	<b>134432</b>
		<b>2048</b>	<b>8192</b>	<b>17216</b>	<b>493568</b>
6	1	<b>2028</b>	<b>2028</b>	<b>3450</b>	<b>5052</b>
		<b>3072</b>	<b>3072</b>	<b>8760</b>	<b>14448</b>
	3	<b>2704</b>	<b>10816</b>	<b>10768</b>	268864
		<b>4096</b>	<b>16384</b>	<b>34432</b>	987136
	6	<b>10816</b>	<b>346112</b>	268864	$0.5 \times 10^9$
		<b>16384</b>	524288	987136	$2.0 \times 10^9$
12	1	<b>4056</b>	<b>4056</b>	<b>7080</b>	<b>10104</b>
		<b>6144</b>	<b>6144</b>	<b>17520</b>	<b>28896</b>
	3	<b>5408</b>	<b>21632</b>	<b>21536</b>	537728
		<b>8192</b>	<b>32768</b>	<b>68864</b>	$2.0 \times 10^6$
	6	<b>21632</b>	692224	537728	$1.1 \times 10^9$
		<b>32768</b>	$1.0 \times 10^6$	$2.0 \times 10^6$	$4.0 \times 10^9$
	12	692224	$1.4 \times 10^9$	$1.1 \times 10^9$	$8.9 \times 10^{15}$
		$1.0 \times 10^6$	$2.1 \times 10^9$	$4.0 \times 10^9$	$0.3 \times 10^{18}$

for SC-FDMA, 71 memory units for WOLA-SC-FDMA, 63 memory units for FC-F-SC-FDMA and NB-FC-F-SC-FDMA, and 160 or 421 memory units for F-SC-FDMA with filter lengths of  $N_h = \{33, 120\}$ , respectively. These memory units are for permanent memory containing the coefficients of the split-radix IFFT implementation, frequency-domain windowing, time-domain windowing components, and filter impulse response. Table 5.2 shows the memory requirements for E-LUT-F and O-LUT-F with different allocations and group sizes using QPSK. For single-tone allocation, the indicated results are without phase continuity. The memory requirement of single-tone with phase continuity equals the corresponding case without phase continuity multiplied by 7. The basic LUT scheme is avoided due to the fact that the effect of CP extrapolation to link performance is negligible with increase in the memory requirements. This table shows significant differences in the memory usage between QPSK and BPSK. Besides, the effect of groups size appears in increasing the memory significantly considering the group size of 6 and 12. Basically, the O-LUT has an extreme memory requirement with group size of 6 and 12.

Table 5.3 shows the total memory requirements to store all of the possible subcarrier allocations in the NB-IoT device with  $G = 1$  for E-LUT-W and E-LUT-F with  $N_h = \{33, 120\}$ . E-LUT-W shows 13 % lower memory requirement than E-LUT-F scheme with  $N_h = 33$ . Considering 3GPP specifications, 3-tone allocation is allowed with four possible locations in the NB-IoT channel. Therefore, three stored waveforms for each location is required. With 6-tone allocation, 3GPP specifications allow two possible locations requiring six waveforms for each location. Considering 12-tone allocation, 12 stored waveforms are needed for the single possible location in the NB-IoT channel. For single-tone, there are 12 possible allocations. With phase continuity, con-

**Table 5.3:** The requirements of memory units for E-LUT based schemes with and without phase continuity and group size of 1. The upper numbers represent E-LUT-W and the middle and lower numbers represent E-LUT-F with filter lengths of  $N_h = \{33, 120\}$ , respectively.

Subband size	Possible allocations	Per subcarriers allocations		All subcarriers allocations	
		BPSK	QPSK	Without phase continuity	With continuity
1	12	294	588	5292	37044
		338	676	6084	42588
		512	1024	9216	64512
3	4	-	882	3528	3528
		-	1014	4056	4056
		-	1536	6144	6144
6	2	-	1764	3528	3528
		-	2028	4056	4056
		-	3072	6144	6144
12	1	-	3528	3528	3528
		-	4056	4056	4056
		-	6144	6144	6144
All allocations				15876	47628
				18252	54756
				27648	82944

jugate symmetry can be exploited to reduce the memory requirement to six stored waveforms that is multiplied by seven symbols. The single-tone without phase continuity is included to highlight the increased memory requirement.

Finally, the computational complexity of LUT based schemes are compared to non-LUT schemes in Figure 5.12. In Figure 5.12(a), it has been shown that the time-domain filtering needs significantly higher real multiplication rates compared to F-SC-FDMA scheme. The benefits of NB-FC-F-SC-FDMA are insignificant in this cases due to the small size of the long transform, i.e.,  $N = 128$ . Moreover, the LUT based schemes do not require multiplications. Nevertheless, LUT based schemes require real additions as shown in Figure 5.12(b). In general, the LUT based schemes reach significantly lower addition rates when compared to the non-LUT schemes. The O-LUT based schemes require lower real addition rates when compared to E-LUT. Moreover, O-LUT schemes does not need real additions with single-tone and 3-tone with  $G = 3$ .

## 5.6 Chapter summary

In this chapter, LUT-based implementation of enhanced OFDM (E-OFDM) schemes was proposed as an alternative to implementations requiring general multiplier units. Focusing mainly on F-OFDM and WOLA-OFDM transmitters, the waveforms provided by these schemes can be stored in the memory of the transmitter considering all of the possible modulating symbol combinations. This approach can be utilized in the implementation of NB-IoT transmitters which are standardized by 3GPP. NB-IoT uses a limited number of BPSK- or QPSK-modulated subcarriers, from one to 12. Low constellation order and low number of subcarriers encourage the use of the memory or LUT instead of the actual implementation with arithmetic operations.



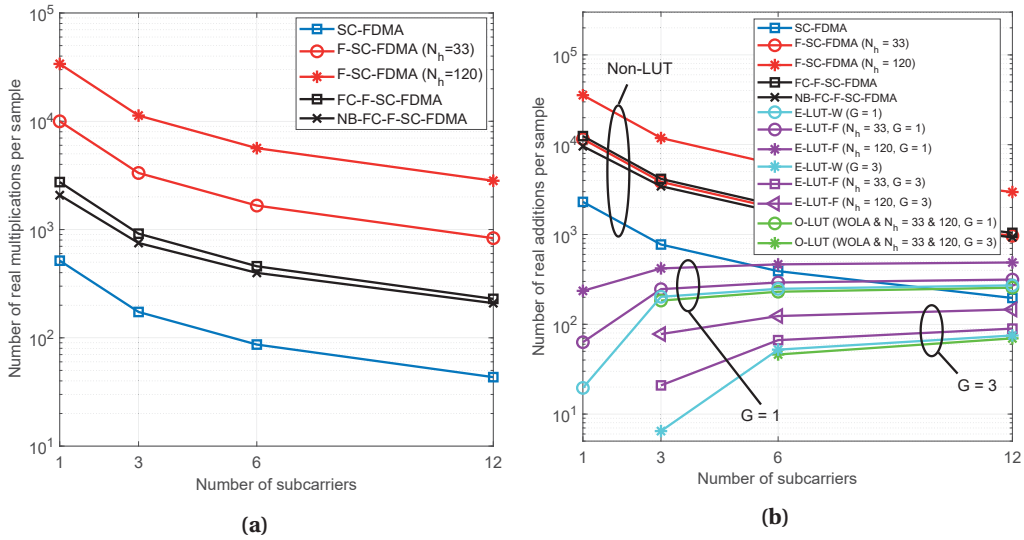


**Figure 5.12:** (a) Real multiplication rates and (b) real addition rates per transmitted samples for different SC-FDMA schemes. The real multiplication rates of E-LUT and O-LUT variants are not shown because they are zero for all configurations. The O-LUT curves of addition rates start from zero. However, these values are not shown due to the logarithmic  $y$ -scale.

The proposed LUT schemes include three enhancements, which can be combined in various ways.

The basic LUT scheme includes the subcarrier grouping to reduce the number of required real additions. With this variant, the subcarriers are arranged in groups and the waveforms for all possible combinations of the modulated symbols are saved in the memory. Nevertheless, the required memory size increases rapidly with the increase of the number of subcarriers in the group. A generalized method to arrange and fetch the stored waveform according to the symbol modulation combination was also proposed with this approach to support efficient implementation. NB-IoT is used only with the normal CP configuration which assumes varying length of CP. With CP extrapolation, the LUT size can be halved without any significant loss in the performance. In WOLA-OFDM and F-OFDM, the windowed or filtered OFDM symbols overlap in time domain. As a result, the waveform generation should perform the overlapping between the consecutive symbols requiring additions. With overlap storing, the LUT can be implemented without other operations but waveform extraction from the LUT. Table 5.2 shows that that O-LUT has realistic memory size with group size of three or less. Also in E-LUT, the group size of 6 is realistic only with BPSK modulation. Therefore, the group sizes of one and three are the useful choices for NB-IoT. Based on Figure 5.12, also additions can be completely avoided in O-LUT, when the number of active subcarriers is three or less.

Another important issue is the minimum wordlength required for the LUT contents. The waveform alternatives to be stored are computed off-line with high-precision arithmetic and then quantized to a wordlength by which the system specifications are reached. In the NB-IoT case, the minimum wordlength was found to be about 10 bits, limited by the OOB emission requirements.



## Conclusion

In this study, the waveform candidates for 5G-NR, NB-IoT, and future beyond-5G/beyond-OFDM wireless systems have been discussed with focus on their computational complexity analyses. These waveforms were compared with the basic CP-OFDM based schemes showing the additional computational complexity required to improve the spectral localization. WOLA-OFDM waveform has an enhanced spectral localization while requiring notably small additional computational complexity, as shown in Figure 2.10. Nevertheless, the OOB emissions of WOLA-OFDM are not sufficient around the active subcarriers, (see, e.g., Figure 2.5). As provided in Figure 2.8, F-OFDM enhances the spectral containment of CP-OFDM. However, fixed filter implementation lacks the flexibility needed for 5G-NR and future wireless system developments. Moreover, the required computational complexity increases exponentially with increasing filter order, as depicted in Figure 2.11. Generally, multirate filtering based waveforms provide significantly reduced OOB emissions. FBMC waveforms perform per-subcarrier filtering providing extremely low OOB emissions as shown in Figure 3.3. RB-F-OFDM is another multirate waveform that performs per-PRB filtering. However, those waveforms demand high computational complexity if the processing is based on time-domain filters or filter banks. Our studies focused on the alternative choice, fast-convolution filtering based waveforms, which are able to provide very good spectrum localization with great flexibility in frequency-domain operations, such as subband frequency shifting and adjusting the subband bandwidths. Additionally, FC based schemes are capable of flexible multimode processing with CP-OFDM, FBMC/OQAM, FMT, and single-carrier waveforms. Along with these benefits, FC based schemes show significantly reduced computational complexity compared to the corresponding time-domain filtering based schemes such as FBMC or RB-F-OFDM. This is especially the case in narrowband allocations, as indicated in Figures 3.12 and 3.13. The computational complexity per processed symbol is controlled by the overlapping factor. The overlapping factor controls also the circular interference introduced by the FC processing. With appropriate overlapping factor, the effect of the circular interference to subband localization and link performance is insignificant.

One answer to the research question stated in the Introduction is to decompose the FC using the CC decomposition technique. D-FC has shown identical outputs to the corresponding basic FC implementation. This was proven through mathematical analyses and simulations. The generic implementation of D-FC requires insignificant increase in the computational complexity compared to the direct implementation of FC. Generic implementation of D-FC

is useful for implementations operating at high sampling rates with long transform sizes, as it helps to parallelize the long transform processing. It can also be configured easily for different transform sizes. The special narrowband configuration of D-FC showed significant (up to 40 % as in Figure 4.8) reduction in the computational complexity compared to the direct multirate FC structure when the active signal bandwidth is relatively small compared to the sampling rate. Moreover, the idea of NB-FC was extended to consider pruning of CP-OFDM with only few active subcarriers. It was shown Figure 4.11 that dynamically pruned CP-OFDM requires only about 20 % of the multiplications of the plain CP-OFDM in such cases. In the narrowband LTE scenarios of Figure 4.12, the symbol synchronized NB-FC-F-OFDM practically reaches the complexity of plain CP-OFDM in terms of multiplication rate. The D-FC was also beneficial with uniformly distributed non-overlapping subbands. However, this scenario lacks the flexibility of the plain FC scheme. Nevertheless, it can achieve up to 35 % reduction in the computational complexity when compared to the corresponding FC implementations with two times oversampling (c.f. Figure 4.9). Moreover, the decomposition was employed to reduce the computational complexity of the short transforms and low-rate OFDM processing in case of symbol-synchronized discontinuous FC-F-OFDM receiver. The complexity reduction of the simplified cases in the narrowband case is insignificant compared to the symbol synchronized FC-F-OFDM without simplification. In the wideband LTE scenario of Figure 4.13 with overlapping factor of 0.5, the simplified implementation requires up to 15 % lower multiplication rate than the original implementation.

A complementary answer to the research question is that look-up table based implementations turned out to be very efficient for narrowband multicarrier devices with very low number of subcarriers. Extremely low-complexity schemes using LUT based approach were proposed for NB-IoT transmitters. These schemes allow to imitate the implementation of extremely complex operations such as FFT/IFFT and filtering in ultra low-complexity devices. With LUT implementation, the multiplications can be completely avoided while generating filtering based waveforms in real time. Besides, the number of real additions is reduced significantly compared to CP-OFDM. Nevertheless, the number of memory elements required by the LUT based approaches varies according to used LUT variant, modulation, number of subcarriers, and filter impulse response length. Moreover, an effective technique was given for allocating and fetching the waveform vectors in the memory. NB-IoT specifications determine that the CP length of the first symbol is longer than the others. It was shown that, by extrapolating the samples of the longer CP from the samples of the shorter CP, the memory requirements could be approximately halved. In these LUT based schemes, the waveforms produced by the adjacent symbols have to be overlapped and added in order to provide the overall waveform. With O-LUT, filtering based or WOLA based waveforms can be produced without any additions. Nevertheless, the memory requirements of this variant increase dramatically as the number of subcarriers and the modulation order of input symbols increases. Therefore, this variant is useful in very narrow allocations, that is, in single-tone and three-tone cases of NB-IoT. The effects of quantization on LUT based implementations were also investigated considering OOB emission, in-band emission, and EVM requirements of the 3GPP specifications for NB-IoT uplink transmitter. It has been shown that with only 10 bit wordlength the requirements can be met.

The author believes that the achieved savings in the computational complexity make the investigated schemes worthwhile for further studies towards hardware implementations. However, it should be noted that very basic complexity metrics were used in this study, and the savings in practical implementation depend greatly on the used hardware technology/platform.

For future work, D-FC based implementations can be extended to non-power-of-two trans-

form lengths. The reduction of the transform sizes with the decomposition could provide even further savings in the implementations. Besides, generic form of NB-FC schemes can be investigated considering input/output pruning with more than one input/output. This idea could be combined with Goertzel algorithm which is used for computing DFTs with few inputs. Furthermore, the condition for the decomposition factor with respect to interpolation/decimation factor could be relaxed. This case can be examined with oversampled/downsampled FC scenarios. Concerning the LUT approach, the study in Chapter 5 could be extended to include optimized finite-precision design of the filtered waveforms to minimize the LUT wordlength. Also practical implementation issues like processing delays and power consumption need further investigation. Moreover, this extended study could find the trade-offs between the memory size and power consumption. Besides, full digital baseband processing for NB-IoT devices meeting the 3GPP specifications could be implemented using the LUT approach for the transmitter and the NB-FC approach for low-complexity receiver.



## A

# The Implementation of the Complex Multiplication and Complex Addition

## A.1 The multiplication of two complex numbers

Assuming a complex number  $x$  that is defined with respect to the real component and imaginary component as  $x_1 + jx_Q$ , where  $j = \sqrt{-1}$ . This complex number is multiplied by  $y = y_1 + jy_Q$  resulting in  $w = w_1 + jw_Q$ . The multiplication in complex domain is expressed as follows:

$$w = xy = (x_1 + jx_Q)(y_1 + jy_Q) \quad (\text{A.1a})$$

$$w_1 = (x_1y_1 - x_Qy_Q) \quad (\text{A.1b})$$

$$w_Q = (x_1y_Q + x_Qy_1). \quad (\text{A.1c})$$

Hence, the multiplication of two complex numbers requires 4 real multiplications and 2 real additions. If  $y_1 = y_Q$ , then 2 real multiplications and 2 real additions are sufficient. This case occurs for  $W_8^{(\pm 1)}$  and  $W_8^{(\pm 3)}$ . If  $y$  is fixed, then 3 components could be stored as follows:

$$y_1 \quad (\text{A.2a})$$

$$a = y_1 + y_Q \quad (\text{A.2b})$$

$$b = y_1 - y_Q. \quad (\text{A.2c})$$

Consequently, the complex multiplication is preformed as follows:

$$w_1 = ax_1 + y_1(x_1 - x_Q) \quad (\text{A.3a})$$

$$w_R = bx_Q - y_1(x_1 - x_Q). \quad (\text{A.3b})$$

Accordingly, the multiplication of the two complex numbers while knowing one of them requires 3 real multiplications and 3 real additions.

## A.2 Complex multiplication of complex sequence by set of twiddle factor

Assuming that a complex sequence  $x[n]$  is multiplied by set of twiddle factors  $W_N^{nk_0}$ , where  $n = 0, 1, \dots, L-1$ ,  $k_0$  is constant integer, and  $N$  is power-of-two number. For  $n = iN/4C$ , where  $i$  is integer and  $C = \gcd(k_0, N)$ , the multiplication by  $W_N^{nk_0}$  is trivial, i.e.,  $W_N^{nk_0} = \{\pm 1, \pm j\}$ . For  $n = (2i+1)N/8C$ , the multiplication by  $W_N^{nk_0}$  requires 2 real multiplications and 2 real additions

because  $W_N^{nk_0} = \{W_8^{(\pm 1)}, W_8^{(\pm 3)}\}$ . In the other cases, the multiplication by  $W_N^{nk_0}$  is performed with 3 real multiplications and 3 real additions. Therefore, the generic formula to multiply the complex sequence by set of twiddle factors is found as

$$\begin{aligned}\sigma_{\text{TW}}[N, L, k_0] &= 3 \left( L - \left\lceil \frac{L}{\left(\frac{N}{8C}\right)} \right\rceil \right) + 2 \left( \left\lceil \frac{L}{\left(\frac{N}{8C}\right)} \right\rceil - \left\lceil \frac{L}{\left(\frac{N}{4C}\right)} \right\rceil \right) \\ \sigma_{\text{TW}}[N, L, k_0] &= 3L - \left\lceil \frac{8CL}{N} \right\rceil - 2 \left\lceil \frac{4CL}{N} \right\rceil,\end{aligned}\tag{A.4}$$

for  $N/C \neq \{1, 2, 4\}$ .

### A.3 Odd-DFT implementations

Assuming that the inputs of FFT of size  $N$  are multiplied by set of twiddle factor  $W_N^{0.5n}$ , where  $n = 0, 1, \dots, N-1$  is the time index. This implementation is expressed as

$$X[k] = \sum_{n=0}^{N-1} x[n] W_N^{0.5n} W_N^{nk}, \tag{A.5}$$

where  $k = 0, 1, \dots, N-1$  is the frequency index. Using the decimation-in-frequency, the implementation in this case can be expressed as

$$X[2k'] = \sum_{n'=0}^{\frac{N}{2}-1} \left( x[n'] - jx\left[n' + \frac{N}{2}\right] \right) W_N^{0.5n'} W_{\frac{N}{2}}^{n'k'} \tag{A.6a}$$

$$X[2k' + 1] = \sum_{n'=0}^{\frac{N}{2}-1} \left( x[n'] + jx\left[n' + \frac{N}{2}\right] \right) W_N^{1.5n'} W_{\frac{N}{2}}^{n'k'}, \tag{A.6b}$$

where  $k' = 0, 1, \dots, N/2 - 1$  is the decimated frequency index. As a result, the odd-DFT is implemented with two FFTs of size  $N/2$ . The inputs of the DFTs are  $W_N^{0.5}$  and  $W_N^{1.5}$  as shown in Figure A.1(a). This modified implementation requires reduced computational complexity as follows:

$$\mu_{\text{ODD}} = N \log_2 N - N \tag{A.7a}$$

$$\alpha_{\text{ODD}} = 3N \log_2 N - N. \tag{A.7b}$$

The other case of the odd-DFT is FFT with output multiplied by  $W_N^{0.5k}$  that is expressed as follows:

$$X[k] = W_N^{0.5k} \sum_{n=0}^{N-1} x[n] W_N^{nk}, \tag{A.8}$$

This case could be decomposed using decimation-in-time as follows:

$$X[k'] = W_N^{0.5k'} \sum_{n'=0}^{\frac{N}{2}-1} x[2n'] W_{\frac{N}{2}}^{n'k'} + W_N^{1.5k'} \sum_{n'=0}^{\frac{N}{2}-1} x[2n'+1] W_{\frac{N}{2}}^{n'k'} \tag{A.9a}$$

$$X\left[k' + \frac{N}{2}\right] = j \left( -W_N^{0.5k'} \sum_{n'=0}^{\frac{N}{2}-1} x[2n'] W_{\frac{N}{2}}^{n'k'} + W_N^{1.5k'} \sum_{n'=0}^{\frac{N}{2}-1} x[2n'+1] W_{\frac{N}{2}}^{n'k'} \right). \tag{A.9b}$$

As a result, the implementation can be reduced to two DFTs of size  $N/2$  with two sets of twiddle factors as shown in Figure A.1(b). The reduced computational complexity can be simply computed using the formula in (A.7).

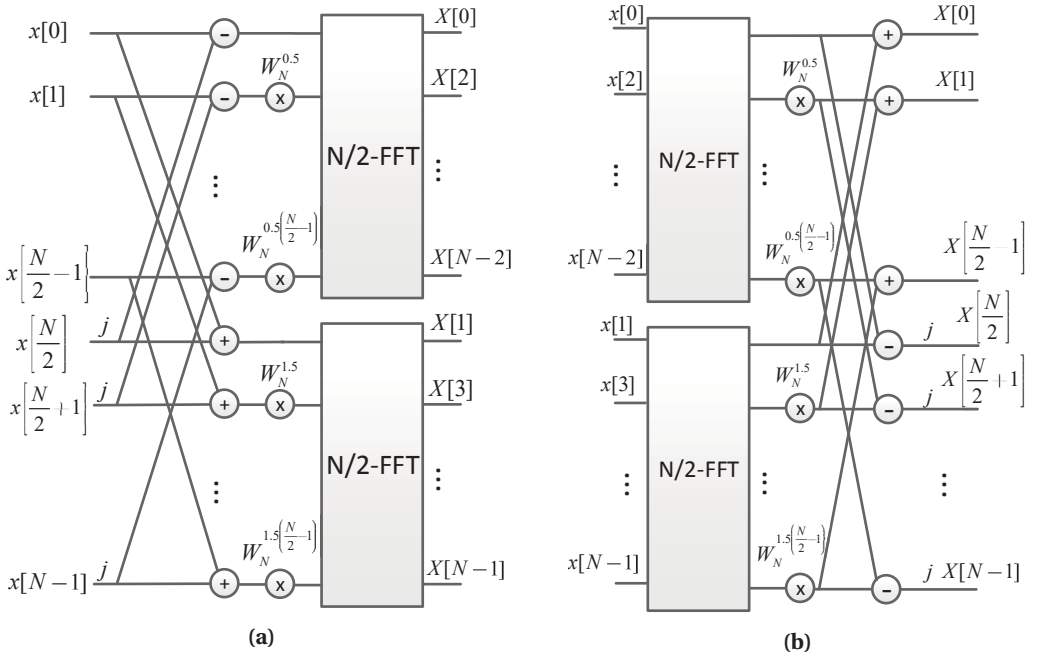


**Figure A.1:** The implementation of modified odd-DFT with (a)  $0.5n$  frequency shift and (b)  $0.5k$  time shift.

#### A.4 DFT pruning with single input/output

Assuming that a single input is fed to DFT of size  $N$ . The output of the DFT is expressed as

$$X[k] = x W_N^{n_0 k}, \quad (\text{A.10})$$

where  $n_0 \in \{0, 1, \dots, N-1\}$  is the index of the DFT input,  $k = 0, 1, \dots, L-1$  is the index of the DFT outputs of length  $L$  and  $x = x_I + j x_Q$  is the single DFT input. It is possible to reduce the number of multiplications by removing the redundant trigonometric components. For non-trivial 8th roots of unity, a unified expression for the multiplications can be expressed as

$$X \left[ \frac{N(2i+1)}{8C} \right] = (-j)^i \left( \sqrt{0.5} (x_I + x_Q) - j \sqrt{0.5} (x_I - x_Q) \right), \quad (\text{A.11})$$

where  $i$  is an integer and  $C = \gcd(N, n_0)$ . Therefore, the multiplications corresponding to  $k = N(2i+1)/8C$  requires 2 real multiplications and 2 real additions. Considering the multiplications by non-8th roots of unity, the real and imaginary components of the twiddle factors are repeated at every  $iN/4C \pm a$ , where  $a$  is an integer. Therefore, the complex multiplications can be performed as follows:

$$X \left[ i \frac{N}{4C} \pm a \right] = (-j)^i \left( \left( x_I \cos \left( \frac{2\pi a}{N} \right) \mp x_Q \sin \left( \frac{2\pi a}{N} \right) \right) + j \left( x_I \sin \left( \frac{2\pi a}{N} \right) \pm x_Q \cos \left( \frac{2\pi a}{N} \right) \right) \right). \quad (\text{A.12})$$

Accordingly, 4 real multiplications and 4 real additions are needed for DFT outputs corresponding to  $k = (iN/4C) \pm a$ . Therefore, the number of real multiplication to perform (A.11) is computed as  $N/2C - 1$ . This approach is feasible if the number of redundant components are at least two for each entry. In such cases, 3 real multiplications and 3 real additions should be used

instead. For single output pruning, the same approach is used requiring similar computational complexity for real multiplications.



# Bibliography

- [3GP04] *Technical Specification Group Radio Access Network; Feasibility Study for Orthogonal Frequency Division Multiplexing (OFDM) for UTRAN enhancement (Release 6)*, 3GPP, document TR 25.893 V6.0.0, Jun. 2004.
- [3GP18a] *Technical Specification Group Radio Access Network; Evolved Universal Terrestrial Radio Access (E-UTRA); User Equipment (UE) radio transmission and reception (Release 15)*, 3GPP, document TR 36.101 V15.0.0, Mar. 2018.
- [3GP18b] *Technical Specification Group Radio Access Network; Evolved Universal Terrestrial Radio Access (E-UTRA); Physical channels and modulation (Release 14)*, 3GPP, document TR 36.211 V14.0.0, Jun. 2018.
- [ADB17] N. Agrawal, S. J. Darak, and F. Bader, “Reconfigurable filtered OFDM waveform for next generation air-to-ground communications,” in *Proc. Digital Avionics Systems Conference (DASC)*, Sep. 2017, pp. 1–7.
- [AJM15] J. Abdoli, M. Jia, and J. Ma, “Filtered OFDM: A new waveform for future wireless systems,” in *Proc. International Workshop on Signal Processing Advances in Wireless Communications (SPAWC)*, Jun. 2015, pp. 66–70.
- [Arm99] J. Armstrong, “Analysis of new and existing methods of reducing intercarrier interference due to carrier frequency offset in OFDM,” *IEEE Transactions on Communications*, vol. 47, no. 3, pp. 365–369, Mar. 1999.
- [Bal81] R. Balian, “Un principe d’incertitude fort en théorie du signal ou en mécanique quantique,” *Comptes-Rendus de l’Académie des Sciences (Paris), Serie II*, vol. 292, no. 20, pp. 1357–1362, 1981.
- [BCB78] G. Bonnerot, M. Coudreuse, and M. Bellanger, “Digital processing techniques in the 60 channel transmultiplexer,” *IEEE Transactions on Communications*, vol. 26, no. 5, pp. 698–706, May 1978.
- [BCS05a] S. Brandes, I. Cosovic, and M. Schnell, “Reduction of out-of-band radiation in OFDM based overlay systems,” in *Proc. International Symposium on New Frontiers in Dynamic Spectrum Access Networks (DySPAN)*, Nov. 2005, pp. 662–665.

- [BCS05b] S. Brandes, I. Cosovic, and M. Schnell, "Sidelobe suppression in OFDM systems by insertion of cancellation carriers," in *Proc. Vehicular Technology Conference (VTC Fall)*, vol. 1, Sep. 2005, pp. 152–156.
- [BD74] M. Bellanger and J. Daguët, "TDM-FDM transmultiplexer: Digital polyphase and FFT," *IEEE Transactions on Communications*, vol. 22, no. 9, pp. 1199–1205, Sep. 1974.
- [BDH99] H. Bölcskei, P. Duhamel, and R. Hleiss, "Design of pulse shaping OFDM/OQAM systems for high data-rate transmission over wireless channels," in *Proc. International Conference on Communications*, vol. 1, Jun. 1999, pp. 559–564.
- [BDH03] H. Bölcskei, P. Duhamel, and R. Hleiss, "Orthogonalization of OFDM/OQAM pulse shaping filters using the discrete zak transform," *Signal Processing*, vol. 83, no. 7, pp. 1379 – 1391, 2003.
- [BDN14a] V. Berg, J. Doré, and D. Noguët, "A flexible FS-FBMC receiver for dynamic access in the TVWS," in *2014 9th International Conference on Cognitive Radio Oriented Wireless Networks and Communications (CROWNCOM)*, Jun. 2014, pp. 285–290.
- [BDN14b] V. Berg, J.-B. Doré, and D. Noguët, "A flexible radio transceiver for TVWS based on FBMC," *Microprocess. Microsyst.*, vol. 38, no. 8, pp. 743–753, Nov. 2014.
- [Bel01] M. G. Bellanger, "Specification and design of a prototype filter for filter bank based multicarrier transmission," in *Proc. International Conference on Acoustics, Speech, and Signal Processing. Proceedings (ICASSP)*, vol. 4, May 2001, pp. 2417–2420.
- [Bel10] M. Bellanger, "FBMC physical layer: A primer," Physical layer for dynamic spectrum access and cognitive radio (PHYDYAS) project, Tech. Rep., Jun. 2010.
- [Bel12a] M. Bellanger, "FS-FBMC: A flexible robust scheme for efficient multicarrier broadband wireless access," in *2012 IEEE Globecom Workshops*, Dec 2012, pp. 192–196.
- [Bel12b] M. Bellanger, "FS-FBMC: An alternative scheme for filter bank based multicarrier transmission," in *2012 5th International Symposium on Communications, Control and Signal Processing*, May 2012, pp. 1–4.
- [BKW<sup>+</sup>17] J. Bazzi, K. Kusume, P. Weitkemper, K. Takeda, and A. Benjebbour, "Transparent spectral confinement approach for 5G," in *Proc. European Conference on Networks and Communications (EuCNC)*, Jun. 2017, pp. 1–5.
- [Bla10] R. E. Blahut, *Fast Algorithms and Multidimensional Convolutions*. Cambridge University Press, jun. 2010.
- [BMF99] M.-L. Boucheret, I. Mortensen, and H. Favaro, "Fast convolution filter banks for satellite payloads with on-board processing," *IEEE Journal on Selected Areas in Communications*, vol. 17, no. 2, pp. 238–248, Feb. 1999.
- [Bon86] C. Boncelet, "A rearranged DFT algorithm requiring  $N^2/6$  multiplications," *IEEE Transactions on Acoustics, Speech, and Signal Processing*, vol. 34, no. 6, pp. 1658–1659, Dec. 1986.
- [Bor06] M. Borgerding, "Turning overlap-save into a multiband mixing, downsampling filter bank," *IEEE Signal Processing Magazine*, vol. 23, no. 2, pp. 158–161, Mar. 2006.

- [BSRN11] L. G. Baltar, F. Schaich, M. Renfors, and J. A. Nossek, "Computational complexity analysis of advanced physical layers based on multicarrier modulation," in *Proc. Future Network Mobile Summit*, Jun. 2011, pp. 1–8.
- [BT07] N. C. Beaulieu and P. Tan, "On the effects of receiver windowing on OFDM performance in the presence of carrier frequency offset," *IEEE Transactions on Wireless Communications*, vol. 6, no. 1, pp. 202–209, Jan. 2007.
- [CBS06] I. Cosovic, S. Brandes, and M. Schnell, "Subcarrier weighting: a method for sidelobe suppression in OFDM systems," *IEEE Communications Letters*, vol. 10, no. 6, pp. 444–446, Jun. 2006.
- [CC97] H. H. Chen and X. D. Cai, "Waveform optimization for OQAM-OFDM systems by using nonlinear programming algorithms," in *Proc. Vehicular Technology Conference (VTC)*, vol. 3, May 1997, pp. 1385–1389.
- [CEO99] G. Cherubini, E. Eleftheriou, and S. Olcer, "Filtered multitone modulation for VDSL," in *Proc. Global Telecommunications Conference (GLOBECOM)*, vol. 2, Dec. 1999, pp. 1139–1144.
- [cGD17] Ç. Göken and O. Dizdar, "Performance of edge windowing for OFDM under non-linear power amplifier effects," in *Proc. Military Communications Conference (MILCOM)*, Oct. 2017, pp. 219–224.
- [Cha66] R. W. Chang, "Synthesis of band-limited orthogonal signals for multichannel data transmission," *The Bell System Technical Journal*, vol. 45, no. 10, pp. 1775–1796, Dec. 1966.
- [CHGH16] X. Cheng, Y. He, B. Ge, and C. He, "A filtered OFDM using FIR filter based on window function method," in *Proc. Vehicular Technology Conference (VTC Spring)*, May 2016, pp. 1–5.
- [CHW<sup>+</sup>17] J. Chen, K. Hu, Q. Wang, Y. Sun, Z. Shi, and S. He, "Narrowband internet of things: Implementations and applications," *IEEE Internet of Things Journal*, vol. 4, no. 6, pp. 2309–2314, Dec. 2017.
- [CM06] I. Cosovic and T. Mazzoni, "Suppression of sidelobes in OFDM systems by multiple-choice sequences," *European Transactions on Telecommunications*, vol. 17, no. 6, pp. 623–630, 11 2006.
- [CT65] J. Cooley and J. Tukey, "An algorithm for the machine calculation of complex Fourier series," *Mathematics of Computation*, vol. 19, no. 90, pp. 297–301, 1965.
- [Cve95] Z. Cvetković, "Oversampled modulated filter banks and tight Gabor frames in  $l^2(\mathbf{Z})$ ," in *Proc. International Conference on Acoustics, Speech, and Signal Processing (ICASSP)*, vol. 2, May 1995, pp. 1456–1459.
- [DGD<sup>+</sup>17] D. Demmer, R. Gerzaguet, J. Doré, D. Le Ruyet, and D. Ktésas, "Block-filtered OFDM: A novel waveform for future wireless technologies," in *Proc. International Conference on Communications (ICC)*, May 2017, pp. 1–6.
- [DH84] P. Duhamel and H. Hollmann, "'Split radix' FFT algorithm," *Electronics Letters*, vol. 20, no. 1, pp. 14–16, Jan. 1984.

- [DH85] P. Duhamel and H. Hollmann, "Implementation of "Split-radix" FFT algorithms for complex, real, and real symmetric data," in *Proc. International Conference on Acoustics, Speech, and Signal Processing (ICASSP)*, vol. 10, Apr. 1985, pp. 784–787.
- [DPS14] E. Dahlman, S. Parkvall, and J. Sköld, *4G: LTE/LTE-Advanced for Mobile Broadband (Second Edition)*. Oxford: Academic Press, 2014.
- [DPS18] E. Dahlman, S. Parkvall, and J. Sköld, *5G NR: The Next Generation Wireless Access Technology*. Oxford: Academic Press, 2018.
- [EPGA16] M. Elkourdi, B. Peköz, E. Güvenkaya, and H. Arslan, "Waveform design principles for 5G and beyond," in *Proc. Annual Wireless and Microwave Technology Conference (WAMICON)*, Apr. 2016, pp. 1–6.
- [ESSA09] M. S. El-Saadany, A. F. Shalash, and M. Abdallah, "Revisiting active cancellation carriers for shaping the spectrum of OFDM-based cognitive radios," in *Proc. Sarnoff Symposium*, Mar. 2009, pp. 1–5.
- [Fau00] M. Faulkner, "The effect of filtering on the performance of OFDM systems," *IEEE Transactions on Vehicular Technology*, vol. 49, no. 5, pp. 1877–1884, Sep. 2000.
- [FBGY10] B. Farhang-Boroujeny and C. (George) Yuen, "Cosine modulated and offset QAM filter bank multicarrier techniques: A continuous-time prospect," *EURASIP Journal on Advances in Signal Processing*, vol. 2010, no. 1, p. 165654, Feb. 2010.
- [GA96] M. Gudmundson and P. Anderson, "Adjacent channel interference in an OFDM system," in *Proc. Vehicular Technology Conference (VTC)*, vol. 2, Apr. 1996, pp. 918–922.
- [GBB<sup>+</sup>17] R. Gerzaguet, N. Bartzoudis, L. G. Baltar, V. Berg, J.-B. Doré, D. Kténas, O. Font-Bach, X. Mestre, M. Payaró, M. Färber, and K. Roth, "The 5G candidate waveform race: A comparison of complexity and performance," *EURASIP Journal on Wireless Communications and Networking*, vol. 2017, no. 1, p. 13, Jan. 2017.
- [GL95] P. Guinand and J. Lodge, "Optimal pulse shape design for OFDM transmission with few subcarriers," in *Proceedings 1995 Canadian Conference on Electrical and Computer Engineering*, vol. 1, Sep. 1995, pp. 17–19.
- [GMD<sup>+</sup>17] R. Gerzaguet, Y. Medjahdi, D. Demmer, R. Zayani, J. Doré, H. Shaiek, and D. Roviras, "Comparison of promising candidate waveforms for 5G: WOLA-OFDM versus BF-OFDM," in *Proc. International Symposium on Wireless Communication Systems (ISWCS)*, Aug. 2017, pp. 355–359.
- [GWT<sup>+</sup>17] P. Guan, D. Wu, T. Tian, J. Zhou, X. Zhang, L. Gu, A. Benjebbour, M. Iwabuchi, and Y. Kishiyama, "5G field trials: OFDM-based waveforms and mixed numerologies," *IEEE Journal on Selected Areas in Communications*, vol. 35, no. 6, pp. 1234–1243, Jun. 2017.
- [HBL<sup>+</sup>14] W. Hong, K. Baek, Y. Lee, Y. Kim, and S. Ko, "Study and prototyping of practically large-scale mmwave antenna systems for 5G cellular devices," *IEEE Communications Magazine*, vol. 52, no. 9, pp. 63–69, Sep. 2014.
- [Hir80] B. Hirosaki, "An analysis of automatic equalizers for orthogonally multiplexed QAM systems," *IEEE Transactions on Communications*, vol. 28, no. 1, pp. 73–83, Jan. 1980.

- [HMK<sup>+</sup>17] D. Han, J. Moon, D. Kim, S. Chung, and Y. H. Lee, "Combined subband-subcarrier spectral shaping in multi-carrier modulation under the excess frame length constraint," *IEEE Journal on Selected Areas in Communications*, vol. 35, no. 6, pp. 1339–1352, Jun. 2017.
- [KB13] P. Kryszkiewicz and H. Bogucka, "Out-of-band power reduction in NC-OFDM with optimized cancellation carriers selection," *IEEE Communications Letters*, vol. 17, no. 10, pp. 1901–1904, Oct. 2013.
- [KLS14] J. Karlsson, J. Li, and P. Stoica, "Filter design with hard spectral constraints," in *Proc. European Signal Processing Conference (EUSIPCO)*, Sep. 2014, pp. 391–395.
- [LBY14] J. Li, E. Bala, and R. Yang, "Resource block filtered-OFDM for future spectrally agile and power efficient systems," *Physical Communication*, vol. 11, pp. 36 – 55, 2014, radio Access Beyond OFDM(A).
- [LGR13] A. E. Loulou, S. A. Gorgani, and M. Renfors, "Enhanced OFDM techniques for fragmented spectrum use," in *Proc. Future Network Mobile Summit*, Jul. 2013, pp. 1–10.
- [LKBY13] J. Li, K. Kearney, E. Bala, and R. Yang, "A resource block based filtered OFDM scheme and performance comparison," in *Proc. International Conference on Telecommunications (ICT)*, May 2013, pp. 1–5.
- [LLJ<sup>+</sup>15] L. B. Le, V. Lau, E. Jorswieck, N.-D. Dao, A. Haghighat, D. I. Kim, and T. Le-Ngoc, "Enabling 5G mobile wireless technologies," *EURASIP Journal on Wireless Communications and Networking*, vol. 2015, no. 1, p. 218, Sep. 2015.
- [low85] F. low, "Complete sets of wave packets," *A Passion for Physics - Essay in Honor of Geoffrey Chew, C. DeTar, Ed. Singapore: world Scientific*, vol. 292, pp. 17–22, Jun. 1985.
- [LPP<sup>+</sup>19] T. Levanen, J. Pirskanen, K. Pajukoski, M. Renfors, and M. Valkama, "Transparent Tx and Rx waveform processing for 5G new radio mobile communications," *IEEE Wireless Communications*, vol. 26, no. 1, pp. 128–136, Feb. 2019.
- [LR13] A. Loulou and M. Renfors, "Effective schemes for OFDM sidelobe control in fragmented spectrum use," in *Proc. International Symposium on Personal, Indoor, and Mobile Radio Communications (PIMRC)*, Sep. 2013, pp. 471–475.
- [LR15] A. Loulou and M. Renfors, "Enhanced OFDM for fragmented spectrum use in 5G systems," *Transactions on Emerging Telecommunications Technologies*, vol. 26, no. 1, pp. 31–45, 2015.
- [LSH<sup>+</sup>17] S. Lien, S. Shieh, Y. Huang, B. Su, Y. Hsu, and H. Wei, "5G new radio: Waveform, frame structure, multiple access, and initial access," *IEEE Communications Magazine*, vol. 55, no. 6, pp. 64–71, Jun. 2017.
- [LYKL<sup>+</sup>19] A. Loulou, J. Yli-Kaakinen, T. A. Levanen, V. K. Lehtinen, F. Schaich, T. Wild, M. K. Renfors, and M. Valkama, "Look-Up table based implementation of Ultra-Low complexity narrowband OFDM transmitters," in *2019 16th International Symposium on Wireless Communication Systems (ISWCS) (ISWCS 2019)*, Oulu, Finland, Aug. 2019.

- [LYL<sup>+</sup>19] A. Loulou, J. Yli-Kaakinen, T. Levanen, V. Lehtinen, F. Schaich, T. Wild, M. Renfors, and M. Valkama, "Multiplierless filtered-OFDM transmitter for narrowband IoT devices," *IEEE Internet of Things Journal*, May 2019.
- [LYR17] A. Loulou, J. Yli-Kaakinen, and M. Renfors, "Efficient fast-convolution based implementation of 5G waveform processing using circular convolution decomposition," in *Proc. International Conference on Communications (ICC)*, May 2017, pp. 1–7.
- [LYR19] A. Loulou, J. Yli-Kaakinen, and M. Renfors, "Advanced low-complexity multicarrier schemes using fast-convolution processing and circular convolution decomposition," *IEEE Transactions on Signal Processing*, vol. 67, no. 9, pp. 2304–2319, May 2019.
- [MA08a] H. A. Mahmoud and H. Arslan, "Sidelobe suppression in OFDM-based spectrum sharing systems using adaptive symbol transition," *IEEE Communications Letters*, vol. 12, no. 2, pp. 133–135, Feb. 2008.
- [MA08b] H. A. Mahmoud and H. Arslan, "Spectrum shaping of OFDM-based cognitive radio signals," in *Proc. Radio and Wireless Symposium (RWS)*, Jan. 2008, pp. 113–116.
- [MAK13] K. Maliatsos, A. Adamis, and A. G. Kanatas, "Interference versus filtering distortion trade-offs in OFDM-based cognitive radios," *Transactions on Emerging Telecommunications Technologies*, vol. 24, no. 7-8, pp. 692–708, 2013.
- [MK97] S. Muramatsu and H. Kiya, "Extended overlap-add and -save methods for multirate signal processing," *IEEE Transactions on Signal Processing*, vol. 45, no. 9, pp. 2376–2380, Sep. 1997.
- [MLT<sup>+</sup>18] Y. Miao, W. Li, D. Tian, M. S. Hossain, and M. F. Alhamid, "Narrowband internet of things: Simulation and modeling," *IEEE Internet of Things Journal*, vol. 5, no. 4, pp. 2304–2314, Aug. 2018.
- [MTB12] D. Mattera, M. Tanda, and M. Bellanger, "Frequency-spreading implementation of OFDM/OQAM systems," in *2012 International Symposium on Wireless Communication Systems (ISWCS)*, Aug. 2012, pp. 176–180.
- [Mur94] H. Murakami, "Real-valued decimation-in-time and decimation-in-frequency algorithms," *IEEE Transactions on Circuits and Systems II: Analog and Digital Signal Processing*, vol. 41, no. 12, pp. 808–816, Dec. 1994.
- [Mus96] C. Muschallik, "Improving an OFDM reception using an adaptive Nyquist windowing," *IEEE Transactions on Consumer Electronics*, vol. 42, no. 3, pp. 259–269, Aug. 1996.
- [MW01] S. H. Muller-Weinfurtner, "Optimum Nyquist windowing in OFDM receivers," *IEEE Transactions on Communications*, vol. 49, no. 3, pp. 417–420, Mar. 2001.
- [MZSR17] Y. Medjahdi, R. Zayani, H. Shaïek, and D. Roviras, "WOLA processing: A useful tool for windowed waveforms in 5G with relaxed synchronicity," in *Proc. International Conference on Communications Workshops (ICC Workshops)*, May 2017, pp. 393–398.
- [NGB11] D. Nogu  t, M. Gautier, and V. Berg, "Advances in opportunistic radio technologies for TVWS," *EURASIP Journal on Wireless Communications and Networking*, vol. 2011, no. 1, p. 170, Nov. 2011.



- [NNB18] J. Nadal, C. A. Nour, and A. Baghdadi, "Novel UF-OFDM transmitter: Significant complexity reduction without signal approximation," *IEEE Transactions on Vehicular Technology*, vol. 67, no. 3, pp. 2141–2154, Mar. 2018.
- [OUWT18] T. Okano, M. Umehira, X. Wang, and S. Takeda, "Overlap-windowed-DFTs-OFDM with overlap FFT filter-bank for flexible uplink access in 5G and beyond," in *Proc. Vehicular Technology Conference (VTC-Fall)*, Aug. 2018, pp. 1–6.
- [PL96] S.-C. Pei and T.-L. Luo, "Split-radix generalized fast Fourier transform," *Signal Processing*, vol. 54, no. 2, pp. 137 – 151, 1996.
- [PP19] R. Pitaval and B. M. Popović, "Filtered-prefix OFDM," *IEEE Communications Letters*, vol. 23, no. 1, pp. 28–31, Jan. 2019.
- [PRWM08] S. Pagadarai, R. Rajbanshi, A. M. Wyglinski, and G. J. Minden, "Sidelobe suppression for OFDM-based cognitive radios using constellation expansion," in *Proc. Wireless Communications and Networking Conference*, Mar. 2008, pp. 888–893.
- [PWR08] S. Pagadarai, A. M. Wyglinski, and R. Rajbanshi, "A sub-optimal sidelobe suppression technique for OFDM-based cognitive radios," in *Proc. Military Communications Conference (MILCOM)*, Nov. 2008, pp. 1–6.
- [QWJ10] D. Qu, Z. Wang, and T. Jiang, "Extended active interference cancellation for sidelobe suppression in cognitive radio OFDM systems with cyclic prefix," *IEEE Transactions on Vehicular Technology*, vol. 59, no. 4, pp. 1689–1695, May 2010.
- [R1-16a] "R1-162199, waveform candidates," Qualcomm Incorporated, 3GPP TSG-RAN WG1 #84b, Discussion/Decision 36.331, 04 2016.
- [R1-16b] "R1-162199, WOLA and filtered-OFDM comparison beyond link level performance," Qualcomm Incorporated, 3GPP TSG-RAN WG1 #86, Discussion/Decision 36.331, 04 2016.
- [R1-16c] "R1-166999, detailed configuration of F-OFDM and W-OFDM for LLS evaluation," Qualcomm Incorporated, 3GPP TSG-RAN WG1 #86, Discussion/Decision 36.331, 04 2016.
- [Rab96] L. R. Rabiner, *Multirate Digital Signal Processing*, 1st ed. Upper Saddle River, NJ, USA: Prentice Hall PTR, 1996.
- [RH11] M. Renfors and F. Harris, "Highly adjustable multirate digital filters based on fast convolution," in *Proc. European Conference on Circuit Theory and Design (ECCTD)*, Aug. 2011, pp. 9–12.
- [RMKB17] M. Renfors, X. Mestre, E. Kofidis, and F. Bader, *Orthogonal Waveforms and Filter Banks for Future Communication Systems*. United States: Elsevier Inc., 1 2017.
- [RMZ<sup>+</sup>16] R. Ratasuk, N. Mangalvedhe, Y. Zhang, M. Robert, and J. P. Koskinen, "Overview of narrowband IoT in LTE Rel-13," in *Proc. 2016 IEEE Conference on Standards for Communications and Networking (CSCN)*, Oct. 2016, pp. 1–7.
- [RS<sup>+</sup>13] T. S. Rappaport, S. Sun *et al.*, "Millimeter wave mobile communications for 5G cellular: It will work!" *IEEE Access*, vol. 1, pp. 335–349, May 2013.

- [RS<sup>+</sup>14] W. Roh, J. Seol *et al.*, “Millimeter-wave beamforming as an enabling technology for 5G cellular communications: theoretical feasibility and prototype results,” vol. 52, no. 2, pp. 106–113, Feb. 2014.
- [RTM<sup>+</sup>17] R. Ratasuk, J. Tan, N. Mangalvedhe, M. H. Ng, and A. Ghosh, “Analysis of NB-IoT deployment in LTE guard-band,” in *Proc. Vehicular Technology Conference (VTC Spring)*, Jun. 2017, pp. 1–5.
- [RY13] M. Renfors and J. Yli-Kaakinen, “Timing offset compensation in fast-convolution filter bank based waveform processing,” in *Proc. International Symposium on Wireless Communication Systems (ISWCS)*, Aug 2013, pp. 1–5.
- [RY14a] M. Renfors and J. Yli-Kaakinen, “Channel equalization in fast-convolution filter bank based receivers for professional mobile radio,” in *Proc. European Wireless Conference (EW)*, May 2014, pp. 1–5.
- [RY14b] M. Renfors and J. Yli-Kaakinen, “Fast-convolution implementation of linear equalization based multiantenna detection schemes,” in *Proc. International Symposium on Wireless Communications Systems (ISWCS)*, Aug. 2014, pp. 712–716.
- [RYH14] M. Renfors, J. Yli-Kaakinen, and F. J. Harris, “Analysis and design of efficient and flexible fast-convolution based multirate filter banks,” *IEEE Transactions on Signal Processing*, vol. 62, no. 15, pp. 3768–3783, Aug. 2014.
- [RYL<sup>+</sup>15] M. Renfors, J. Yli-Kaakinen, T. Levanen, M. Valkama, T. Ihalainen, and J. Vihriala, “Efficient fast-convolution implementation of filtered CP-OFDM waveform processing for 5G,” in *Proc. Globecom Workshops (GC Wkshps)*, Dec. 2015, pp. 1–7.
- [RYLV16] M. Renfors, J. Yli-Kaakinen, T. Levanen, and M. Valkama, “Fast-convolution filtered OFDM waveforms with adjustable CP length,” in *Proc. Global Conference on Signal and Information Processing (GlobalSIP)*, Dec. 2016, pp. 635–639.
- [SA11a] A. Sahin and H. Arslan, “Edge windowing for OFDM based systems,” *IEEE Communications Letters*, vol. 15, no. 11, pp. 1208–1211, Nov. 2011.
- [SA11b] A. Sahin and H. Arslan, “The impact of scheduling on edge windowing,” in *Proc. Global Telecommunications Conference (GLOBECOM)*, Dec. 2011, pp. 1–5.
- [Sal67] B. Saltzberg, “Performance of an efficient parallel data transmission system,” *IEEE Transactions on Communication Technology*, vol. 15, no. 6, pp. 805–811, Dec. 1967.
- [SAYR15] K. Shao, J. Alhava, J. Yli-Kaakinen, and M. Renfors, “Fast-convolution implementation of filter bank multicarrier waveform processing,” in *Proc. International Symposium on Circuits and Systems (ISCAS)*, May 2015, pp. 978–981.
- [SB93] H. V. Sorensen and C. S. Burrus, “Efficient computation of the DFT with only a subset of input or output points,” vol. 41, no. 3, pp. 1184–1200, Mar. 1993.
- [SBJ88] H. V. Sorensen, C. S. Burrus, and D. L. Jones, “A new efficient algorithm for computing a few DFT points,” in *Proc. IEEE Int. Symp. Circuits Syst. (ISCAS)*, vol. 2, Jun. 1988, pp. 1915–1918.
- [SHB86] H. Sorensen, M. Heideman, and C. Burrus, “On computing the split-radix FFT,” *IEEE Transactions on Acoustics, Speech, and Signal Processing*, vol. 34, no. 1, pp. 152–156, Feb. 1986.



- [SIVR10] T. Stitz, T. Ihalainen, A. Viholainen, and M. Renfors, "Pilot-based synchronization and equalization in filter bank multicarrier communications," *EURASIP Journal on Advances in Signal Processing*, vol. 2010, no. 1, p. 741429, Feb. 2010.
- [SL05] R. Song and S.-H. Leung, "A novel OFDM receiver with second order polynomial Nyquist window function," *IEEE Communications Letters*, vol. 9, no. 5, pp. 391–393, May 2005.
- [SM15] D. Soldani and A. Manzalini, "Horizon 2020 and beyond: On the 5G operating system for a true digital society," *IEEE Vehicular Technology Magazine*, vol. 10, no. 1, pp. 32–42, Mar. 2015.
- [SMS<sup>+</sup>17] M. Shafi, A. F. Molisch, P. J. Smith, T. Haustein, P. Zhu, P. De Silva, F. Tufvesson, A. Benjebbour, and G. Wunder, "5G: A tutorial overview of standards, trials, challenges, deployment, and practice," *IEEE Journal on Selected Areas in Communications*, vol. 35, no. 6, pp. 1201–1221, Jun. 2017.
- [SP99] B. R. Sekhar and K. M. M. Prabhu, "Radix-2 decimation-in-frequency algorithm for the computation of the real-valued FFT," *IEEE Transactions on Signal Processing*, vol. 47, no. 4, pp. 1181–1184, Apr. 1999.
- [SPYR17] K. Shao, L. Pi, J. Yli-Kaakinen, and M. Renfors, "Filtered multitone multicarrier modulation with partially overlapping sub-channels," in *Proc. European Signal Processing Conference (EUSIPCO)*, Aug. 2017, pp. 405–409.
- [SR17] P. Siohan and M. Renfors, "Chapter 7 - orthogonal communication waveforms," in *Orthogonal Waveforms and Filter Banks for Future Communication Systems*, M. Renfors, X. Mestre, E. Kofidis, and F. Bader, Eds. Academic Press, 2017, pp. 129 – 156.
- [SSE<sup>+</sup>16] F. Schaich, B. Sayrac, S. Elayoubi, I.-P. Belikaidis, M. Caretti, A. Georgakopoulos, X. Gong, E. Kosmatos, H. Lin, P. Demestichas, B. Mouhouche, K. Pedersen, N. Pratas, M. Schellmann, M. Schubert, M. Shaat, and G. Wunder, "FANTASTIC-5G: flexible air interface for scalable service delivery within wireless communication networks of the 5th generation," *Transactions on Emerging Telecommunications Technologies*, vol. 27, no. 9, pp. 1216–1224, 2016.
- [SSL02] P. Siohan, C. Siclet, and N. Lacaille, "Analysis and design of OFDM/OQAM systems based on filterbank theory," *IEEE Transactions on Signal Processing*, vol. 50, no. 5, pp. 1170–1183, May 2002.
- [SW14] F. Schaich and T. Wild, "Waveform contenders for 5G — OFDM vs. FBMC vs. UFMFC," in *Proc. International Symposium on Communications, Control and Signal Processing (ISCCSP)*, May 2014, pp. 457–460.
- [SW17] F. Schaich and T. Wild, "Method of and apparatus for providing a sample vector representing at least a portion of a multi-carrier modulated signal," Patent application EP3 136 200A1, 2017.
- [SWA<sup>+</sup>16] F. Schaich, T. Wild, R. Ahmed *et al.*, "Deliverable D3.1: Preliminary results for multi-service support in link solution adaptation," Project: Flexible Air iNTErFAce for Scalable service delivery wiThin wireless Communication networks of the 5th Generation (FANTASTIC-5G), Tech. Rep., May 2016.

- [SWC14] F. Schaich, T. Wild, and Y. Chen, "Waveform contenders for 5G - suitability for short packet and low latency transmissions," in *Proc. Vehicular Technology Conference (VTC Spring)*, May 2014, pp. 1–5.
- [SYLR18] K. Shao, J. Yli-Kaakinen, T. Levanen, and M. Renfors, "Phase-noise analysis of overlapping filtered multitone waveforms in millimeter-wave radio systems," in *Proc. Asilomar Conference on Signals, Systems, and Computers (ACSSC)*, Oct. 2018, pp. 269–273.
- [TMS<sup>+</sup>18] K. Tani, Y. Medjahdi, H. Shaiek, R. Zayani, and D. Roviras, "PAPR reduction of post-OFDM waveforms contenders for 5G amp; Beyond using SLM and TR algorithms," in *Proc. International Conference on Telecommunications (ICT)*, Jun. 2018, pp. 104–109.
- [Tom05] S. Tomasin, "Overlap and save frequency domain DFE for throughput efficient single carrier transmission," in *Proc. International Symposium on Personal, Indoor and Mobile Radio Communications (PIMRC)*, vol. 2, Sep. 2005, pp. 1199–1203.
- [TUIT09] M. Tanabe, M. Umehira, K. Ishihara, and Y. Takatori, "A new flexible channel access scheme using overlap FFT filter-bank for dynamic spectrum access," in *Proc. Asia-Pacific Conference on Communications*, Oct. 2009, pp. 178–181.
- [UT10] M. Umehira and M. Tanabe, "Performance analysis of overlap FFT filter-bank for dynamic spectrum access applications," in *Proc. Asia-Pacific Conference on Communications (APCC)*, Oct. 2010, pp. 424–428.
- [Vai93] P. P. Vaidyanathan, *Multirate Systems and Filter Banks*. Upper Saddle River, NJ, USA: Prentice-Hall, Inc., 1993.
- [VL01] L. Vangelista and N. Laurenti, "Efficient implementations and alternative architectures for OFDM-OQAM systems," *IEEE Transactions on Communications*, vol. 49, no. 4, pp. 664–675, Apr. 2001.
- [VT95] R. Vallet and K. H. Taieb, "Fraction spaced multi-carrier modulation," *Wireless Personal Communications*, vol. 2, no. 1, pp. 97–103, Mar. 1995.
- [VWS<sup>+</sup>13] V. Vakilian, T. Wild, F. Schaich, S. ten Brink, and J. Frigon, "Universal-filtered multi-carrier technique for wireless systems beyond LTE," in *Proc. Globecom Workshops (GC Wkshps)*, Dec. 2013, pp. 223–228.
- [WAT16] S. Wang, J. Armstrong, and J. S. Thompson, "Waveform performance for asynchronous wireless 5G uplink communications," in *Proc. Annual International Symposium on Personal, Indoor, and Mobile Radio Communications (PIMRC)*, Sep. 2016, pp. 1–6.
- [Wel67] P. Welch, "The use of fast Fourier transform for the estimation of power spectra: A method based on time averaging over short, modified periodograms," *IEEE Transactions on Audio and Electroacoustics*, vol. 15, no. 2, pp. 70–73, Jun. 1967.
- [WHKJ04] T. Weiss, J. Hillenbrand, A. Krohn, and F. K. Jondral, "Mutual interference in OFDM-based spectrum pooling systems," in *Proc. Vehicular Technology Conference (VTC Spring)*, vol. 4, May 2004, pp. 1873–1877.

- [WJ04] T. A. Weiss and F. K. Jondral, "Spectrum pooling: an innovative strategy for the enhancement of spectrum efficiency," *IEEE Communications Magazine*, vol. 42, no. 3, pp. S8–14, Mar. 2004.
- [WJK<sup>+</sup>14] G. Wunder, P. Jung, M. Kasparick, T. Wild, F. Schaich, Y. Chen, S. T. Brink, I. Gaspar, N. Michailow, A. Festag, L. Mendes, N. Cassiau, D. Ktenas, M. Dryjanski, S. Pietrzyk, B. Eged, P. Vago, and F. Wiedmann, "5G NOW: non-orthogonal, asynchronous waveforms for future mobile applications," *IEEE Communications Magazine*, vol. 52, no. 2, pp. 97–105, Feb. 2014.
- [WLA<sup>+</sup>17] Y. . E. Wang, X. Lin, A. Adhikary, A. Grovlen, Y. Sui, Y. Blankenship, J. Bergman, and H. S. Razaghi, "A primer on 3GPP narrowband internet of things," *IEEE Communications Magazine*, vol. 55, no. 3, pp. 117–123, Mar. 2017.
- [WWS15] X. Wang, T. Wild, and F. Schaich, "Filter optimization for carrier-frequency- and timing-offset in universal filtered multi-carrier systems," in *Proc. Vehicular Technology Conference (VTC Spring)*, May 2015, pp. 1–6.
- [WWSF14] X. Wang, T. Wild, F. Schaich, and A. Fonseca dos Santos, "Universal filtered multi-carrier with leakage-based filter optimization," in *European Wireless 2014; 20th European Wireless Conference*, May 2014, pp. 1–5.
- [XYW<sup>+</sup>18] J. Xu, J. Yao, L. Wang, Z. Ming, K. Wu, and L. Chen, "Narrowband internet of things: Evolutions, technologies, and open issues," *IEEE Internet of Things Journal*, vol. 5, no. 3, pp. 1449–1462, Jun. 2018.
- [Yam04] H. Yamaguchi, "Active interference cancellation technique for MB-OFDM cognitive radio," in *Proc. European Microwave Conference*, vol. 2, Oct. 2004, pp. 1105–1108.
- [YFL14] Z. You, J. Fang, and I.-T. Lu, "Out-of-band emission suppression techniques based on a generalized OFDM framework," *EURASIP Journal on Advances in Signal Processing*, vol. 2014, no. 1, p. 74, May 2014.
- [YKLRP18] J. Yli-Kaakinen, T. Levanen, M. Renfors, and K. Pajukoski, "FFT-domain signal processing for spectrally-enhanced CP-OFDM waveforms in 5G new radio," in *Proc. Asilomar Conference on Signals, Systems, and Computers (ACSSC)*, 2018, pp. 1049–1056.
- [YKR16] J. Yli-Kaakinen and M. Renfors, "Optimization of flexible filter banks based on fast convolution," *Journal of Signal Processing Systems*, vol. 85, no. 1, pp. 101–111, Oct 2016.
- [YLRV17] J. Yli-Kaakinen, T. Levanen, M. Renfors, and M. Valkama, "Optimized fast convolution based filtered-OFDM processing for 5G," in *Proc. European Conference on Networks and Communications (EuCNC)*, Jun. 2017, pp. 1–6.
- [YLV<sup>+</sup>17] J. Yli-Kaakinen, T. Levanen, S. Valkonen, K. Pajukoski, J. Pirskanen, M. Renfors, and M. Valkama, "Efficient fast-convolution-based waveform processing for 5G physical layer," *IEEE Journal on Selected Areas in Communications*, vol. 35, no. 6, pp. 1309–1326, Jun. 2017.
- [YPW08] Z. Yuan, S. Pagadarai, and A. M. Wyglinski, "Cancellation carrier technique using genetic algorithm for OFDM sidelobe suppression," in *Proc. Military Communications Conference (MILCOM)*, Nov. 2008, pp. 1–5.

- [YR13] J. Yli-Kaakinen and M. Renfors, "Fast-convolution filter bank approach for non-contiguous spectrum use," in *Proc. Future Network Mobile Summit*, Jul. 2013, pp. 1–10.
- [YR14a] J. Yli-Kaakinen and M. Renfors, "Multi-mode filter bank solution for broadband pmr coexistence with TETRA," in *Proc. European Conference on Networks and Communications (EuCNC)*, Jun. 2014, pp. 1–5.
- [YR14b] J. Yli-Kaakinen and M. Renfors, "Optimization of flexible filter banks based on fast-convolution," in *Proc. International Conference on Acoustics, Speech and Signal Processing (ICASSP)*, May 2014, pp. 8317–8320.
- [YR15a] J. Yli-Kaakinen and M. Renfors, "Flexible fast-convolution implementation of single-carrier waveform processing for 5G," in *Proc. International Conference on Communication Workshop (ICCW)*, Jun. 2015, pp. 1269–1274.
- [YR15b] J. Yli-Kaakinen and M. Renfors, "Optimized burst truncation in fast-convolution filter bank based waveform generation," in *Proc. International Workshop on Signal Processing Advances in Wireless Communications (SPAWC)*, Jun. 2015, pp. 71–75.
- [YR18] J. Yli-Kaakinen and M. Renfors, "Optimized reconfigurable fast convolution-based transmultiplexers for flexible radio access," *IEEE Transactions on Circuits and Systems II: Express Briefs*, vol. 65, no. 1, pp. 130–134, Jan. 2018.
- [YX17] L. Yang and Y. Xu, "Filtered-OFDM system performance research based on Nuttall's Blackman-Harris window," in *Proc. International Conference on Communication Technology (ICCT)*, Oct. 2017, pp. 687–691.
- [ZCQA16] X. Zhang, L. Chen, J. Qiu, and J. Abdoli, "On the waveform for 5G," *IEEE Communications Magazine*, vol. 54, no. 11, pp. 74–80, Nov. 2016.
- [ZIX<sup>+</sup>18] L. Zhang, A. Ijaz, P. Xiao, M. M. Molu, and R. Tafazolli, "Filtered OFDM systems, algorithms, and performance analysis for 5G and beyond," *IEEE Transactions on Communications*, vol. 66, no. 3, pp. 1205–1218, Mar. 2018.
- [ZJC<sup>+</sup>15] X. Zhang, M. Jia, L. Chen, J. Ma, and J. Qiu, "Filtered-OFDM - enabler for flexible waveform in the 5th generation cellular networks," in *Proc. Global Communications Conference (GLOBECOM)*, Dec. 2015, pp. 1–6.
- [ZL10] R. Zakaria and D. Le Ruyet, "A novel FBMC scheme for spatial multiplexing with maximum likelihood detection," in *Proc. International Symposium on Wireless Communication Systems (ISWCS)*, Sep. 2010, pp. 461–465.
- [ZL12] R. Zakaria and D. Le Ruyet, "A novel filter-bank multicarrier scheme to mitigate the intrinsic interference: Application to MIMO systems," *IEEE Transactions on Wireless Communications*, vol. 11, no. 3, pp. 1112–1123, Mar. 2012.
- [ZLG<sup>+</sup>16] A. A. Zaidi, J. Luo, R. Gerzaguet, A. Wolfgang, R. J. Weiler, J. Vihriala, T. Svensson, Y. Qi, H. Halbauer, Z. Zhao, P. Zetterberg, and H. Miao, "A preliminary study on waveform candidates for 5G mobile radio communications above 6 GHz," in *Proc. Vehicular Technology Conference (VTC Spring)*, May 2016, pp. 1–6.

- [ZMMF17] D. Zhang, M. Matthé, L. L. Mendes, and G. Fettweis, "A study on the link level performance of advanced multicarrier waveforms under MIMO wireless communication channels," *IEEE Transactions on Wireless Communications*, vol. 16, no. 4, pp. 2350–2365, Apr. 2017.
- [ZMSR16] R. Zayani, Y. Medjahdi, H. Shaiek, and D. Roviras, "WOLA-OFDM: A potential candidate for asynchronous 5G," in *Proc. Globecom Workshops (GC Wkshps)*, Dec. 2016, pp. 1–5.
- [ZW00] C. Zhang and Z. Wang, "A fast frequency domain filter bank realization algorithm," in *Proc. World Computer Congress (WCC) - Int. Conf. Signal Process. (ICSP)*, vol. 1, Aug. 2000, pp. 130–132.
- [ZWG15] J. Zhao, W. Wang, and X. Gao, "Transceiver design for fast-convolution multicarrier systems in multipath fading channels," in *Proc. International Conference on Wireless Communications Signal Processing (WCSP)*, Oct. 2015, pp. 1–5.





